

Impact of pore-scale mass fluxes
on bioavailability and effective
degradation rates in bioremediation

Impact of pore-scale mass fluxes on bioavailability and effective degradation rates in bioremediation

Dissertation

zur Erlangung des akademischen Grades doctor rerum naturalium
(Dr. rer. nat.)

vorgelegt dem Rat der Chemisch-Geowissenschaftlichen Fakultät der
Friedrich-Schiller-Universität Jena

von Falk Heße, M. Sc. in Computational Science
geboren am 31. Mai 1977 in Gera

Promotionskommision:

Prof. Dr. Kai-Uwe Totsche Friedrich-Schiller-Universität Jena, Vorsitzender

Prof. Dr. Sabine Attinger Friedrich-Schiller-Universität Jena, Gutachter

Dr. Martin Thullner Universiteit Utrecht, Gutachter

Prof. Dr. Georg Büchel Friedrich-Schiller-Universität Jena

Prof. Dr. Reinhard Gaupp Friedrich-Schiller-Universität Jena

Tag der öffentlichen Verteidigung: 20. Januar 2010

Zusammenfassung.

Wasser ist zweifellos die wichtigste Ressource der Menschheit. Unter der Vielzahl von Funktionen, welche Wasser im Ökosystem der Erde erfüllt, ist die Trinkwasserversorgung, die für den Menschen unmittelbarste und essentielle. Der permanente Zugang zu sauberem Trinkwasser ist daher von grundlegender Bedeutung für jede Gesellschaft. Weltweit muss diese Aufgabe vor allem mit der wachsenden Bevölkerung sowie den Herausforderungen des Klimawandels umgehen. Obwohl Wasser auf unserem Planeten praktisch allgegenwärtig ist, kann nur ein Bruchteil davon für den Menschen genutzt werden. Nur drei Prozent der weltweiten Wasservorkommen können als Süßwasser bezeichnet werden und zwei Drittel dieser Vorkommen sind in Form von Eis in Gletschern gebunden. Doch auch der frei verfügbare Teil kann nicht ohne weiteres als Trinkwasser verwendet werden.

Der Grund für diese Einschränkung sind die hohen Anforderungen, die an die Wasserqualität gestellt werden um als Trinkwasser genutzt zu werden. Zu diesen Anforderungen zählen Farb- und Geruchlosigkeit, die Abwesenheit von Krankheitserregern sowie die Einhaltung von Maximalwerten für verschiedene gelöste Inhaltsstoffe. Die Einsicht in den engen Zusammenhang zwischen Wasserqualität und der Gesundheitsvorsorge führte zur Ausarbeitung internationaler Standards durch die Weltgesundheitsorganisation. Gemessen an diesen Standards existieren gegenwärtig große Defizite in der Wasserversorgung, vor allem in den sogenannten Entwicklungsländern.

In den industriellen oder entwickelten Ländern steht, aufgrund der starken Entwicklungsunterschiede zu den Entwicklungsländern, die Qualitätssicherung des Wassers vor anderen Herausforderungen. Die größte Bedrohung stammt hier von menschengemachten Verschmutzungen verursacht durch industrielle Alt-

lasten, Havarien, schlecht gewartete Abwassersysteme, landwirtschaftliche Chemikalien usw. Von den beiden potentiellen Trinkwasserquellen in Mitteleuropa stellt Grundwasser im Gegensatz zum Oberflächenwasser das wichtigere Reservoir dar. Gleichzeitig ist es jedoch durch die großen Schwierigkeiten Schadstoffquellen für Grundwasser zu lokalisieren, sie hinsichtlich ihrer Gefährlichkeit zu bewerten sowie geeignete Gegenmaßnahmen zu ergreifen, aus das deutlich schwieriger zu bewirtschaftende Reservoir. Diese Probleme leiten sich ab von der komplexen und heterogenen Struktur des Bodens, welche eine Vorhersage des Fliessverhaltens sowie der Abbauprozesses des Schadstoffes sehr aufwändig macht.

Aufgrund des hohen finanziellen Aufwandes, den eine direkte Reinigung eines verschmutzten Grundwasserleiters bedeutet, wurde in den letzten Jahren vermehrt In-Situ-Bioremeditation als alternative Sanierungsmethode verwendet. Bei diesem Verfahren kommen Mikroorganismen zur Anwendung, die in der Lage sind die im Grundwasser gelösten Schadstoffe abzubauen. In Folge des geringen technischen Aufwandes ist diese Methode in der Regel deutlich kostengünstiger. Dabei ist klar, dass nicht jeder Schadstoff von jedem Mikroorganismus gleich gut abgebaut werden kann, sowie die Bedingungen vor Ort den Abbauprozess stark beeinflussen können. Zur Optimierung des Abbaupotentials wurden daher eine Reihe vielfältiger Untersuchungen vorgenommen.

Ein wichtiges Problem der In-Situ-Bioremeditation ist dabei die Tatsache, dass in der Praxis erzielte Abbauraten meist deutlich niedriger ausfallen als unter idealisierten Laborbedingungen ermittelte Referenzwerte. Eine Ursache dieses Missverhältnisses liegt in der limitierten Bioverfügbarkeit der Schadstoffe unter natürlichen Bedingungen. Bioverfügbar meint hier den Anteil des im Grundwasser vorhandenen Schadstoffes der tatsächlich den Mikroorganismen zugänglich

ist. Ist dieser gering, ist dementsprechend auch die Effektivität des Abbauprozesses vermindert, was das Konzept der Bioverfügbarkeit zu einer wichtigen Größe bei der Bestimmung des Abbaupotentials macht. Aufgrund der komplexen Struktur des Bodens existieren eine große Zahl von Faktoren, die die Bioverfügbarkeit eines Schadstoffes vermindern können. Beispiele wären Massentransferprozesse auf verschiedenen Skalen, verschlossene Fließwege in der porösen Bodenmatrix usw.

Das Hauptziel dieser Arbeit ist die Beschreibung der Limitierung der Bioverfügbarkeit durch porenskalige Massenflüsse und deren Einfluss auf die effektiven Abbauraten.

Zu diesem Zweck wird in dieser Arbeit der Transport reaktiver Schadstoffe auf der Porenskala in einer zweidimensionalen Kanal- bzw. Sinusoidgeometrie mittels numerischer und analytischer Methoden untersucht. Der mikrobielle Abbau wurde in Form einer Randbedingung an den reaktiven Wänden der untersuchten Geometrie realisiert. Als Reaktionskinetik kommt in dieser Arbeit die Michaelis-Menten-Kinetik zur Anwendung. Zusätzlich wurde der Grenzfall einer Erstordnung-Kinetik betrachtet um analytische Lösungen zur Interpretation der Michaelis-Menten-Kinetik zu gewinnen, wo dies nicht möglich ist. Für die mathematische und numerische Analyse wurden die beschriebenen Gleichungen entdimensionalisiert, so dass die Ergebnisse leicht generalisierbar sind. Als relevante Kennzahlen traten dabei (i) der Thiele-Modul sowie (ii) das Verhältnis der Konzentration des Schadstoffes und der Michaelis-Konstanten hervor. Der Thiele-Modul vergleicht den diffusiven mit dem reaktiven Fluss auf Porenskala. Hohe Werte des Thiele-Modul kennzeichnen eine langsame Diffusion im Vergleich zur Reaktion und werden als diffusionslimitierendes Regime bezeichnet.

Für niedrige Werte spricht man hingegen von einem reaktionslimierten Regime. Die starke Abhängigkeit der Ergebnisse von dieser Kennzahl verdeutlicht den Einfluss der porenskaligen Diffusion auf die Bioverfügbarkeit, die sich umgekehrt proportional zum Thiele-Modul verhält. Die zweite Kennzahl ist ein Maß, ob die Michaelis-Menten-Kinetik durch die Grenzfälle einer Erstordnung-Kinetik oder eine Nulltordnung-Kinetik bzw. durch eine Mischung beider beschrieben werden kann. Die Transport- und Reaktionsprozesse wurden in den genannten Geometrien numerisch simuliert bzw. analytische oder semianalytische Lösungen entwickelt. Parallel zu diesem räumlich aufgelösten porenskaligen Modell wurde eine effektive eindimensionale Beschreibung des reaktiven Transports verwendet. Der Einfluss der porenskaligen Massenflüsse ist in diesem eindimensionalem Modell implizit in der effektiven Reaktionsrate enthalten. Deren Untersuchung erlaubt daher eine quantitative Beschreibung der Bioverfügbarkeit in Abhängigkeit von porenskaligen Transport- und Reaktionsprozessen. Die gemittelten Lösungen des zweidimensionalen Problems dienten dabei als Referenz zur Evaluierung der gefundenen effektiven Beschreibungen. Dies beinhaltet vor allem die Bestimmung von Parametern der effektiven Reaktionskinetik durch Fitten der Lösungen der effektiven Beschreibung an gemittelte Lösungen des räumlich expliziten Modells sowie die Bewertung der Genauigkeit der verwendeten effektiven Beschreibungen. Die Ergebnisse der Untersuchungen sind in den Kapiteln 3-5 der Arbeit dargelegt, in denen unterschiedliche Fragen aus dem oben beschriebenen Themenkreis untersucht und beantwortet werden.

In Kapitel 3 wird das Skalierungsverhalten in dem oben beschriebenen Setup für den Fall einer simplen Kanalgeometrie untersucht. Als porenskalige Reaktionskinetik wird neben der realistischen Michaelis-Menten-Kinetik ebenfalls der einfacherere Grenzfall einer Erstordnung-Kinetik verwendet. Für die Reakti-

onsrate der effektiven Beschreibung wurde dabei jeweils dieselbe Kinetik wie auf der Porenskala angenommen. Im Fall einer Erstordnung-Kinetik auf Porenskala kann die Relevanz der porenskaligen diffusiven Massenflüsse für die effektive Abbaurate anhand des Thiele-Modul dargelegt werden. Im diffusionslimitiertem Regime, d.h. einem großen Thiele-Modul, entstehen große Gradienten der Schadstoffkonzentration auf Porenebene. Dies hat zur Folge, dass die bioverfügbare Konzentration des Schadstoffes deutlich kleiner ist als die mittlere Porenkonzentration, d.h. die Bioverfügbarkeit ist sehr gering. Die effektive Reaktionsrate ist folglich ebenfalls sehr gering. Im entgegengesetzten reaktionslimitierten Regime ist die porenskalige Reaktion langsam im Vergleich zur Diffusion und der Thiele-Modul sehr klein. Die effektive Reaktionsrate ist dann stark mit der porenskaligen Reaktion korreliert. Das Übergangsregime mit etwa gleich schneller Reaktion und Diffusion ist von einer Mischung beider Extremfälle gekennzeichnet. Der Zusammenhang zwischen porenskaliger und effektiver Reaktionsrate kann sehr gut mittels eines einzelnen Skalierungsparameters beschrieben werden, welcher vom Thiele-Modul abhängt. Im Fall einer Michaelis-Menten-Kinetik auf Porenskala wird das Skalierungsverhalten deutlich komplexer. Dieses ist im Übergang zwischen reaktions- und diffusionslimitiertem Regime nun zusätzlich von dem Verhältnis von Schadstoffkonzentration zur Michaelis-Konstanten abhängig. Ein einzelner Skalierungsparameter, wie in der Literatur für eine Michaelis-Menten-Kinetik vorgeschlagen, kann in diesem Fall zu nicht unerheblichen Fehlern bei der Reproduktion der effektiven Kinetik führen. Diese Fehler sind jedoch deutlich reduziert, sobald nicht ein, sondern zwei unabhängige Skalierungsparameter verwendet werden, d.h. die beiden Reaktionsparameter der Michaelis-Menten-Kinetik müssen unabhängig voneinander skaliert werden. Die Anwendbarkeit der Skalierungsparameter ist in der

Praxis jedoch durch die Abhangigkeit von den zwei relevanten Kennzahlen der porenskaligen Reaktionskinetik eingeschrankt.

In Kapitel 4 wird das gleiche Porenskalenmodell mittels einer anderen effektiven Reaktionskinetik interpretiert. In diesem Kapitel wird eine effektive Beschreibung der Abbaukinetik mittels eines linearen Austauschterms abgeleitet, welcher die bioverfugbare sowie die gemittelte porenskalige Schadstoffkonzentration verknupft. In Analogie zu den Untersuchungen in Kapitel 3 wird dabei die bioverfugbare Konzentration entsprechend einer Michaelis-Menten-Kinetik abgebaut. Der Austausch zwischen beiden Konzentrationen ergibt sich durch deren Gradienten multipliziert mit einem Massenflusskoeffizienten. Im Fall eines Gleichgewichtes zwischen reaktiven und diffusiven Massenflussen, lassen sich Michaelis-Menten-Kinetik sowie linearer Austauschterm zu einem analytischen Ausdruck fur die effektive Abbaurate verbinden, der als Best-Gleichung oder Best-Kinetik bekannt ist. Im Gegensatz zu den Skalierungskoeffizienten in Kapitel 3 ist im Falle der Best-Kinetik der Massenflusskoeffizient des linearen Austauschterms die relevante Skalierungsgroe. In einem ersten Schritt wird dieser in Analogie zu Kapitel 3 durch Fitten bestimmt. Dabei zeigt sich ebenfalls eine starke Abhangigkeit des Massenflusskoeffizienten von den relevanten Kennzahlen, d.h. dem Thiele-Modul und dem Verhaltnis zwischen Konzentration und Michaelis-Konstante. Eine durchgefehrte Fehleranalyse zeigt, dass im Falle hoher bzw. niedriger Bioverfugbarkeit eine sehr gute Ubereinstimmung zwischen den exakten numerischen Ergebnissen und der effektiven Beschreibung besteht. In einem zweiten Schritt wurde anstelle des gefitteten Massenflusskoeffizienten ein konstanter Wert verwendet, der im Grenzfall einer porenskaligen Erstordnung-Kinetik analytisch bestimmt wurde. Eine Fehleranalyse der effektiven Beschreibung mittels des analytischen Massenflusskoeffizienten in Vergleich

zum Fall des gefitteten Koeffizienten zeigt ein qualitativ vergleichbares Bild mit nur leicht größeren Fehlern.

In Kapitel 5 wird ein im Vergleich zu Kapitel 3 und 4 modifiziertes Porenskalenmodell verwendet. Wurde in den beiden vorherigen Kapiteln die Reaktivität und damit die Verteilung der Mikroorganismen zeitlich und räumlich als konstant angesehen, wird in diesem Kapitel das Wachstum der Mikroorganismen explizit modelliert. Des Weiteren wird zusätzlich zur simplen Kanalgeometrie eine erweiterte Sinusoidgeometrie als Gebietsbeschreibung des Porenraumes verwendet. Die Ergebnisse zeigen, dass im Gleichgewicht von Wachstum und Absterben der Mikroorganismen es zu einer Entkopplung von Transport und Reaktion kommt. Diese Reduzierung der Komplexität trotz Erhöhung der Freiheitsgrade des Systems kann erklärt werden durch die Adaption der Verteilung der Mikroorganismen. Diese erreicht ihr Gleichgewicht wenn in jedem Zeitschritt das Wachstum durch die einkommenden diffusiven Flüsse des Schadstoffes gleich der Menge an sterbenden Mikroorganismen ist. Das Ergebnis ist eine konstante bioverfügbare Konzentration des Schadstoffes wodurch sich mathematisch ein reines Transportproblem ergibt. Da das Wachstum der Mikroorganismen nur durch die diffusiven Massenflüsse beschränkt ist, kann für die effektive Abbaukinetik stets von einem diffusionslimitiertem Regime ausgegangen werden. Die Beschreibung der effektiven Reaktionskinetik ist für den Fall einer Kanalgeometrie demnach identisch mit diesem bereits in Kapitel 3 beschriebenen Grenzfall. Für den Fall einer erweiterten Sinusoidgeometrie als Gebietsbeschreibung ergibt sich ein anderes Bild. Im Vergleich zu einer Kanalgeometrie gleichen Volumens zeigt sich eine vergrößerte Abbaurate in der effektiven Abbaukinetik, die proportional zur Amplitude der Variation der Porenbreite ist. Dieser Effekt kann mit dem überproportional starken Zuwachs des Abbaus in den schmalen Stel-

len des Porenraumes verglichen mit der gleichzeitigen Abnahme in den breiten Stellen erklärt werden.

Zusammenfassend kann gesagt werden, dass diese Arbeit einen relevanten Beitrag zur Skalierung der Reaktionskinetik von porenskaligen Bioabbau leisten möchte. Im Fall einer durch porenskalige Massenflüsse begrenzten Bioverfügbarkeit zeigt sich ein nichttriviales Skalierungsverhalten. Insbesondere der Einfluss der Konzentration wurde hervorgehoben und beschrieben. Weder die Annahme einer effektive Michaelis-Menten-Kinetik noch die Beschreibung mittels der Best-Kinetik können den Skalierungsschritt perfekt wiedergeben. Die vorgestellten Methoden erlauben jedoch eine hinreichend gute Beschreibung wobei die Best-Kinetik mit analytisch bestimmten Massenflusskoeffizienten gute Genauigkeit mit einfacher Anwendbarkeit verbindet. Für den praktischen Einsatz wurde in Kapitel 3 und 4 eine Übersicht abgeleitet unter welchen Umständen die Limitierungen durch porenskalige Massenflüsse berücksichtigt werden müssen. Als wichtigste Kennzahlen wurden dabei der Thiele-Modul sowie das Verhältnis von Schadstoffkonzentration und Michaelis-Konstante identifiziert. Weiterhin wurde in Kapitel 4 an einem Beispiel demonstriert, wie diese relevanten Kennzahlen für einen gegebenen Versuchsaufbau bestimmt und die effektiven Reaktionskinetiken angewendet werden können.

Abstract.

The supply of drinking water of sufficient quality is unarguably one of the most important tasks of every society. In the developed world the most serious threat for this supply are anthropogenic pollutants originating for example from landfill or sewage leaks or from agriculture. From the two main reservoirs of drinking water, i.e. surface water and groundwater, the latter is more important in Central Europe and likewise more vulnerable to such pollutants. The complex structure of the soil makes it difficult to estimate pathways of the pollutant and therefore hard to assess the risk and apply appropriate counter measures. Due to the high financial burden of classic remediation strategies cost effective methods like *in-situ* bioremediation has been developed and successfully applied in the last years. In these methods the ability of microbes is used to metabolize certain pollutants. Degradation rates in the field however, has been shown to be lower sometimes significantly than under idealized laboratory experiments. To explain this discrepancy the concept of bioavailability has been introduced. This concept draws a distinction between the measured or bulk concentration of the pollutant and the concentration available to the microbes. In case of a clear mismatch between both one speaks of a low bioavailability, which results in reduced degradation rates with respect to the bulk concentration. Due to the structure of the soil and the variety of the processes involved a low bioavailability can be caused by many different factors. In this study we focus on pore-scale mass fluxes. Since the microbes reside at the surface of the solid matrix a mismatch between bulk and bioavailable concentration can occur if reaction is fast compared to diffusive mass fluxes. Under such circumstances the scaling behavior of reaction kinetics becomes complex.

In this study we use simple two-dimensional channel and sinusoid geometries as representations of the pore space in order to simulate transport of a reactive species. Reaction kinetics will be simulated by appropriate boundary conditions of the geometry following a Michaelis-Menten or a first-order kinetics. The system will be solved numerically and the steady state solutions will be averaged transversal to the flow direction to get effective one-dimensional solutions. Effective descriptions of the one-dimensional system will be tested and assessed with respect to these numerical solutions.

In Chapter 3 we investigate the scaling behavior by assuming Michaelis-Menten kinetics for the effective one-dimensional description too. Research from the literature focussed on local first-order kinetics showed that the behavior of effective kinetics can be separated into three different regimes. For high bioavailability effective kinetics depends on pore-scale reaction. This regime is called reaction limited. In the case of low bioavailability the pore-scale diffusion is the limiting factor and the regime is therefore called diffusion limited. The transition regime between them is characterized by a mixture of both. If Michaelis-Menten kinetics is introduced for the pore-scale kinetics the scaling behavior becomes more complex. The transition zone between the two marginal regimes becomes additionally dependent on concentration. As a result we get large errors in the case of mediate bioavailability when trying to connect the parameters of the pore-scale and the effective Michaelis-Menten kinetics by a single constant scaling unit determined by fitting. These errors however, can be clearly reduced when introducing an additional degree of freedom, thus allowing the two reaction rate parameters of Michaelis-Menten kinetics to scale independently. The remaining error shows that strictly spoken Michaelis-Menten kinetics is not

prevailing in the effective regime, being however, small enough to justify the application.

In Chapter 4 the linear exchange model is applied to derive the reaction kinetics of the effective description of reactive transport. Within this concept the bulk and the bioavailable concentration are thought to represent two different reservoirs, with the latter being subject to biodegradation. The link between both reservoirs is modelled with a linear exchange term, i.e. being proportional to the gradient between both multiplied with the mass-flux coefficient. In steady state the linear exchange term and Michaelis-Menten kinetics can be combined to the so called Best kinetics being an alternative effective description for biodegradation. In order to estimate the unknown mass-flux coefficient optimum fits are performed in analogy to the procedure used in Chapter 3. The resulting estimate provide a good description in the cases of either low or high bioavailability. As an alternative a constant estimate for the mass-flux coefficient from the marginal case of a first-order kinetics is tested for the whole range of reaction regimes and found to describe the effective behavior with only little less accuracy.

In Chapter 5 a similar setup is used, compared to Chapters 3 and 4, with additionally considering biofilm growth and a sinusoid geometry. Results show that the adaption of the biofilm leads in steady state to a constant value for the bioavailable concentration. As a result the description of the reactive species turns into a simple transport problem with fixed concentration values at the boundaries of the medium. Since the growth of the biofilm is only limited by the incoming diffusional fluxes the steady state in the channel geometry will be identical to the results presented above for the case of a diffusion-limited regime. Results for the sinusoid geometry show a diffusion-limited regime in

the effective description as well but with higher reaction constants proportional to the amplitude of the pore-width variations.

In summary the thesis tries to achieve important contributions to the topic of bioavailability limited by pore-scale mass fluxes. Several effective descriptions for the pore-scale model developed herein were tested and discussed. A short guideline is presented when pore-scale mass fluxes must be considered. In addition, the reader is shown by means of a realistic example how the results from this work can be transferred to practice.

Nomenclature

Latin

A	...	amplitude of Ψ
\mathcal{A}	...	time dependent differential operator
a_v	...	specific reactive surface
c	...	concentration of the reactive species
c_0	...	concentration profile at Γ_f
c_{bio}	...	bioavailable concentration
c_{ref}	...	reference concentration
c_{mo}	...	concentration of the microorganisms
C	...	macroscale or bulk concentration
D	...	pore-scale diffusion coefficient
\mathbf{f}	...	flux of the concentration c
j_{tr}	...	mass-flux coefficient
K_m	...	Michaelis constant
k_{\max}	...	maximum reaction rate
k_{tr}	...	mass-transfer rate coefficient
\mathcal{L}	...	spatial differential operator
L_{ref}	...	reference length scale
\mathbf{n}	...	unit vector normal to Γ_s

Pe	...	Péclet number
q_{\max}	...	maximum conversion rate
Q	...	effective conversion rate
R	...	generic reaction rate
R_{tr}	...	mass exchange rate
\mathbf{v}	...	pore-scale fluid velocity
V	...	pore-scale average velocity
Y	...	microbial yield factor

Greek

η	...	scaling coefficient
Γ_f	...	boundary of Ω with the fluid
Γ_f^i	...	inlet of Ω_p
Γ_f^o	...	outlet of Ω_p
Γ_s	...	boundary of Ω with the solid
Φ^2	...	Thiele modulus
Ψ	...	transversal part of solution c
λ	...	eigenvalue of Ψ
μ_{dec}	...	decay rate of the microorganisms
τ_{ij}	...	coupling constant between mode i and j
Ω	...	whole domain
Ω_p	...	pore domain

miscellaneous

$\langle \cdot \rangle$...	averaged quantity
$\tilde{\cdot}$...	deviation quantity

$\hat{\cdot}$... scaled quantity
 \cdot_{eff} ... effective parameter
 \cdot_{eqv} ... constant approximation for \cdot_{eff}
 \cdot_i ... i th mode

Contents

Zusammenfassung/Abstract	v
Nomenclature	xvii
List of Figures	xxvii
List of Tables	xxxiii
1. Introduction	1
1.1. Relevance of the study	1
1.2. Objectives of the thesis	4
1.3. Outline	5
2. Basic theory and concepts	7
2.1. Historic perspective on the modelling of biodegradation	7
2.2. Pore-scale modelling	8
2.3. Mathematical description of reactive transport	9
2.3.1. Transport of reactive species	11
2.3.1.1. Advection	11
2.3.1.2. Dispersion	13
2.3.2. Reaction kinetics	13

2.4.	Bioavailability	16
2.5.	Upscaling	18
2.6.	Numerical solution of the system	22
2.6.1.	Discretization of the time derivative	22
2.6.2.	Grid generation	23
2.6.3.	Finite Element Method	24
2.7.	The software toolbox UG	30
3.	Upscaling of the advection-diffusion-reaction equation with Michealis-Menten kinetics	31
3.1.	Introduction	33
3.2.	Conceptual Model	37
3.2.1.	Mathematical description	37
3.2.2.	Geometrical description	41
3.2.3.	Scenarios considered for calculations	42
3.2.4.	Upscaling of the pore-scale processes	43
3.2.5.	Numerical scheme	45
3.3.	Upscaling and Analytical Methods	47
3.3.1.	First-order kinetics	47
3.3.1.1.	Uniform velocity field	48
3.3.1.2.	Parabolic velocity field	49
3.3.2.	Michaelis-Menten kinetics	51
3.3.2.1.	Uniform velocity field	51
3.3.2.2.	Parabolic velocity field	53
3.3.3.	Synopsis of analytical methods	55
3.4.	Results and Discussion	56
3.4.1.	First-order kinetics with uniform velocity field	56

3.4.2.	First-order kinetics with parabolic velocity field	59
3.4.3.	Michaelis-Menten kinetics with uniform velocity field	61
3.4.4.	Michaelis-Menten kinetics with parabolic velocity field . .	64
3.4.5.	Equivalent Michaelis-Menten parameters	66
3.4.6.	Synopsis	71
3.5.	Summary and Conclusion	73
4.	A Linear Exchange Model for the description of bioavailability at the pore scale.	77
4.1.	Introduction	79
4.2.	Theory	82
4.2.1.	Biodegradation at the pore scale	82
4.2.2.	Pore-scale geometry	83
4.2.3.	Mass transfer described by a linear exchange term	83
4.2.4.	Dimensionless description	86
4.2.5.	General approach	89
4.3.	Results and Discussion	91
4.3.1.	General behavior of the mass-flux coefficient j_{tr}	92
4.3.2.	Using a constant estimate for j_{tr}	95
4.3.3.	Comparison with macroscopic Michaelis-Menten kinetics .	97
4.3.4.	Relevance of pore-scale bioavailability restrictions	98
4.3.5.	Comparison to experimental data	100
4.3.6.	Implications for practical applications	101
5.	Influence of biofilm growth and pore-width variations on effective degradation rates	103
5.1.	Introduction	104

5.2. Theory	106
5.2.1. Scale of Interest	106
5.2.2. Governing Equations	106
5.2.3. Channel Domain	107
5.2.4. Sinusoid domain	108
5.2.5. Scaling analysis	109
5.2.6. Scenarios considered for the calculation	111
5.3. Analytical Methods	113
5.3.1. Scenario I	114
5.3.2. Scenario II	115
5.3.3. Scenario III	116
5.4. Results and Discussion	120
5.4.1. Scenario I	120
5.4.2. Scenario II	121
5.4.3. Scenario III	122
5.4.4. Scenario IV	124
5.4.5. Contributions of the new reactive-transport model	125
5.5. Summary and Conclusion	127
6. Synthesis	129
6.1. Summary and conclusions	129
6.2. Outlook	132
Bibliography	135
A. Appendix of Chapter 3	153
A.1. Development of the upscaled solution	153
A.1.1. Separation of the variables	153

A.1.2. Analysis of the case of first-order kinetics with a uniform velocity field	158
A.1.3. Analysis of the case of first-order kinetics with a parabolic velocity field	160
A.1.4. Analysis of the case of Michaelis-Menten kinetics	162
B. Appendix of Chapter 4	165
B.1. Analytical estimate for j_{tr}	165
B.2. Effective bioavailability	168
B.3. Experimental setup	169
Danksagung	173
Selbstständigkeitserklärung	175

List of Figures

1.1.	Schematic of a contaminant leaking into the subsurface and subsequently forming a plume due to being transported with groundwater flow.	3
2.1.	Schematic of the two geometries used in the study.	9
2.2.	Velocity distribution corresponding to the geometries used in this study (see Figure 2.1).	12
2.3.	Transport at the pore scale.	14
2.4.	Reaction rate $R(c_S)$ with respect to the concentration of the substrate c_S according to Michaelis-Menten, first-order and zeroth-order kinetics. The parameters in the example are; $k_{\max} = 1$ and $K_m = 0.1$	16
2.5.	Scheme of the different scales involved in reactive transport of a biodegradeable species.	17
2.6.	Upscaling in porous media.	20
2.7.	Representative example solution.	21
2.8.	Example for an unstructured grid with triangular elements for the two geometries used in the study (see Figure 2.1).	24
2.9.	Basis function φ_i of V_h in the FEM.	28

3.1. Schematic of the complexity of the subsurface and the variety the different scales involved.	34
3.2. Schematic of the computational domain.	37
3.3. Schematic sketch of the semi-infinite channel used to describe processes in a single pore.	42
3.6. Examples for first order reaction rate with uniform velocity field. The local parameters are $\Phi^2 = 10$ and $Pe = 2$. Top: sim- ulated two-dimensional results. Bottom: comparison of one- dimensional analytical and numerical solutions.	57
3.7. Dependency of Φ_{eff}^2 and η on Φ^2 in case of first-order kinetics with a uniform velocity field. Together with the linear and con- stant asymptotes representing the reaction-limited (reached for low values of Φ^2) and the diffusion limited regime (reached for high values of Φ^2). The value of Φ_{eff}^2 has been evaluated using Equation (A.23).	58
3.8. Examples of first-order kinetics with a parabolic velocity field. The local parameters are $\Phi^2 = 10$ and $Pe = 2$. Top: sim- ulated two-dimensional results. Bottom: comparison of one- dimensional analytical and numerical solution with results for a uniform velocity field.	60
3.9. Dependency on the effective parameters v_{eff} and D_{eff} from Φ^2 for the case of first-order kinetics with a uniform velocity field. The values were evaluated by solving the Equations (3.16a) and (3.16b)	61

3.10. Examples for Michaelis-Menten kinetics with uniform velocity field. The local parameters are $\Phi^2 = 10$, $Pe = 2$ and $K_m = 0.1$. Top: simulated two-dimensional solution. Bottom: comparison of analytical and numerical one-dimensional solutions with results from first-order kinetics.	62
3.11. Development of η for different Φ^2 and K_m for the case of Michaelis-Menten kinetics with uniform velocity field. The respective value of Φ^2 are tagged along the curves. The results were evaluated by using Equation (3.24).	63
3.12. Examples for Michaelis-Menten kinetics with a parabolic velocity field. The local parameters are $\Phi^2 = 10$, $K_m = 0.1$, and $Pe = 2$. Top: simulated two-dimensional solution. Bottom: comparison of analytical and numerical one-dimensional solutions.	65
3.13. Examples for Michaelis-Menten kinetics with a parabolic velocity field. The local parameters are $K_m = 0.1$ and $Pe = 2$	66
3.14. Dependency of the approximated equivalent scaling parameter η_{eqv} on Φ^2 in case of Michaelis-Menten kinetics with uniform velocity field.	67
3.15. Residual error made by using η_{eqv} (solid line) compared to two (dashed line) degrees of freedom (DoF) for Michaelis-Menten kinetics. Results were obtained assuming a value of $K_m = 0.1$	68
3.16. Dependency of the approximated equivalent parameters Φ_{eqv}^2 and $K_{m,\text{eqv}}$ on Φ^2 for several K_m in case of Michaelis-Menten kinetics with a parabolic velocity field.	70
3.17. General survey of the upscaling behavior in case of Michaelis-Menten kinetics. Borders of the zones with different regimes are drawn for demonstration purposes using arbitrary threshold values.	72

4.1. Top: Selected examples showing simulated concentration distributions for the full problem for two different scenarios. Bottom: Comparison of averaged numerical simulations (—) of the full problem to solutions of Equation (4.16) using Best kinetics with a fitted j_{tr} (\times) and using Michaelis-Menten kinetics with local reaction rate parameters (---).	91
4.2. Behavior and accuracy of the mass-flux coefficient j_{tr} from Equation (4.17) with respect to Φ^2 . The value of j_{tr} was determined by fitting an effective solution using Equation (4.16) to averaged numerical solutions of the full problem for several Φ^2 and c_0/K_m (a,b).	94
4.3. Residual errors made when using Best kinetics with a constant mass-flux coefficient $j_{\text{tr}} = \pi^2/4$ as effective reaction rate expression for several Φ^2 and c_0/K_m	96
4.4. Residual errors made by using different effective rate expression: Best kinetics with a constant $j_{\text{tr}} = \pi^2/4$ (dashed line), and with fitted values for j_{tr} (solid line), and Michaelis-Menten kinetics with one (dotted line) and two (dashed dotted line) degrees of freedom (DoF), i.e. independently fitted scaling parameter(s). Results were obtained assuming a value of $c_0/K_m = 10$	97
4.5. Effective bioavailability B_{eff} with respect to the local reaction rate parameters Φ^2 and C/K_m . The values were calculated as the ratio of the reactive flux given by Best kinetics using Equation (4.17) compared to the reactive flux given by Michaelis-Menten kinetics using Equation (4.18) with local parameters.	99
5.1. Schematic of the scale of interest.	106

5.2. Geometry of a channel geometry.	108
5.3. Geometry of a sinusoidal geometry.	109
5.4. Overview of the different scenarios considered in this study. . . .	112
5.5. Demonstration of the different scales in case of a sinusoidal geometry.	118
5.6. Distribution of the averaged concentration of the reactive species C and of the biomass c_{mo} along the channel as described in Figure 5.2 calculated for Scenario I. The coefficients for the numerical calculations were: $Pe = 1$, $Y = 0.1$ and $\mu_{\text{dec}} = 0.01$	120
5.7. Distribution of the averaged concentration of the reactive species C and of the biomass c_{mo} along the channel calculated for Scenario I and II. The coefficients for the numerical calculations were: $Pe = 1$, $Y = 0.1$ and $\mu_{\text{dec}} = 0.01$	122
5.8. Distribution of the averaged concentration of the reactive species C and of the biomass c_{mo} along the channel calculated for Scenario I and Scenario III. The coefficients for the numerical calculations were: $Pe = 1$, $Y = 0.1$ and $\mu_{\text{dec}} = 0.01$. The amplitude of the pore width variations for the simulation in Scenario III was $a = 0.5$	123
5.9. Averaged concentration C with respect to x for all four scenarios. The parameters for the simulations were: $Pe = 1$, $Y = 0.1$ and $\mu_{\text{dec}} = 0.01$	124
5.10. Averaged concentration C for different values of c_{bio} with respect to x for scenario I.	125
5.11. Development of Φ_{eqv}^2 in Scenario III for different amplitudes a . .	126

A.1. Solution of the eigenvalue problem described by Equation (A.5) displayed as the interfaces of the $\lambda \tan(\lambda)$ function (continuous line) and a constant reaction rate (dashed line, arbitrarily set to $\Phi^2 = 50$ in this example).	155
A.2. First five rows and columns of matrix \mathbf{T} in graphical and numerical display, evaluated for $\Phi^2 = 10$ in case of first-order kinetics and a parabolic velocity field.	160
A.3. Error made by using only a limited number of longitudinal modes for the calculation of $\langle C_1 \rangle$ in case of first-order kinetics and a parabolic velocity field.	162
B.2. Numerical estimate of the mass-flux coefficient j_{tr} with respect to Φ^2 in case of an effective first-order reaction rate (dashed line). The analytically derived value $j_{\text{tr}} = \pi^2/4$ is plotted as solid line.	168

List of Tables

3.1. Summary of cases and corresponding equations.	56
B.1. Measured parameters of the column experiment.	170

1. Introduction

This thesis would like to give a contribution to the field of biodegradation limited by pore-scale mass fluxes. In the Introduction the relevance of the topic will be motivated to the reader. Furthermore, the research questions will be given and the structure of the remainder of the text will be outlined.

1.1. Relevance of the study

Water is unarguably the most precious single resource on earth. Although it is also the most abundant substance on earth's surface only a small fraction can be used for drinking water supply. In order to be consumable water has to meet sufficiently high quality standards [World Health Organization, 1997]. In Europe the European Union (EU) has outlined the guidelines for its water policy in its *Water Framework Directive* [Kaika, 2003]. Unlike to most countries in the world drinking water supply in Germany is mostly based on groundwater. The quality of this important reservoir however, is endangered for example by wastewater, landfills, fertilizers from agriculture and/or industrial contaminants.

Although the pollution of groundwater, and therefore the drinking water supply, has been a permanent concomitant phenomenon of the industrialization from

the very beginning, the cleaning of the sites has not attracted much attention until some decades ago. This may be explained by the fact that groundwater contamination happens out of public sight compared to pollution of rivers and lakes. A contaminant entering the subsurface percolates slowly until reaching the groundwater table (see Figure 1.1). The groundwater flow then transports the contaminant, which evolves into a plume stretching sometimes long distances. A connection between the point of contaminant infiltration and extraction of the polluted water for drinking use may thus not be apparent. Public awareness of this issue first sparked the late 70's most notably with the prominent cases of Woburn [Bair and Metheny, 2005] and Love Canal [Gensburg et al., 2009], where severe health problems were connected to contaminated groundwater caused by dumped toxic waste. The decisions of the courts in these trials gave rise to the implementation of remediation techniques for the treatment of the polluted sites. Early efforts to restore such sites involved methods like pump-and-threat or the excavation of large volumes of soil, which are however, very expensive and have a high environmental impact. Therefore, researchers began to investigate alternative methods.

So called natural attenuation (NA) has attracted a lot of interest in the last decades. Passive or monitored NA simply relies on the ability of the soil to remediate itself whereas active or enhanced NA tries to increase this process by directly improve certain properties of the soil. Next to low costs NA can be very versatile and efficient if properly applied and has a low environmental impact. Mechanisms of NA include for example dilution, sorption, volatilization or abiotic transformations. The most effective mechanism however, is commonly biodremediation, i.e. the degradation of the contaminant by microorganisms.

Section 1.1: Relevance of the study

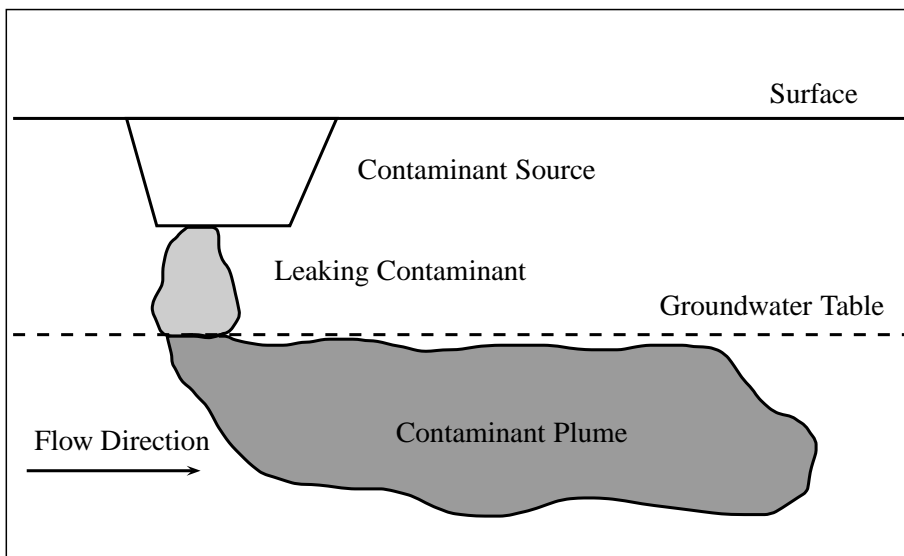


Figure 1.1.: Schematic of a contaminant leaking into the subsurface and subsequently forming a plume due to being transported with groundwater flow.

In order to perform a correct assessment of bioremediation for the treatment of a polluted site, it is necessary to consider the effectiveness of this strategy. To that end research has focused on determining the degradation rates of a certain pollutant by different microorganisms. A transfer of these results into practice however, has generally shown clearly lower degradation rates in the field. In order to describe this apparent discrepancy the term bioavailability is used. Many factors, which can affect the degradation rates in the field, are lumped into this term. Consequentially different concepts to bioavailability exists in practice. The focus of this study will be mass fluxes of the contaminant at the scale of single pores of the soil, which has been shown to be a relevant factor in limiting effective degradation rates.

1.2. Objectives of the thesis

With the problem in mind as outlined above the following objectives are to be addressed in this thesis:

- Does bioavailability limited by pore-scale mass fluxes change the effective reaction rate if the pore-scale reaction rate is assumed to follow Michaelis-Menten kinetics?
- Can the effect of pore-scale mass fluxes on effective reaction rates be described by using a linear exchange model?
- Which effective reaction rate is preferable in terms of accuracy and applicability?
- In which way does biofilm growth affect the effective reaction rate?
- Under which circumstances must the influence of pore-scale mass fluxes be considered and how can the effective descriptions developed herein be put into practice?

Answering these questions will hopefully contribute significantly to the field of biodegradation limited by bioavailability and by extension to the broader field of securing a sustainable water management.

1.3. Outline

The thesis itself consist of six chapters. Having passed the Introduction the reader will be familiarized in Chapter 2 with the theory and the methods used in this study. There will be some overlap with the respective sections in the Chapters 3-5. This is however, seen to be necessary in order to let them be self explanatory. The literature review and the outlining of the theory will be as concise as possible in order to minimize repetition. The next three Chapters are basically manuscripts written for publication in a peer reviewed journal and henceforth represent research studies on their own. Accordingly each Chapter is following the same structure comprising an introduction, a methodology, a results and discussion part as well as a short summary.

In Chapter 3 a pore-scale reactive transport model is investigated. The pore space is represented by a simple channel geometry in order to facilitate the use of analytical methods. Pore-scale biodegradation is modelled with Michaelis-Menten kinetics. Additionally the much simpler marginal case of first-order kinetics is used to validate the used model. In order to derive an effective description the model is averaged over the width of the pore represented by a channel geometry. The effective reaction rate is assumed to follow Michaelis-Menten kinetics too and the parameters are determined by fitting.

In Chapter 4 the same pore-scale reactive transport model is used as described above. Instead of Michaelis-Menten kinetics a Best kinetics is used for the description of the effective reaction rate. The free parameter is determined both by fitting and analytical means in the marginal case of first-order kinetics. The use of both parameters is assessed with respect to accuracy. The derived

effective description is furthermore used to interpret data from a laboratory experiment exhibiting a limited bioavailability.

In Chapter 5 an altered version of the previously used pore-scale reactive transport model is used. The microorganisms are assumed to grow according to the reactive influx until steady state is achieved. Furthermore, a more elaborated sinusoid geometry is used and the findings are compared to the case of a simple channel geometry.

Chapter 6 will contain a short summary of the findings presented in the former chapters with respect to the objectives given above. Furthermore, a short outline of future perspectives of the research presented herein will be given.

2. Basic theory and concepts

This chapter will give an overview on the basic concepts of modelling of biodegradation. In Section 2.1 a short introduction into the historic development of the topic will be given. After that we will present the geometric representation of the pore space as used in this study in Section 2.2 and derive the mathematical description of reactive transport in Section 2.3. Furthermore, the issues of bioavailability (Section 2.4) and upscaling (Section 2.5) will be introduced to the reader. In Section 2.6 the numerical implementation of the system derived in Section 2.3 will be explained and the software toolbox used for the numerical solution will be described in Section 2.7.

2.1. Historic perspective on the modelling of biodegradation

The study of groundwater as a scientific field has a relatively short history. It came not into existence until the pioneering work of Darcy [1856]. Further early contributions came for example from Boussinesq [1897], Thiem [1906] and Forchheimer [1914]. Understanding in the mechanisms of solute transport and reactive degradation however, has not been achieved until the second half of

the 20th century with the important contributions of [Bear, 1972], [Scheidegger, 1974], [Dagan, 1989] and [Gelhar, 1993].

With the advent of high-performance computers in the 1980s the study of reactive transport saw the development of the first efficient numerical models [Steefel and MacQuarrie, 1996], which were able to simulate the transport of a reactive species affected by degradation in the subsurface. Nowadays a broad variety of tools exists for the modeling of groundwater flow [Rausch et al., 2005], [Alvarez and Illman, 2005], [Nützmann et al., 2005] like MODFLOW [McDonald and Harbaugh, 2005], FEFLOW [Diersch, 1992] reactive transport like MUFTE/UG [Helmig et al., 1998] as well as biodegradation like MIN3P [Mayer, 2000], TBC [Schäfer et al., 1998] or GeoSys/BRNS [Kolditz, 2002]. The accuracy of these models however, is challenged by the identification and assessment of the relevant processes and the incorporation into such an integrative description of the fate of organic pollutants in the soil.

2.2. Pore-scale modelling

The typical scale of modeling in groundwater research or environmental engineering is much larger than the average diameter of the pore space. In this work however, we want to determine the influence of pore-scale processes of the bioavailability of a reactive species.

Consequently, we need to find a suitable representation of the pore space. Within this work we use two different geometries in order to describe the pore-scale processes spatially resolved. A simple channel domain (Figure 2.1a) as well as a sinusoid domain (Figure 2.1b). Within this geometries we need to

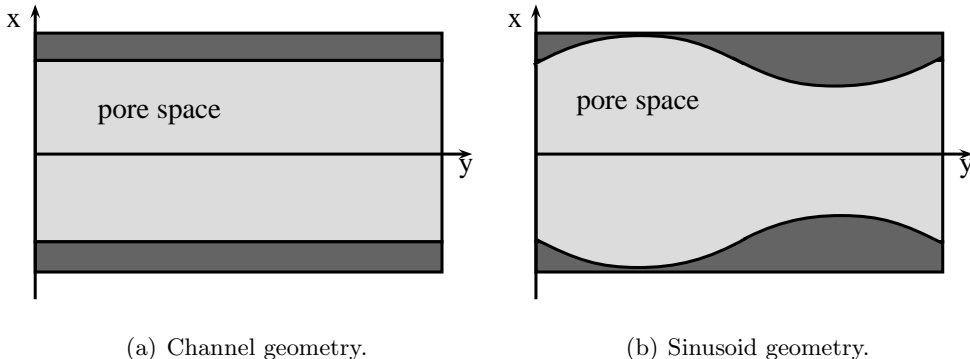


Figure 2.1.: Schematic of the two geometries used in the study.

investigate the processes of transport and biodegradation, which will be further explained in the following.

2.3. Mathematical description of reactive transport

For the mathematical description of the fate of a reactive species two different representations can be distinguished. The first one is called *particle based*. In this approach the processes of transport and biodegradation are modelled by describing a representative sample of individual particles. These particles can represent single molecules of the chemical compound or representative aggregates. The second representation describes the *concentration* of the species directly. In this model the quantity is therefore assumed to be a spatial continuum, which corresponds to a description based on *partial differential equations* (PDE's). In this study only the latter approach is used.

In order to derive the governing equations let us start with a simple balance equation for the concentration of the reactive species, denoted with c . In mathematical terms this quantity can be defined as an integrable function

$c : \Omega \times [0, T] \rightarrow \mathbb{R}$. Here $\Omega \subset \mathbb{R}^{\text{dim}}$ is an open subset of the physical space in either two or three spatial dimensions dim and $[0, T]$ denotes the time interval under consideration. In a given control volume $\Omega_V \subset \Omega$ the accumulation of mass is equal to the transport of mass across the boundary of the volume $\partial\Omega_V$ plus the creation and/or destruction of mass inside the volume per timestep. The mathematical representation of this balance is the following integral equation

$$\underbrace{\frac{d}{dt} \int_{\Omega_V} c \, d\Omega_V}_{\begin{array}{c} \text{accumulation} \\ \text{of mass} \end{array}} = \underbrace{\oint_{\partial\Omega_V} \mathbf{f}(c) \cdot \mathbf{n} \, dA}_{\begin{array}{c} \text{transport across} \\ \text{the boundary} \end{array}} + \underbrace{\int_{\Omega_V} R(c) \, d\Omega_V}_{\begin{array}{c} \text{source/sink} \\ \text{of mass} \end{array}}. \quad (2.1)$$

Here dA is an infinitesimal area of the surface of Ω_V and \mathbf{n} is the outer unit normal. The vector function $\mathbf{f}(c) : \Omega \times [0, T] \rightarrow \mathbb{R}^{\text{dim}}$ in Equation (2.1) lumps the relevant transport mechanisms affecting c together. The scalar product $\mathbf{n} \cdot \mathbf{f}(c)$ therefore yields the flux of c leaving Ω_V through dA in every time step. The source/sink term $R(c) : \Omega \times [0, T] \rightarrow \mathbb{R}$ can be interpreted in our scenario as the microbial degradation of the reactive species.

Referring to the Gauss's theorem the flux perpendicular to a closed surface can be equated to the divergence of this flux within the volume. Furthermore, integration and time derivative can be interchanged since the control volume Ω_V does not change with time. Equation (2.1) can therefore be rewritten into

$$\int_{\Omega_V} \frac{\partial}{\partial t} c \, d\Omega_V = \int_{\Omega_V} \nabla \cdot \mathbf{f}(c) \, d\Omega_V + \int_{\Omega_V} R(c) \, d\Omega_V. \quad (2.2)$$

For the derivation of Equation (2.2) no specific assumptions about the control volume Ω_V were made. As a result the equation must hold pointwise so the in-

Section 2.3: Mathematical description of reactive transport

tegral can be dropped. This leads eventually to the following partial differential equation:

$$\frac{\partial}{\partial t}c = \nabla \cdot \mathbf{f}(c) + R(c), \quad (2.3)$$

which is the well known continuity equation in its general differential form. In order to complete the mathematical description the flux $\mathbf{f}(c)$ and the sink term $R(c)$ need to be further specified, which will be addressed in the following. Additionally, the initial and boundary conditions have to be included. In order to keep the analysis generic this will be omitted at this point and defined in the Chapters 3, 4 and 5 individually.

2.3.1. Transport of reactive species

In the text above the flux $\mathbf{f}(c)$ of the concentration of the reactive species c has been kept unspecified. In the subsurface its movement can be driven by two different mechanisms; *advection* as well as *hydrodynamic dispersion*. Assuming a linear relationship we can write

$$\mathbf{f}(c) = \mathbf{f}_{\text{adv}}(c) + \mathbf{f}_{\text{dis}}(c) \quad (2.4)$$

for both fluxes respectively.

2.3.1.1. Advection

The transport mechanism advection can be described by the following relationship:

$$\mathbf{f}_{\text{adv}}(c) = \mathbf{v}c. \quad (2.5)$$

The vector field $\mathbf{v} : \Omega \times [0, T] \rightarrow \mathbb{R}^{\text{dim}}$ in Equation (2.5) can be interpreted in physical terms as the velocity field of the groundwater transporting the reactive species. Since water is an incompressible newtonian fluid its motion is described by the Navier-Stokes Equation [Navier, 1823]. At the pore scale this mathematical description can be simplified to the Stokes Equation [Stokes, 1842] due to the low Reynolds-numbers typically found in groundwater flow:

$$\mu \Delta \mathbf{v} = \nabla \cdot p. \quad (2.6)$$

In Equation (2.6) μ is the viscosity of the fluid and p denotes the pressure field.

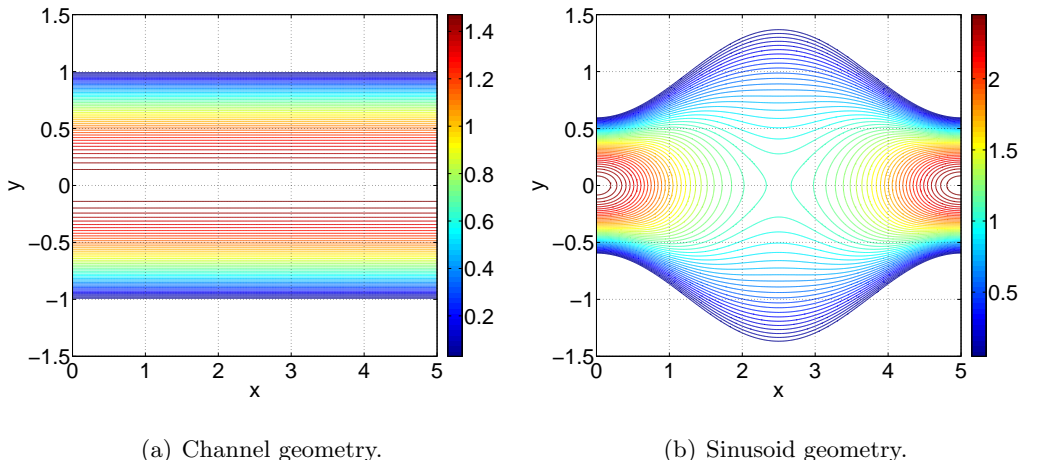


Figure 2.2.: Velocity distribution corresponding to the geometries used in this study (see Figure 2.1).

In this study two different representations of the pore space are used as depicted in Figure 2.1. For both geometries exist analytical solutions of Equation (2.6)

Section 2.3: Mathematical description of reactive transport

(see Figure 2.2 for an example), which will be further specified in Chapters 3, 4 and 5 individually.

Note that at the continuum scale fluid flow is described by the Darcy Equation [Darcy, 1856], due to the porous structure of the soil

$$\mathbf{v} = -K \nabla \cdot p \quad (2.7)$$

The coefficient function K in Equation (2.7) denotes the conductivity field of the soil comprising the effects of pore-scale fluid mechanics.

2.3.1.2. Dispersion

The second transport mechanism, which must be considered for groundwater flow, is hydrodynamic dispersion and is given by

$$\mathbf{f}_{\text{dis}}(c) = D \nabla c. \quad (2.8)$$

The coefficient function $D : \Omega \times [0, T] \rightarrow \mathbb{R}^{\text{dim} \times \text{dim}}$ is in general a tensor field lumping together the physical mechanisms of *molecular diffusion* [Fick, 1855] and *mechanical dispersion* caused by statistically distributed small scale flow paths [Taylor, 1953], [Aris, 1956], [Saffman, 1959] (see Figure 2.3). On the pore scale however, only molecular diffusion is contributing. In this work the coefficient function D is consequently a constant scalar.

2.3.2. Reaction kinetics

During the derivation of the mathematical description of reactive transport the source/sink term of Equation (2.3) was already identified with the biodegra-

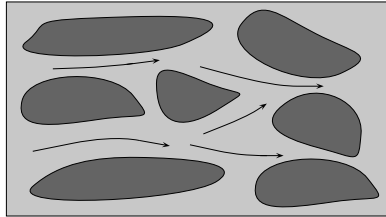


Figure 2.3.: Transport at the pore scale.

dation of the reactive species. The algebraic implementation of this coefficient function requires some knowledge of the mechanisms of microbial reaction kinetics. Unlike to plain chemical reactions, microorganisms are catalyzing a chemical substrate S with the help of enzymes E . In such a scenario the complex ES is first formed and subsequently transformed into the product P , whereas the enzyme leaves the process unchanged. The reaction process can therefore be described as



Here the parameters k_1 , k_{-1} and k_2 denote the respective kinetic rate constants. The rate equations for the concentrations of the product c_P and the complex c_{ES} are consequently

$$\frac{d}{dt}c_P = k_2 c_{ES}, \quad (2.10)$$

$$\frac{d}{dt}c_{ES} = k_1 c_E c_S - c_{ES}(k_{-1} + k_2). \quad (2.11)$$

Let us introduce the following two assumptions: First, we assume the total mass of enzymes to be constant so $E_{tot} = E + ES$. Second, we assume the complex

Section 2.3: Mathematical description of reactive transport

being formed very fast compared to the reactants, so it can be approximated being constant $\frac{d}{dt}c_{ES} = 0$. With this conditions it can be concluded that

$$c_{ES} = \frac{k_1 c_{E_{tot}} c_S}{k_{-1} - k_2 + k_1 c_S}. \quad (2.12)$$

Let us now introduce the following conventions: First, we define $k_{\max} = k_2 c_{E_{tot}}$. This value is the maximum reaction rate. Second, we set $K_m = (k_{-1} - k_2)/k_1$. This parameter is called the Michaelis constant. It is the value of the concentration, where half of the maximum conversion rate is achieved. Inserting Equation (2.12) into Equation (2.10) and using these definitions it can be stated that

$$R(c_S) = \frac{k_{\max}}{K_m + c_S} c_S. \quad (2.13)$$

Equation (2.13) is the classical reaction kinetics assumed for microbially catalyzed biodegradation. It is called Michaelis-Menten kinetics [Michaelis and Menten, 1913] and gives the relationship between the concentration of the reactive solute and the reaction rate.

Two marginal cases, for either very low or very high concentrations compared to K_m are important (see Figure 2.4). In the first case the reaction rate is reduced to first-order kinetics so

$$R(c_S) = \frac{k_{\max}}{K_m} c_S \quad (2.14)$$

holds. In the second case we get zeroth-order kinetics, i.e.

$$R(c_S) = k_{\max}. \quad (2.15)$$

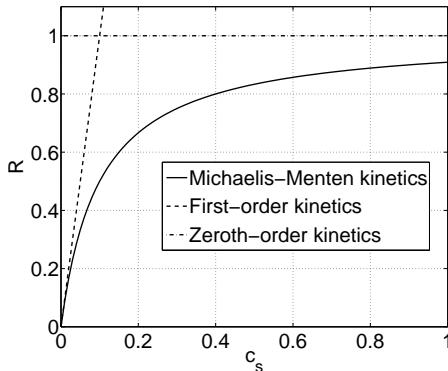


Figure 2.4.: Reaction rate $R(c_S)$ with respect to the concentration of the substrate c_S according to Michaelis-Menten, first-order and zeroth-order kinetics. The parameters in the example are; $k_{\max} = 1$ and $K_m = 0.1$.

It is clear, that, unlike Equation (2.14), the reaction kinetics in Equation (2.15) can only be valid for high concentrations. A constant conversion rate would sooner or later result in negative concentrations which is however, self contradictory.

2.4. Bioavailability

In the context of bioremediation it is crucial to asses the effectiveness of this strategy, i.e. to estimate the degradation rates of the pollutant in a given site. It is obvious that these rates are dependent on the ability of the microorganisms to metabolize the reactive species. A considerably amount of research has therefore been focused to determine microbial activity in idealized laboratory experiments. Measured degradation rates in the field however, are commonly lower, than one would expect from those laboratory results [Alexander, 2000].

Section 2.4: Bioavailability

In order to describe this discrepancy the term bioavailability has been introduced.

This term is used across many disciplines and therefore a broad variety of definitions exists [Semple et al., 2004]. It originated in pharmacology and is used to describe the effectiveness of a route of administration of a drug compared to intravenous injection, which is considered as the optimum. This concept has been transferred into the field of groundwater remediation to compare effective degradation rates in the field or from realistic experiments to results from idealized laboratory experiments regarded likewise as a reference [National Research Council (U.S.), 2003], [Haws et al., 2006]. For the reasons explained above, this quantity is an important tool for the assessment of bioremediation being deployed on a contaminated site.

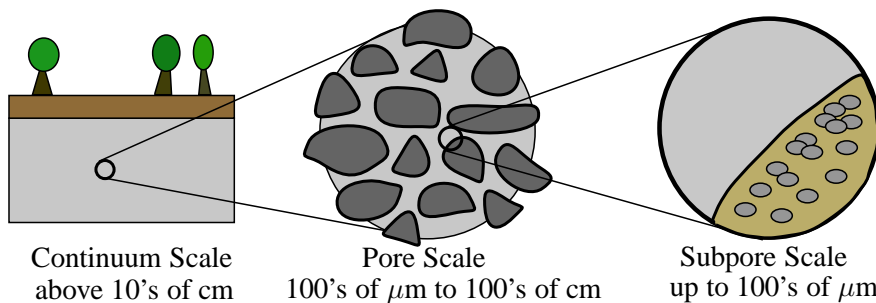


Figure 2.5.: Scheme of the different scales involved in reactive transport of a biodegradeable species.

Due to the complexity and heterogeneity of the subsurface several factors exist, which may decrease the bioavailability of a reactive species. Such factors include sorption, heterogeneity of the conductivity or limiting mass fluxes on different scales [Harms and Bosma, 1997] (see Figure 2.5). As stated above the focus of this study is on bioavailability limited by pore-scale mass fluxes.

Therefore, bioavailability will be defined as the ratio of the intrapore mass fluxes and the microbial reactive flux [Bosma et al., 1997]. In porous media a mismatch between these fluxes can occur due to the microbes being localized at the surface of the solid matrix (Figure 2.5 right part). If the microbial uptake is much faster than the diffusional mass flux strong gradients occur and the bioavailable concentration is much smaller than the bulk concentration in the aqueous phase. At the continuum scale however, these pore-scale variations are no longer resolved and the measured concentration can become a bad measure for assessing microbial degradation rates under such circumstances. In order to circumvent these difficulties the continuum-scale description of reactive transport has to incorporate such limitations by use of effective reaction rates. The mathematical procedure of the derivation of effective descriptions is called upscaling.

2.5. Upscaling

Upscaling refers to an ensemble of methods, which try to establish a mathematical relationship between a well known process at a smaller scale and a desired or given solution at a larger scale. Next to simple heuristic methods a large body of mathematical rigorous upscaling techniques exist. For the study of subsurface flow and reactive transport common approaches are Homogenization Theory [Papanicolaou, 1995], [Pavliotis, 2002], Volume Averaging [Whitaker, 1999] or Stochastic Method [Gelhar, 1993]. In the following the idea of upscaling will be outlined in short and the abstract framework will be connected to the issue of reactive transport.

To begin with consider the general system

$$\mathcal{A}c = f. \quad (2.16)$$

The operator \mathcal{A} is identified herein with the differential operator of Equation (2.3), so

$$\mathcal{A}c = \left(\frac{\partial}{\partial t} - \nabla \mathbf{v} + \nabla D \nabla - \frac{k_{\max}}{K_m + c} \right) c, \quad (2.17)$$

with the transport parameters \mathbf{v} and D as well as the reaction rate parameters k_{\max} and K_m . The unknown c is the solution of the system at the pore scale and the right hand side f comprises possible external influences. The need for upscaling arises if the solution c is given on a larger scale, which can be denoted with $\langle c \rangle$. This macroscale can be identified in our work with the continuum scale, where the pore-scale variations of c are no longer resolved. For the macroscale solution $\langle c \rangle$ the following definition may be sufficiently generic

$$\langle c \rangle = \frac{1}{\text{Vol}(\Omega_V)} \int_{\Omega_V} w(\Omega_V) c d\Omega. \quad (2.18)$$

Within the scope of this study this averaging process can be interpreted as an integral transformation. The function c is averaged over the representative volume Ω_V according to the weighting function $w(\Omega_V)$ (see Figure 2.6 for the interpretation of Ω_V in porous media). The factor $1/\text{Vol}(\Omega_V)$ is necessary to preserve the mass of c . This mathematical averaging corresponds in physical terms to the finite resolution of the measuring process were $w(\Omega_V)$ can be interpreted as the characteristic sensitivity of the sensor respectively the measuring process in general.

The process of upscaling can be consequentially described mathematically by

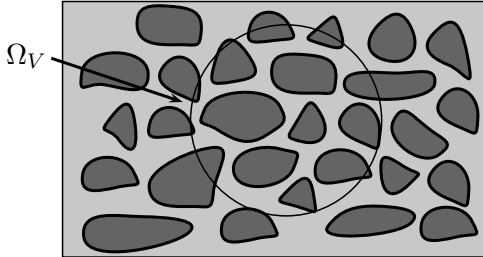


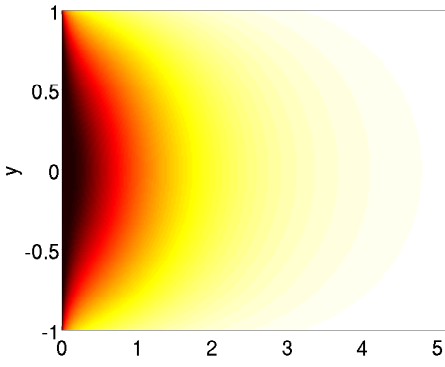
Figure 2.6.: Upscaling in porous media.

$$\langle \mathcal{A}c \rangle = \langle f \rangle \quad (2.19)$$

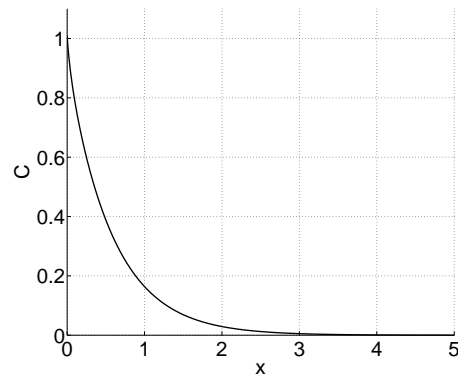
$$\mathcal{A}_{\text{eff}} \langle c \rangle = \langle f \rangle. \quad (2.20)$$

Equations (2.19) (2.20) illustrate that upscaling is the determination of the effective operator \mathcal{A}_{eff} . Compared to \mathcal{A} this operator can either change its form completely or simply exhibit new parameter values. An example for the former is the upscaling of groundwater flow. At the pore scale the motion of water is described by the Stokes Equation compared to the Darcy Equation at the continuum scale. The upscaling of reactive transport is rather an example for the latter. At the pore scale as well as at the continuum scale the flux is described by Equation (2.22) with adjusted coefficient functions \mathbf{v} and D . The scaling of the reaction kinetics however, is still an open question and some researchers have proposed different kinetics on the continuum scale to account for the influence of pore-scale mass fluxes [Bosma et al., 1997]. The question about the characteristics of the upscaled reaction kinetics is covered in detail in the Chapters 3 and 4.

With respect to the pore-scale representations used in this study (see Figure 2.1) the upscaling procedure is



(a) Spatially resolved two-dimensional solution corresponding to geometry depicted in Figure 2.1a.



(b) Averaged one-dimensional solution according to Equation (2.21).

Figure 2.7.: Representative example solution.

$$\langle c \rangle = C(x) = \frac{1}{h(x)} \int_0^{h(x)} c(x, y) \, dy, \quad (2.21)$$

with $C(x)$ denotes the averaged concentration in this work and $h(x)$ being the envelope of the respective geometries. This procedure applied to the spatially resolved two-dimensional description (example solution of which is seen in Figure 2.7a) will consequently yield an effective one-dimensional description of the process of reactive transport (example solution of which is seen in Figure 2.7b corresponding to Figure 2.7a) comprising the limiting effects of pore-scale mass fluxes on the reaction kinetics.

2.6. Numerical solution of the system

For the mathematical description of the process of biodegradation Equation (2.3) was shown to be valid. An analytical solution for this problem however, will only exist for a very confined set of scenarios. Commonly, numerical methods must be applied in order to find an acceptable approximation c_h , with h being a placeholder for the characteristic properties of the numerical scheme. To that end a proper *discretization*, i.e. a mapping of the system given by Equation (2.3) to a system of algebraic equations, has to be found

$$\mathcal{A}c = f \mapsto A_h c_h = f_h. \quad (2.22)$$

The main task, i.e. the derivation of A_h , will be divided in several steps. First, the time derivative will be discretized leaving a *Boundary Value Problem* (BVP)

$$\mathcal{L}c = f, \quad (2.23)$$

with the operator \mathcal{L} in Equation (2.23) being the spatial operator of \mathcal{A} , so

$$\mathcal{L}c = \left(\nabla \mathbf{v} - \nabla D \nabla + \frac{k_{\max}}{K_m + c} \right) c. \quad (2.24)$$

After that, the important steps for the solution of a BVP will be shortly introduced. This comprises grid generation, discretization and linearization.

2.6.1. Discretization of the time derivative

For the discretization of the time derivative a simple implicit Euler method is used in this work

$$\frac{\partial}{\partial t} c \approx \frac{c_{t+\Delta t} - c_t}{\Delta t}, \quad (2.25)$$

which has been shown to be robust and stable [Chikurov, 2006]. Inserting Equation (2.25) into the right part of Equation (2.22) yields

$$c_{t+\Delta t} \approx c_t + \Delta t (\mathcal{L}[c_{t+\Delta t}] + f). \quad (2.26)$$

Due to the implicit scheme Equation (2.26) leads a system of algebraic equations.

2.6.2. Grid generation

The first step of the numerical solution of a BVP is the geometric discretization of the domain Ω . This process is called grid or mesh generation. To that end Ω is decomposed into N elements Ω_i . For these element the following properties hold:

- All elements are pairwise disjunct: $\Omega_i \cap \Omega_j = \emptyset : (i \neq j)$.
- The decomposition is complete: $\bigcup_i \Omega_i = \Omega$.
- The elements Ω_i have a non-empty interior.

It is clear that different discretization methods demand different grids. Therefore, a broad variety from simple regular to versatile unstructured grids exists (for further information see for example [George and Frey, 2000], [Mackerle, 2001], [Ushakova, 2007]). In this work the Delaunay triangulation [George and Borouchaki, 1998] is used, which basic element is a triangle in two dimensions respectively a tetrahedra in three dimensions (see Figure 2.8). The grid size is

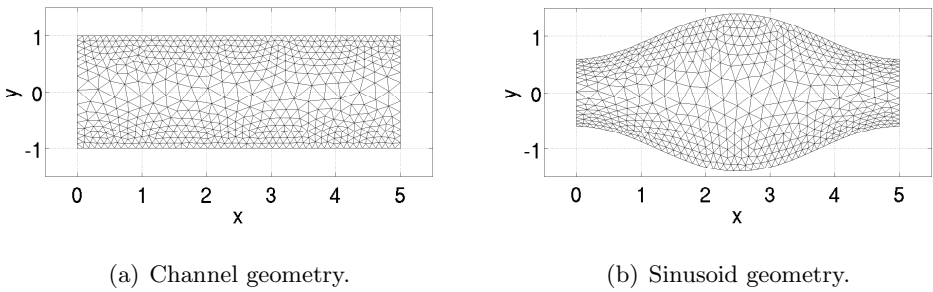


Figure 2.8.: Example for an unstructured grid with triangular elements for the two geometries used in the study (see Figure 2.1).

locally adapted close to the wall of the geometry, where strong gradients of the solution are expected (see example in Figure 2.7a).

2.6.3. Finite Element Method

The *Finite Element Method* (FEM) is a technique for obtaining a numerical solution of a BVP. The procedure of this method can be summarized by the following steps:

1. The BVP is rephrased in its *weak formulation* (WF).
2. In the actual *discretization* the solution space of the weak formulation is projected into a finite dimensional subspace.
3. In case the resulting algebraic system is nonlinear a suitable *linearization* scheme has to be applied.

The procedure for the derivation of the FEM outlined here is called *Galerkin method* [Galerkin, 1915]. As an alternative to step 1 and 2 the BVP can also be rephrased into a minimization problem, which is subsequently discretized. This

method is called *Ritz method* [Ritz, 1909] and has shown to be equivalent to the Galerkin method [Munz and Westermann, 2006]. For a more comprehensive treatment of the subject the reader is referred for example to Strang and Fix [1973], Knabner and Angermann [2003] or Hundsdorfer and Verwer [2003].

Weak formulation Starting point of the discretization in the FEM is not the partial differential equation but its weak formulation. The name emphasizes the fact that the solution of the WF complies to weaker conditions, especially with respect to the smoothness, compared to the classical or strong solution of the PDE. For the problem given by Equation (2.26) the WF can be formulated by multiplying Equation (2.23) with an arbitrarily chosen test function $v \in V$ and integrating over the domain Ω

$$\int_{\Omega} [\mathcal{L}c]v \, d\omega = \int_{\Omega} fv \, d\omega. \quad (2.27)$$

These test functions have to conform to the boundary conditions of the BVP. By applying Gauss' theorem to the second derivative of \mathcal{L} the order of the problem can be reduced by one. The calculation is not performed here but the curious reader is referred for example to van Kan et al. [2005] for more details. Let us now introduce the following conventions; $\int_{\Omega} [\mathcal{L}c]v \, d\omega := l(c, v)$ and $\int_{\Omega} fv \, d\omega := f(v)$, so

$$l(c, v) = f(v) \quad \forall v \in V. \quad (2.28)$$

Equation (2.28) is now called the weak formulation of the BVP. The main reason for this re-formulation can be motivated by the fact that the WF is a proper generalization of the concept of PDE's. That means every weak solution will

be identical with the classical solution provided the latter exists. Furthermore, owing to the reduction of the order of the problem by one, the WF will give us meaningful solutions even in cases where the PDE would fail. Conditions with less smoothness appear in many real world phenomena so the WF is better suited for the modelling of many physical processes.

Discretization (Galerkin method) In order to discretize Equation (2.28) the solution space V is replaced by an appropriate finite dimensional subspace $V_h \subset V$. Let the basis of this subspace be the set of basisfunctions $\varphi_1, \varphi_2, \dots, \varphi_N$, with N being the number of dimensions of V_h . Then, every element $v_h \in V_h$ and therefore the approximation of the solution c_h can be written as a linear combination of this basisfunctions

$$c_h = \sum_{i=1}^N c_i \varphi_i, \quad (2.29)$$

with the coefficients c_i still to determine. Replacing the solution c and the test functions v in Equation (2.28) by their finite dimensional counterparts c_h and v_h will yield the Galerkin Equation

$$l(c_h, v_h) = f(v_h) \quad \forall v_h \in V_h. \quad (2.30)$$

Note that the problem itself has not changed from Equation (2.28) to Equation (2.30) but the solution space. As a consequence c_h can in general only be an approximation of the true solution c . In the Galerkin method the following constraint is applied for the derivation of an algebraic system:

$$l(c_h, \varphi_i) = f(\varphi_i) \quad \forall \varphi_i. \quad (2.31)$$

Section 2.6: Numerical solution of the system

With this condition the *residual* is minimized, i.e. the difference between the right hand side of the Equations (2.30) and (2.28). Note that a residual of zero would require $c \in V_h$, which is usually not the case. Inserting Equation (2.29) into Equation (2.31) it can eventually be stated

$$L_h c_h = f_h, \quad (2.32)$$

with

$$L_h(j, i) = l(\varphi_j, \varphi_i) = \int_{\Omega} \mathcal{L}[\varphi_j] \varphi_i \, d\omega, \quad (2.33)$$

$$c_h(j) = c_j, \quad (2.34)$$

$$f_h(i) = f(\varphi_i). \quad (2.35)$$

Equation (2.32) is now the discretized form of the BVP given by Equation (2.23) representing a system of algebraic equations suitable for a numerical solution of the system. In order to complete the description the properties of the discretized solution space V_h used in the FEM need to be further specified.

Without expanding the analysis too far, it can be stated that V_h should meet two main requirements:

- The elements of V_h should be a representative sample of V , i.e. for any possible solution c a near approximation c_h can be found in V_h .
- The resulting matrix L_h should be sparse so efficient solvers can be applied.

The FEM satisfies both requirements by defining the basisfunctions φ_i of V_h as simple polynomials over the nodes N_i of the finite elements Ω_j (henceforth

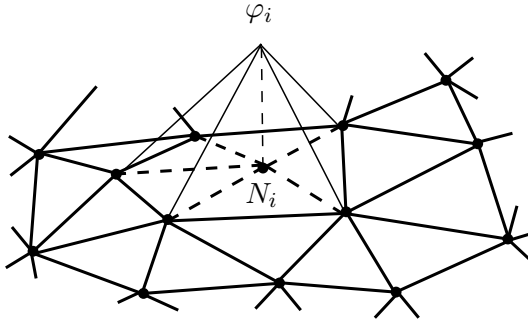


Figure 2.9.: Basis function φ_i of V_h in the FEM.

the name of the method). According to the definition the φ_i 's are zero in Ω except for the Ω_j 's adjacent to that node (see Figure 2.9). Since the φ_i 's are polynomials the local behavior of c can be reproduced very well. On the global domain Ω however, every φ_i interferes only with its direct neighbors. The resulting approximation c_h is therefore able to adapt locally as well as globally to c , which satisfies the first condition. Furthermore, Equation (2.33) will only give nonzero entries if φ_i and φ_j are defined on the same or on neighboring nodes. Thus, the FEM produces a system matrix L_h being sparse, which satisfies the second condition.

Due to the structure of Michaelis-Menten kinetics Equation (2.32) however, will be nonlinear (see Equation (2.24)). Accordingly, a nonlinear solver has to be applied.

Linearization and solution of the system In this study the *Newton* resp. *Newton-Raphson method* [Ypma, 1995] is applied for the solution of a nonlinear algebraic system. This method is an iterative solver, i.e. the required solution c_h is found by a series of approximations c_h^k . Starting with a reasonable first guess c_h^1 the following rule is applied:

$$c_h^k = c_h^{k-1} + J^{-1}(c_h^k) \left(L_h(c_h^k) - f_h \right). \quad (2.36)$$

Here J is the *Jacobian* of L_h , i.e. a matrix containing the first derivatives of L_h with respect to c_h . Therefore, one can write

$$J = L_h(c_h^k) + L'_h(c_h^k)c_h^k. \quad (2.37)$$

In Equation (2.36) the second term of the sum is called the correction

$$cor^k = J^{-1}(c_h^k)d^k \quad (2.38)$$

and

$$d^k = (L_h(c_h^k) - f_h) \quad (2.39)$$

the defect of every step k . By applying an appropriate damping factor λ

$$c_h^k = c_h^{k-1} + \lambda cor^k \quad (2.40)$$

the convergence of the Newton solver can be adjusted if necessary. By default λ is set to 1. A successful termination of the solver is reached if a suited norm of the defect $\|d^k\|$ is below a given threshold. An unsuccessful termination may occur if the threshold is not reached after a given number of iterations. Unlike the defect d^k , which has to be provided in every step, the Jacobian is only calculated if needed. A reasonable criteria is a bad *reduction* within a single step, i.e. $\|d^k\|/\|d^{k-1}\|$ remains below a given threshold.

2.7. The software toolbox UG

For the numerical solution of Equation (2.3) the software toolbox UG [Bastian et al., 1997] (abbreviation for *Unstructured Grids*) is used in this study. This toolbox provides a large collection of algorithms for the solution of partial differential equations. It furthermore provides a flexible framework so that new tools and algorithms suited for the actual problem can be implemented relatively easy. Tools for typical problems are provided by libraries, which can be accessed via a script language.

From the very beginning the development of UG has been focussed on easy parallelization of the code, flexible grid management as well as the implementation of multigrid solvers ([Hackbusch, 1985], [Bastian, 1996], [Lang, 2006]). Since then the toolbox has been used for works in the field of reactive transport ([Geiser, 2004], [Watson et al., 2005], [Neubauer and Bastian, 2005]) as well as related topics ([Nägele, 2003], [Blumschein, 2002]). The software is currently developed at the Goethe-University Frankfurt am Main in the research group of Prof. Gabriel Wittum at the Goethe Center for Scientific Computing [UGG]. The source code of this software collection can be downloaded free of charge on the website of the group for scientific purposes.

3. Upscaling of the advection-diffusion-reaction equation with Michealis-Menten kinetics

Abstract The need for reliable models for the reactive transport of contaminants in the subsurface is well recognized. The predictive power of these tools is challenged by the accurate description of the bioavailability of the contaminants to microorganisms in the porous medium. Among many other factors influencing bioavailability, diffusive mass-transfer processes may limit the substrate availability at the pore scale and hence reduce the effective degradation rate considerably. In this chapter we use a combination of analytical and numerical methods to upscale surface catalyzed Michealis-Menten kinetics within a single pore, to obtain effective rate expression at a larger scale. Results show that in the upscaled description Michealis-Menten kinetics leads to a concentration dependent transition between a reaction and diffusion limited regime. Strictly, the effective rate repression does not follow Michealis-Menten kinetics. However, we could present appropriate effective parameters relations, which provide a

good approximation of degradation dynamics using effective Michealis-Menten kinetics.

3.1. Introduction

Anthropogenic groundwater contamination is a severe problem in many industrialized countries. *Ex situ* remediation means, such as pump-and-treat systems, are often neither technically nor financially feasible due to the size of the contaminated sites. For many organic carbon compounds *in situ* bioremediation, either passive or enhanced, has shown to be a cost-effective alternative. Enhanced bioremediation uses the ability of subsurface microorganisms to degrade organic contaminants [Wiedemeier et al., 1999].

The biodegradation of groundwater contaminants has been extensively investigated, both in the field and in the laboratory. However, due to the complex interplay of microbial, chemical and physical processes occurring in groundwater, a direct quantification of *in situ* biodegradation is often hard to achieve. In order to judge the effectiveness of biodegradation on contaminated sites the experimental characterization is often combined with numerical simulations using reactive-transport models [Murphy and Ginn, 2000], [Barry et al., 2002], [Brun and Engesgaard, 2002], [Prechtel et al., 2006]. Yet, their predictive power is restricted by the accuracy of the implemented process descriptions.

The extrapolation of laboratory results on microbial degradation processes to *in situ* biodegradation processes in the field and the incorporation of these processes in reactive-transport simulations are - among many other aspects - challenged by finding an adequate description of the bioavailability of the substrate [Haws et al., 2006], [Thullner et al., 2007]. Factors controlling the bioavailability include the physico-chemical structure of the substrate [Bonneville et al., 2004], [Hyacinthe et al., 2006], physical occlusion by small pores [Mayer, 1994], [Zimmermann et al., 2004], [Knutson et al., 2005] or mineral coatings [Roden, 2004],

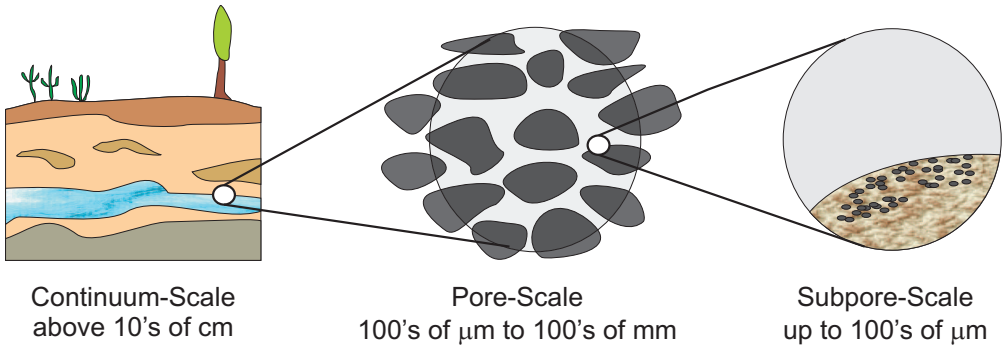


Figure 3.1.: Schematic of the complexity of the subsurface and the variety the different scales involved.

and macroscopic mixing processes [Cirpka et al., 1999], [Thullner et al., 2002a]. Most importantly, the bioavailability of a dissolved contaminant in porous media is highly affected by mass-transfer processes at the pore or sub-pore scale. The activity of microorganisms is controlled by substrate concentrations in their immediate vicinity [Harms, 1996], [Semple et al., 2003], [Kampara et al., 2009]. In porous media microorganisms primarily reside on the surface of the solid matrix (Fig. 3.1, right part). Microscopic transport processes within each pore must provide the supply of the contaminant from the bulk pore water to the location of the microbial cells. This transport limits bioavailability, besides any of the other processes mentioned above, which might impose an additional restriction to bioavailability. As a consequence, the bioavailable concentration, to which microorganisms are exposed to, may differ considerably from the average concentration measured at the macroscale [Raje and Kapoor, 2000] [Meile and Tuncay, 2006].

To understand the limitations of macroscopic degradation rates by such pore-scale mass fluxes, research has focused on simple representations of the pore space [Balakotaiah and Chang, 1995], [Knutson et al., 2007], [Lichtner and

Kang, 2007]. Looking at the pore scale it can be shown that the effective reaction rate can be significantly reduced when pore-scale diffusion becomes a limiting factor for bioavailability [Balakotaiah and Chang, 1995], [Bosma et al., 1997], [Dykaar and Kitanidis, 1996], [Kechagia et al., 2002], [Mikelić et al., 2006]. However, the reaction rate in most of these studies was assumed to follow first-order kinetics with respect to the concentration of the degraded species. In case of microbially catalyzed reactions first-order kinetics is valid for low concentrations only [Bekins et al., 1997]. In reality, the biodegradation of organic contaminants often follows Monod-type [Monod, 1949] respectively Michaelis-Menten kinetics [Michaelis and Menten, 1913]. Recently, Wood et al. [2007] have performed investigations assuming Michaelis-Menten kinetics within a single pore. They derived upscaling rules in the cases of either very low or very high substrate concentration. However, by comparing their upscaled equation with numerical simulations in a complex array of pores they got a mismatch for concentrations in the range of the Michaelis constant.

In this work we use a channel geometry comparable to Kechagia et al. [2002] and Balakotaiah and Chang [1995] but consider Michaelis-Menten kinetics for the reactive surface of the pore. We chose this simple geometry in order to be able to make use of analytical tools in the upscaling process. With our approach we aim to verify: (i) whether the upscaled reaction rate laws can be sufficiently described by effective Michaelis-Menten kinetics, and whether the problems reported by Wood et al. [2007] can be resolved and if yes: (ii) how the parameters of such effective Michaelis-Menten kinetics can be linked to microscopic reaction rate parameters that are valid at the local scale. The results obtained in this study for pore-scale systems may provide the base for interpreting results from laboratory column experiments. With further upscaling steps and additionally

taking into account large scale heterogeneities, our results can be applied for describing biodegradation efficiency at the field scale.

In the following sections of this paper we will first introduce the conceptual approach used in this study including the underlying equations, the geometric representation of the pore system, and the applied numerical schemes and upscaling concepts (Section 3.2). This is followed by the description of the analytical tools used to obtain explicit solutions for the microscale problems and effective equations for the macroscale continuum (Section 3.3). Analytical and numerical results are presented and discussed in Section 3.4 and final conclusions for the scaling behavior of bioavailability controlled Michaelis-Menten kinetics are given in Section 3.5.

3.2. Conceptual Model

This section describes the conceptual approach used in this study. This includes the governing equations describing transport and degradation of a reactive species as well as the pore geometry these equations are applied to. Furthermore, the applied upscaling concepts and numerical schemes are introduced.

3.2.1. Mathematical description

In the following we will derive the mathematical model for reactive transport at the pore scale. Starting with a general description we will introduce appropriate scaling units and apply a few simplifications before stating the definite mathematical description.

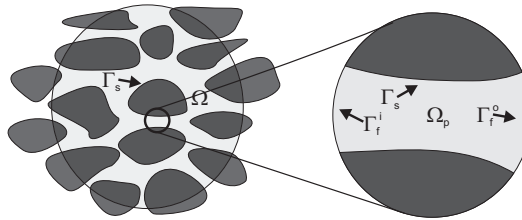


Figure 3.2.: Schematic of the computational domain.

The scale of interest is that of a single pore (Figure 3.2). All flow and transport processes are taking place in the fluid phase Ω , only. For a single pore, the boundaries of the fluid phase domain can be separated into a fluid–solid interface Γ_s and a fluid–fluid interface Γ_f . The latter can be further separated into the inlet boundary Γ_f^i and the outlet boundary Γ_f^o , each of them described by different boundary conditions. In a single pore, the fate of a single species with concentration c is described by (a) the advective diffusive transport in the

fluid phase, (b) microbial degradation following Michaelis-Menten kinetics at the fluid–solid interface, (c) a constant concentration along the inlet boundary, and (d) a zero-concentration gradient at the outlet boundary

$$\frac{\partial}{\partial t}c + V\nabla \cdot \tilde{\mathbf{v}}c = D\Delta c \quad \text{in } \Omega_p, \quad (3.1a)$$

$$D\nabla c \cdot \mathbf{n} = -\frac{q_{\max} c}{K_m + c} \quad \text{on } \Gamma_s, \quad (3.1b)$$

$$c = c_0 \quad \text{on } \Gamma_f^i, \quad (3.1c)$$

$$\nabla c \cdot \mathbf{n} = 0 \quad \text{on } \Gamma_f^o. \quad (3.1d)$$

Here, the water flux \mathbf{v} is given as $\mathbf{v} = V\tilde{\mathbf{v}}$, with V being the pore-scale average velocity and $\tilde{\mathbf{v}}$ the rescaled velocity, D is the molecular diffusivity, \mathbf{n} is the outer unit normal, q_{\max} is the maximum conversion rate and K_m is the Michaelis constant. The implementation of the reaction rate in Equation (3.1b) assumes the microorganisms to be localized at the solid liquid interface in a thin biofilm being constant in space and time.

Equations (3.1)a – (3.1c) were transferred into a non-dimensional form using reference lengths $L_{x,\text{ref}}$ and $L_{y,\text{ref}}$ as well as a reference concentration c_{ref} (values for $L_{x,\text{ref}}$, $L_{y,\text{ref}}$ and c_{ref} are addressed in Section 3.2.2). This allows for the definition of the following dimensionless variables

$$\hat{x} = \frac{x}{L_{x,\text{ref}}}, \quad \hat{y} = \frac{y}{L_{y,\text{ref}}}, \quad \hat{c} = \frac{c}{c_{\text{ref}}}, \quad \hat{K}_m = \frac{K_m}{c_{\text{ref}}}, \quad \text{and } \hat{t} = \frac{Dt}{L_{y,\text{ref}}^2}. \quad (3.2)$$

Furthermore, two dimensionless quantities are used: the Péclet number and the Thiele modulus. The Péclet number

$$Pe = \frac{VL_{y,\text{ref}}^2}{DL_{x,\text{ref}}} \quad (3.3)$$

indicates whether the advective or the diffusive transport is dominant at the scale of interest. High Péclet numbers mean advection dominates diffusion and vice versa. At the pore scale of groundwater systems, typical values of $L_{y,\text{ref}} < 1\text{mm}$ and $V < 1\text{m}/\text{d}$ result in values of $Pe \approx 10$ or below. This is in contrast to the continuum scale where Péclet numbers can be considerably higher. The Thiele modulus [Thiele, 1939]

$$\Phi^2 = \frac{q_{\max} L_{y,\text{ref}}}{DK_m} \quad (3.4)$$

compares the dynamics of the reactive consumption and the diffusive flux. This dimensionless quantity is related to the Damköhler numbers Da [Damköhler, 1937], commonly used in chemical engineering to relate the kinetics of reactions to mass-transfer processes [Fogler, 1998]. The Thiele modulus can be used to describe the bioavailability of a substrate [Myrold and Tiedje, 1985], [Chung et al., 1993]. In pore-scale systems Φ^2 as well as K_m can vary over several orders of magnitude. In our work we will focus on values comprising the transition from the reaction-limited to the diffusion-limited as well as from a first-order to a zeroth-order regime.

Using the definitions given by the Equations (3.2), (3.3) and (3.4) we write Equations (3.1a) – (3.1b)

$$\frac{\partial}{\partial \hat{t}} \hat{c} + Pe \nabla \cdot \tilde{\mathbf{v}} \hat{c} = \frac{L_{y,\text{ref}}^2}{L_{x,\text{ref}}^2} \frac{\partial^2}{\partial \hat{x}^2} \hat{c} + \frac{\partial^2}{\partial \hat{y}^2} \hat{c} \quad \text{in } \Omega_p, \quad (3.5a)$$

$$\nabla \hat{c} \cdot \mathbf{n} = - \frac{\Phi^2 \hat{c}}{1 + \hat{c}/\hat{K}_m} \quad \text{on } \Gamma_s. \quad (3.5b)$$

Equations (3.1c) – (3.1d) exhibit no significant changes using non-dimensional variables.

In the remainder of this publication, we will use the same symbols for dimensional as well as for non-dimensional variables. The occurrence of the Péclet number and the Thiele modulus in the equations will be the indicator whether dimensional or non-dimensional variables are considered.

Before stating the definite system of equations we will apply three simplifications justified by the scope of the study. First, we will drop the time derivative, since we are mainly interested in the steady state solution. Second, we restrict our analysis to travel paths of the contaminant with $L_{y,\text{ref}}^2 \ll L_{x,\text{ref}}^2$. This is corresponding to a flow path of the contaminant being effectively longer along than perpendicular to the flow field. Rephrasing this constraint as $L_{y,\text{ref}}^2/L_{x,\text{ref}}^2 \ll 1$ shows that we can neglect the longitudinal diffusion in Equation (3.5a). The assumption is for example supported by the findings of Liedl et al. [2005] who showed that the longitudinal dispersivity has practically no impact on the steady state plume length. The last simplification regards the velocity field, which has only a component in the direction along the flow path. With these simplifications and using the inlet boundary concentration as a reference ($c_{\text{ref}} = c_0$) the pore system is described by

$$Pe f(y) \frac{\partial}{\partial x} c = \frac{\partial^2}{\partial y^2} c \quad \text{in } \Omega_p, \quad (3.6a)$$

$$c = 1 \quad \text{on } \Gamma_f^i, \quad (3.6b)$$

$$\nabla c \cdot \mathbf{n} = -\frac{\Phi^2 c}{1 + c/K_m} \quad \text{on } \Gamma_s. \quad (3.6c)$$

Section 3.2: Conceptual Model

Equations (3.6a) – (3.6c) were used to perform all analysis presented in the following sections. The coefficient function $f(y)$ in Equation (3.6a) is a placeholder for an arbitrary velocity profile. Note that for first-order kinetics or $c \ll K_m$ Equation (3.6c) reads $\nabla c \cdot \mathbf{n} = -\Phi^2 c$.

3.2.2. Geometrical description

The pore system to which we apply Equations (3.6a) – (3.6c) is represented by a channel extending in x- and y-direction (Figure 3.3). A single pore with such a geometry will lead to a porous medium consisting of a compound of capillary tubes [Dupin et al., 2001b]. Compared to other two-dimensional arrays of single pores (e.g. [Knutson et al., 2007], [Lichtner and Kang, 2007], [Edwards et al., 1993]) this represents a simplification of the pore geometry, which is however, necessary in order to obtain analytical solutions in closed form expressions. Such a single pore system, although simple, has been proven to give appropriate indications on the relation between pore geometry, diffusion and reaction in general ([Kitanidis, 1992], [Paine et al., 1993]) and the geometry used here has previously been used by other authors to describe reactive processes in porous media [Kechagia et al., 2002] , [Mikelić et al., 2006], [van Duijn et al., 2008]. Results obtained for single pores can be transferred to more realistic porous media representations using the ratio of the reactive surface and the free volume as a scaling factor [Wood et al., 2007].

The reference length $L_{y,\text{ref}}$ is chosen to be half the width of the pore resulting in a pore space Ω_p given by the dimensionless coordinate ranges of $0 < x < \infty$ and $-1 < y < 1$. The reference length $L_{x,\text{ref}}$ is the characteristic length for which the concentration should be determined. As described in Equation (3.6b),

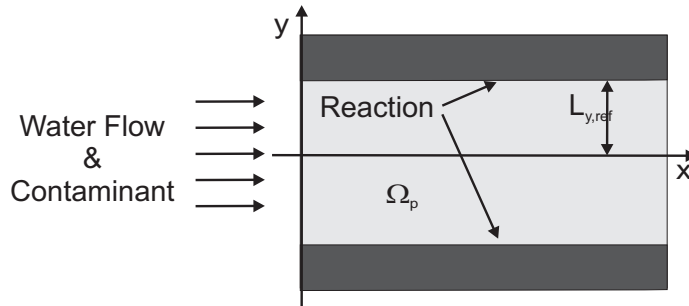


Figure 3.3.: Schematic sketch of the semi-infinite channel used to describe processes in a single pore.

the fixed concentration considered at the inlet boundary is used as reference concentration c_{ref} .

The pore space, the boundaries and thus all obtained solutions of Equations (3.6a) – (3.6c) are symmetric with respect to the x -axis (Figure 3.3). For this reason the domain was split along the y -axis. All analytical and numerical solutions were calculated for $0 < y < 1$, considering $\nabla c \cdot \mathbf{n} = 0$ as boundary condition at $y = 0$.

3.2.3. Scenarios considered for calculations

In Equation (3.6a) the form of the coefficient function regarding the velocity profile was not further specified. For the given pore geometry a parabolic profile is the most realistic velocity distribution [Taylor, 1953], [Aris, 1956]. The focus of this study is on the scaling behavior of Michaelis-Menten kinetics. However, in order to verify the results of our approach with those presented and discussed in the literature for first-order kinetics and uniform velocity profiles [Kechagia et al., 2002], we here consider the same in form of scenario I. Next to the most simple (scenario I) and the most realistic scenario (scenario IV), two further

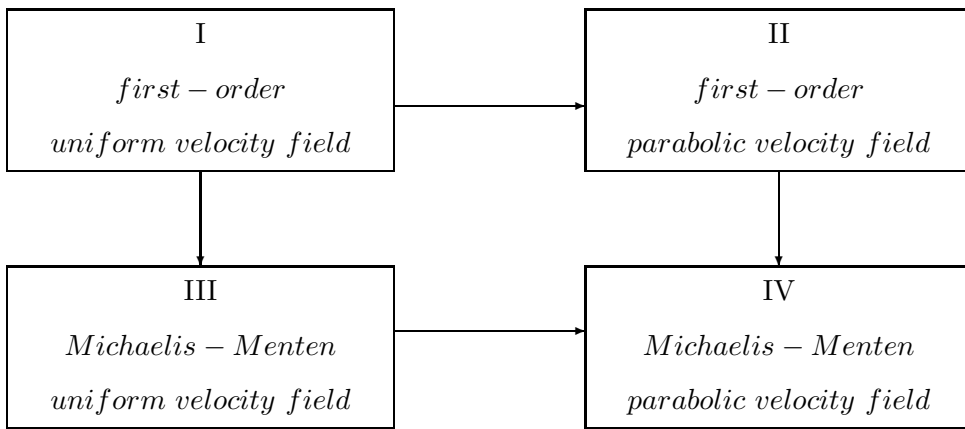


Figure 3.4.: Schematic of the different scenarios (I - IV) investigated in this study.

scenarios (II and III) of intermediate complexity were considered (Figure 3.4). In scenarios II and III the remaining combinations of reaction kinetics and velocity profile were addressed to investigate the influence of each individual feature on the obtained results.

3.2.4. Upscaling of the pore-scale processes

The focus of this study is to use upscaling methods to obtain an effective one-dimensional representation of the system described by Equation (3.6). Generally the purpose of upscaling is to find an effective description of the process of interest on a coarse level by starting with a well defined representation of the process on a fine level. The most common methods for upscaling in subsurface

hydrology [Renard and de Marsily, 1997], [Wood, 2008] are homogenization [Bakhvalov and Panasenko, 1989], [Papanicolaou, 1995] and volume averaging [Whitaker, 1999].

To arrive at an effective representation we have to average the process over the y -axis (Figure 3.3). The scheme of the upscaling process used in this study is outlined in Figure 3.5.

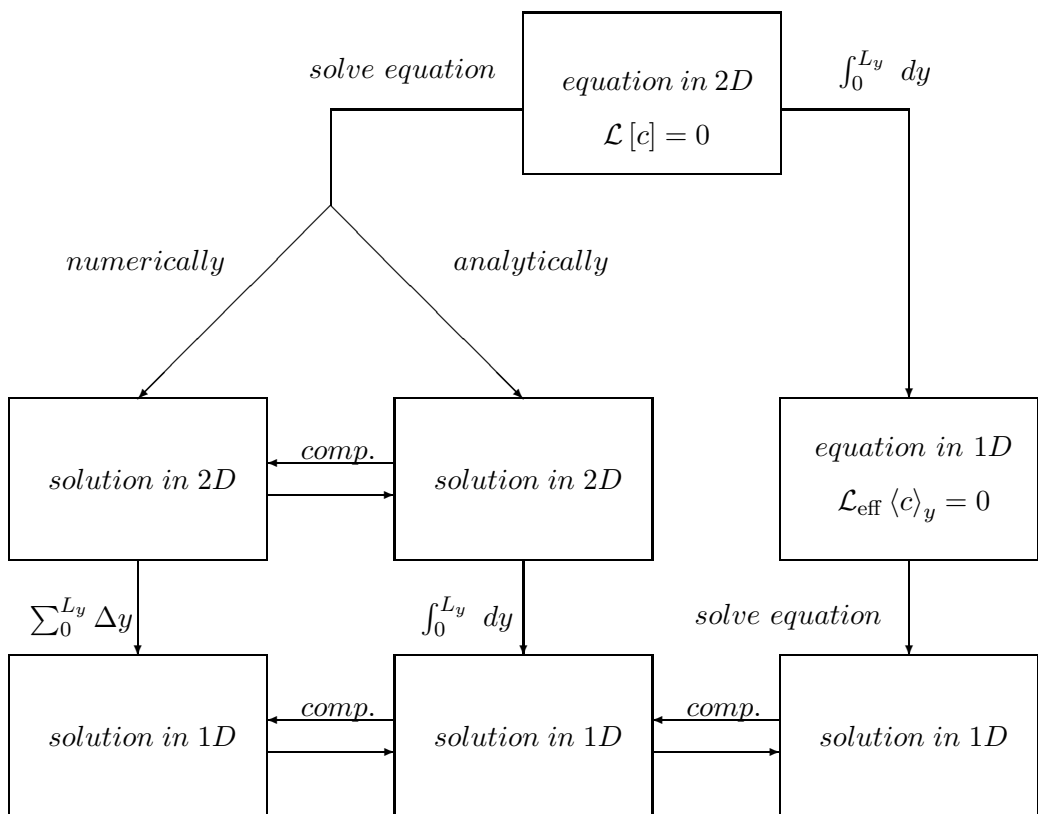


Figure 3.5.: Schematic of the upscaling process

Starting point of the analysis is the system of two-dimensional partial differential equations as given by Equations (3.6a) – (3.6c). The most 'straight forward' analysis is first solving these equations either numerically or analytically (left side of Figure 3.5). The resulting two-dimensional concentration distribution is then averaged over the width of the pore (i.e., the y -axis; Figure 3.3) providing a one-dimensional concentration profile along the length of the pore. The derived concentration profiles were used as references for an alternative approach where the steps of analytical solution and averaging are permuted (right side of Figure 3.5). In the latter approach, first the averaging over the y -axis results in a new one-dimensional effective differential operator \mathcal{L}_{eff} with a reduced complexity but new effective parameters (see Section 3.3). The evaluation of these parameters is the main part of the analytical upscaling process. After that, the upscaled parameters are used to calculate an effective solution (one-dimensional concentration profile along the length of the pore). A comparison between the solutions is a good measure for the accuracy of the effective parameters (Figure 3.5).

3.2.5. Numerical scheme

To support the analytically derived results numerical solutions for Equations (3.6a) – (3.6c) were calculated (see Figure 3.5). These numerical simulations were performed using the software platform UG ('*U*nstructured *G*rids', [Bastian et al., 1997]). Steady state results were obtained by simulating a transient problem with arbitrary initial conditions until steady state was reached. The time derivative is discretized by the one-step implicit Euler method. In order to ensure the local mass conservation, the mixed finite element method is applied for the spatial discretization. More precisely, the lowest order finite elements of

Raviart-Thomas type are used for the approximation of the fluxes and piecewise constants for the concentrations. The resulting algebraic system of equations is hybridized by adding Lagrange multipliers on the edges according to Radu et al. [2008, 2009]. Then the nonlinear problem is linearized by a damped Newton method and the resulting linear systems are solved by a multigrid algorithm.

3.3. Upscaling and Analytical Methods

In this section we present (i) analytical solutions for the coupled transport degradation problem in two-dimensions and the subsequent averaging over the y -axes, as well as (ii) one-dimensional effective equations obtained by the upscaling theory (see schematic in Figure 3.5). Both approaches are first applied for first-order kinetics and afterwards modified to solve the case of Michaelis-Menten kinetics.

3.3.1. First-order kinetics

Assuming first-order kinetics, Equation (3.6c) can be written as

$$\nabla c \cdot \mathbf{n} = -\Phi^2 c_{\text{bio}} \quad (3.7)$$

introducing c_{bio} as $c(x, y)|_{y=1}$, i.e. the concentration available to the surface bound microorganisms. To solve the resulting system of equations we assume the concentration to be given as an infinite sequence of modes

$$c(x, y) = \sum_{i=1}^{\infty} C_i(x) \Psi_i(y). \quad (3.8)$$

This ansatz separates every mode into a longitudinal and a transversal component (relative to the flow direction), under the assumption that the velocity field is constant along the longitudinal direction. Thus both sides of Equation (3.8) are not coupled by the coefficient function $f(y)$ from Equation (3.6a). A comprehensive discussion on the solution of Equation (3.8) can be found in Appendix A.1.1. As a result we get the following expression

$$\mathbf{T} \frac{\partial}{\partial x} \mathbf{C} = \boldsymbol{\Lambda} \mathbf{C}, \quad (3.9)$$

which can be rearranged to

$$\frac{\partial}{\partial x} \mathbf{C} = \mathbf{T}^{-1} \boldsymbol{\Lambda} \mathbf{C} = \boldsymbol{\Gamma} \mathbf{C}. \quad (3.10)$$

The entries of the unknown vector \mathbf{C} are the longitudinal modes C_i of the concentration c . The entries of the system matrix $\boldsymbol{\Gamma}$ depend on the velocity field $f(y)$. In this form Equation (3.10) represents a system of linear ordinary differential equations. In the following subsections we will solve this system for the cases of a uniform and a parabolic velocity field.

3.3.1.1. Uniform velocity field

For a uniform velocity field the coefficient function in Equation (3.6a) is given by $f(y) = 1$.

Analytical Solution For this velocity field the system matrix $\boldsymbol{\Gamma}$ is diagonal so the single longitudinal modes are decoupled

$$C_i(x) = A_i \frac{\sin(\lambda_i)}{\lambda_i} e^{-\frac{\lambda_i^2}{Pe} x}. \quad (3.11)$$

For a comprehensive derivation of this solution and the calculation of the coefficients A_i and λ_i see Appendix A.1.2. The y -averaged solution can be written as

$$C(x) = \sum_{i=1}^N e^{-\frac{\lambda_i^2}{Pe} x} \frac{4 \sin^2(\lambda_i)}{\lambda_i (\sin(2\lambda_i) + 2\lambda_i)}. \quad (3.12)$$

Section 3.3: Upscaling and Analytical Methods

From Equation (3.11) it can be concluded, that only the first few modes are required to obtain a good approximation of $C(x)$. Since the elements of $\{\lambda_i\}_{i \geq 1}$ are monotonously increasing (see Figure A.1) the respective modes exhibit a steeper exponential decay. Furthermore, the coefficients A_i in Equation (3.11) are decreasing with increasing i (see Equation (A.7)). Consequently, the contribution of higher modes to $C(x)$ is insignificant.

Effective Equation Details on the direct upscaling of the system given by Equations (3.6a) – (3.6c) can be found in Appendix A.1.2. As a result of this procedure we get the following differential equation

$$\frac{\partial}{\partial x} C(x) = -\frac{\Phi_{\text{eff}}^2}{Pe} C(x), \quad (3.13)$$

which exhibits a first-order dependency on the y -averaged concentration. The new effective coefficient Φ_{eff}^2 will be discussed in Section 3.4.1 in more detail.

3.3.1.2. Parabolic velocity field

For a parabolic velocity field the coefficient function in Equation (3.6a) is now given by $f(y) = 1.5(1 - y^2)$. The details of the determination of the analytical solution as well as the effective equation are given in Appendix A.1.3.

Analytical Solution For this velocity field the different modes of the unknown vector \mathbf{C} are now coupled and have to be diagonalized before they can be solved in analogy to Equation (3.11). Consequently we get

$$w_i(x) = w_i(0)e^{-d_{ii}x}, \quad (3.14)$$

where d_{ii} are the entries of the diagonalized Matrix $\mathbf{\Gamma}$ from Equation (3.10) and the vector of the initial conditions is $\mathbf{w}(0) = \mathbf{G}^{-1}\mathbf{C}(0)$. The required solution is then found by re-transforming the solution of Equation (3.14).

Effective Equation For a parabolic velocity field we get an ordinary, second order differential equation for the first mode of the concentration

$$v_{\text{eff}} \frac{\partial}{\partial x} C_1(x) = D_{\text{eff}} \frac{\partial^2}{\partial x^2} C_1(x) + R_{\text{eff}} C_1(x) \quad (3.15)$$

In comparison to Equation (3.13) new transport parameters v_{eff} and D_{eff} are introduced. Since all quantities in Equation (3.15) are non-dimensionalized these effective parameters represent the ratio between the microscale and the physically effective values. The transport parameters can be determined by solving Equation (A.17)

$$v_{\text{eff}} = \tau_{11} + \tau_{22} \frac{\lambda_1^2}{\lambda_2^2}, \quad (3.16a)$$

$$D_{\text{eff}} = \frac{Pe}{\lambda_2^2} (\tau_{21}\tau_{12} - \tau_{11}\tau_{22}) \text{ and} \quad (3.16b)$$

$$R_{\text{eff}} = -\frac{\lambda_1^2}{Pe}. \quad (3.16c)$$

Here τ_{ij} are the entries of the matrix \mathbf{T} from Equation (3.9). Note that the representation of the effective parameters is arbitrary. The present form has been chosen such that R_{eff} is a good approximation of the reaction rate in the former scenario (see Equation (A.18)).

3.3.2. Michaelis-Menten kinetics

For Michaelis-Menten kinetics given by Equation (3.6c) the coefficients $\lambda_i(x)$ are now x -dependent so Equation (3.10) must be modified

$$\frac{\partial}{\partial x} \mathbf{C} = \boldsymbol{\Gamma}(x) \mathbf{C}. \quad (3.17)$$

Further details on the calculations are again given in the Appendix A.1.4. The solution of Equation (3.17) depends on the velocity field $f(y)$ and is in the following discussed in analogy to Section 3.3.1.

3.3.2.1. Uniform velocity field

Analytical Solution As mentioned above in the case of a uniform velocity field all modes in Equation (3.10) are decoupled. Therefore, each single mode $C_i(x)$ is given by the differential equation

$$\frac{\partial}{\partial x} C_i(x) = -\gamma_{ii} C_i(x). \quad (3.18)$$

Here γ_{ii} are the respective entries of $\boldsymbol{\Gamma}(x)$ from Equation (3.17). Due to the x -dependency of the coefficient function we have to modify Equation (3.11) to

$$C_i(x) = A_i(0) \frac{\sin(\lambda_i(0))}{\lambda_i(0)} e^{-\int_0^x \gamma_{ii}(x') dx'}. \quad (3.19)$$

This leads to the y -averaged solution for the concentration

$$C(x) = \sum_{i=1}^N \frac{4 \sin(\lambda_i(0)) \sin(\lambda_i(x)) e^{-\int_0^x \gamma_{ii}(x') dx'}}{\lambda_i(0) \lambda_i(x) \sqrt{\sin(2\lambda_i(0)) + 2\lambda_i(0)} \sqrt{\sin(2\lambda_i(x)) + 2\lambda_i(x)}}. \quad (3.20)$$

Due to Michaelis-Menten kinetics being nonlinear the coefficients λ_i depend on the solution c . Therefore, Equation (3.19) has to be solved iteratively. Using the solution for first-order kinetics as an initial guess c^0 , we solve the system to get the new approximation c^1 and iterate the proceedings. The fixed point c^* of the iterative loop is then the required solution. Although, we have not proven the convergence of the iteration scheme, we see it numerically. Moreover, for all investigated parameter settings we see a good agreement between the semi-analytical solution and the numerically calculated solution (see Section 3.4).

Effective Equation The direct upscaling described above for first-order kinetics is now applied using Equation (A.26) instead of (3.7). This leads to

$$Pe \frac{\partial}{\partial x} C = - \frac{\Phi^2 c_{\text{bio}}}{1 + c_{\text{bio}}/K_m}. \quad (3.21)$$

Furthermore, we introduce a new coefficient function

$$K_{m,\text{eff}} = \frac{C}{c_{\text{bio}}} K_m. \quad (3.22)$$

With this new effective Michaelis constant and the effective Thiele modulus Φ_{eff}^2 , given in analogy to Equation (A.23), we obtain

$$Pe \frac{\partial}{\partial x} C = - \frac{\Phi_{\text{eff}}^2 C}{1 + C/K_{m,\text{eff}}}. \quad (3.23)$$

Both effective coefficient functions Φ_{eff}^2 and $K_{m,\text{eff}}$ are scaled by the same scaling factor

$$\eta = \frac{c_{\text{bio}}}{C}, \quad (3.24)$$

Section 3.3: Upscaling and Analytical Methods

which is the ratio of the bioavailable concentration c_{bio} and the y -averaged or upscaled concentration C . Using Equation (3.24), we can rewrite Equation (3.23) to obtain an analytical expression of the governing differential equation for the upscaled concentration C

$$Pe \frac{\partial}{\partial x} C = - \frac{\Phi^2 C}{1/\eta + C/K_m}. \quad (3.25)$$

If the coefficients Φ_{eff}^2 and $K_{m,\text{eff}}$ are constant and if $C(0) = 1$ is used as boundary condition, the analytical solution of Equation (3.23) is given by

$$C = K_{m,\text{eff}} \text{Lambert}W \left(\frac{e^{1 - \frac{\Phi_{\text{eff}}^2}{Pe K_{m,\text{eff}}} x}}{K_{m,\text{eff}}} \right). \quad (3.26)$$

The function $\text{Lambert}W(z)$ is the solution of $z = we^w$ (see [Corless et al., 1997]), which has already been used in the context of microbial reaction kinetics (e.g, [Schnell and Mendoza, 1997], [Helfgott and Seier, 2007]). Comparing Equation (3.26) to the analytical or numerical solutions of the two-dimensional problem allows to obtain direct estimates for the effective parameters Φ_{eff} and $K_{m,\text{eff}}$.

3.3.2.2. Parabolic velocity field

Analytical Solution Because of the x -dependency of the coefficients $\lambda_i(x)$, Equation (3.19) has to be modified in analogy to Equation (3.11):

$$\begin{aligned}\mathbf{C}' &= \mathbf{\Gamma}(x)\mathbf{C} = \mathbf{G}(x)\mathbf{D}(x)\mathbf{G}^{-1}(x)\mathbf{C} \\ \mathbf{G}^{-1}(x)\mathbf{C}' &= \mathbf{D}(x)\mathbf{G}^{-1}(x)\mathbf{C} \\ \mathbf{w}' &= \mathbf{D}(x)\mathbf{w}.\end{aligned}$$

By decoupling the system we have arrived at a form comparable to Equation (3.17). The analytical solution in analogy to Equation (3.19) is now

$$w_i(x) = w_i(0)e^{-\int_0^x d_{ii}(x')dx'}. \quad (3.27)$$

The required solution is found by re-transforming the solution of Equation (3.27).

Effective Equation As in the case of first-order kinetics with a parabolic velocity field, no closed solution for the direct upscaling exists. However, by applying a similar scheme as used for first-order kinetics we can derive an effective equation for the first longitudinal mode $C_1(x)$

$$v_{\text{eff}}(x)\frac{\partial}{\partial x}C_1(x) = D_{\text{eff}}(x)\frac{\partial^2}{\partial x^2}C_1(x) + R_{\text{eff}}(x)C_1(x). \quad (3.28)$$

All coefficients of the effective Equation (3.28) are now x -dependent functions. Their evaluation has therefore, become cumbersome for practical applications compared to the case of first-order kinetics. Nonetheless, these coefficient functions are useful for theoretical considerations

$$v_{\text{eff}} = 1 + \frac{\gamma_{11}}{\gamma_{22}} - \frac{\gamma_{12}}{\gamma_{22}} \frac{\partial}{\partial x} \frac{1}{\gamma_{12}}, \quad (3.29a)$$

$$D_{\text{eff}} = -\frac{1}{\gamma_{22}} \text{ and} \quad (3.29b)$$

$$R_{\text{eff}} = (\gamma_{11} - \frac{\gamma_{12}\gamma_{21}}{\gamma_{22}} - \frac{\gamma_{12}}{\gamma_{22}} \frac{\partial}{\partial x} \frac{\gamma_{11}}{\gamma_{12}}). \quad (3.29c)$$

$$(3.29d)$$

Here the coefficients γ_{ij} are the entries of the system matrix $\boldsymbol{\Gamma}$ of Equation (3.17). The increase in complexity is attributed to the new mixing terms for the effective velocity v_{eff} and the effective reaction term R_{eff} . Though the effective dispersion D_{eff} contains no additional terms all coefficient functions are x -dependent (see also Equation (3.23)).

3.3.3. Synopsis of analytical methods

In Table 3.1 a summary of the analytical solutions and effective equations derived from Equations (3.6a) – (3.6c) for the different pore velocity profiles and reaction rates is given. For first-order kinetics our results are comparable to those found in the literature [Kechagia et al., 2002], [Balakotaiah and Chang, 1995]. In the case of the parabolic velocity field the effective equation only provides results for the first mode. The introduced error by neglecting higher modes is confined to small values of x .

	First-order kinetics		Michaelis-Menten kinetics	
	analytical	effective	analytical	effective
uniform vel. profile	(3.12)	(3.13)	(3.20)	(3.23)
parabolic vel. profile	(3.14)	(3.15)	(3.27)	(3.28)

Table 3.1.: Summary of cases and corresponding equations.

3.4. Results and Discussion

In this section we first present and discuss the analytical and numerical results obtained by applying the different approaches outlined in Figure 3.5 for different combinations of velocity fields and reaction kinetics (see Figure 3.4). Calculated values of the effective parameters used in the one-dimensional up-scaled equation, and the dependency of these parameters on local parameters are evaluated. Finally, the applicability of effective Michaelis-Menten kinetics is discussed.

3.4.1. First-order kinetics with uniform velocity field

The case of first-order kinetics with a uniform velocity field is well studied in the literature [Kechagia et al., 2002]. We briefly review and compare those results vis-à-vis our numerical findings. Calculated concentration profiles exhibit an exponential decrease along the x -direction and a cosine-like profile along the y -direction (see Figure 3.6 for an arbitrary example). The strong gradient in the y -direction shows that the transversal diffusion is not fully able to transport the contaminant from the bulk of the domain to the reactive boundary at $y = \pm 1$. The y -averaged profile of the numerical and the analytical solution match very

Section 3.4: Results and Discussion

well in all investigated scenarios, which indicates the soundness of the used numerical scheme.

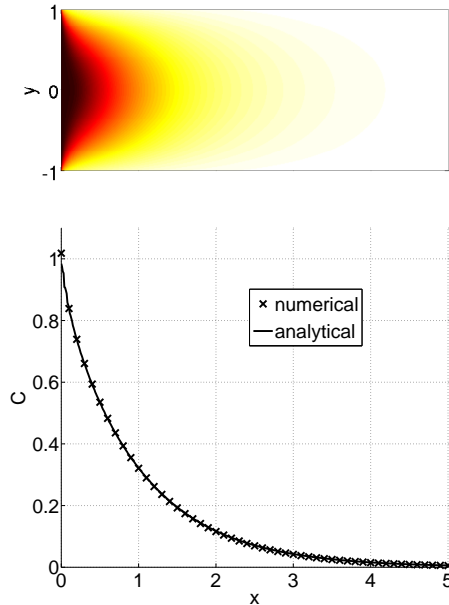


Figure 3.6.: Examples for first order reaction rate with uniform velocity field.

The local parameters are $\Phi^2 = 10$ and $Pe = 2$. Top: simulated two-dimensional results. Bottom: comparison of one-dimensional analytical and numerical solutions.

Calculated values for Φ_{eff}^2 , using Equation (3.13), show a hyperbolic behavior with respect to Φ^2 (Figure 3.7). Consequently, we can identify three different regimes. The first one is termed *reaction-limited* and is valid for low Φ^2 values. Here Φ_{eff}^2 shows a nearly linear dependency and the scaling unit η is accordingly close to 1. This indicates a strong coupling between the local and global behavior. Thus, the reaction in this regime is sufficiently slow for the transversal diffusion to provide the reactive boundary with enough substrate. The bioavailable concentration c_{bio} is therefore nearly the same as the

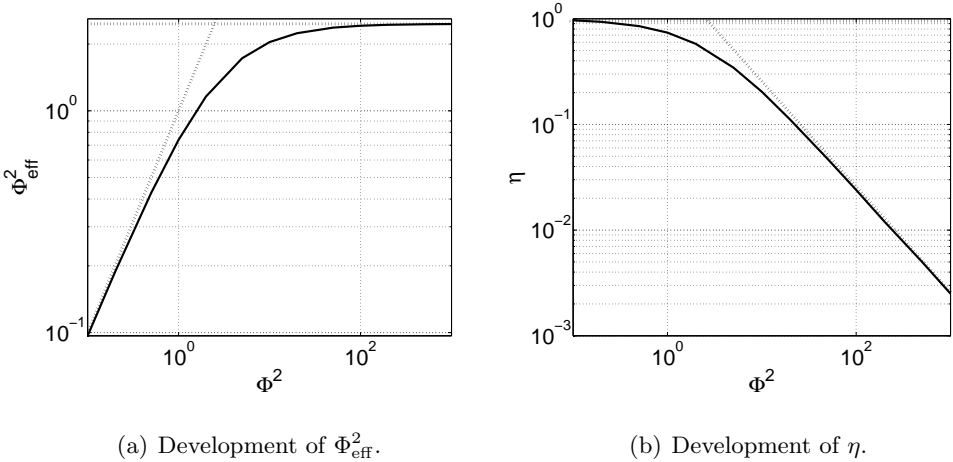


Figure 3.7.: Dependency of Φ_{eff}^2 and η on Φ^2 in case of first-order kinetics with a uniform velocity field. Together with the linear and constant asymptotes representing the reaction-limited (reached for low values of Φ^2) and the diffusion limited regime (reached for high values of Φ^2). The value of Φ_{eff}^2 has been evaluated using Equation (A.23).

y -averaged concentration C . As a result the upscaled reaction rate is mostly governed by the small scale reaction henceforth the name. The second regime is called *diffusion-limited* and is valid for high values of Φ^2 . Here Φ_{eff}^2 asymptotically approaches $\pi^2/4$, corresponding to a linear decrease of η (Figure 3.7). In this regime the reaction is too fast for the transversal diffusion to transport sufficient amounts of substrate to the reactive boundary. As a result, strong concentration gradients occur along the width of the pore and the bioavailable concentration is much smaller than the y -averaged concentration, i.e. $c_{\text{bio}} \ll C$. The third regime is the transition zone between the two other regimes and is characterized by reaction as well as diffusion. Both are limiting processes and control the upscaled behavior. These findings agree with results from the liter-

Section 3.4: Results and Discussion

ature [Kechagia et al., 2002], [Wood et al., 2007], which in case of Wood et al. [2007] also shows that, by applying appropriate scaling steps, the results from a simple geometry can be extended to more realistic scenarios.

3.4.2. First-order kinetics with parabolic velocity field

All other boundary conditions assuming the same as in Section 3.4.1, we discuss the case of first-order kinetics with a parabolic velocity field. As noted in Section 3.2, this case has been discussed in the literature [Balakotaiah and Chang, 1995], but for different conditions as considered here. Nevertheless, our results are similar to those previously reported. Calculated concentration profiles for a parabolic velocity field (Figure 3.8) show only minor differences to profiles obtained for a uniform velocity field. For small values of x , i.e. close to the inlet, y -averaged concentrations are slightly smaller in the case of a parabolic velocity field. For increasing x however, higher concentrations are observed for the parabolic velocity field.

The differences between the two velocity fields can be attributed to the occurrence of the effective dispersion coefficient D_{eff} and the effective velocity v_{eff} (see Equation (3.15)), which result in a faster transport of substrate along the length of the pore. The relation between the effective velocity v_{eff} and Φ^2 depends on the regime governing the overall consumption of the substrate (see Figure 3.9a). In the reaction-limited regime the effective velocity is close to 1 (i.e., equal to the average flow velocity) and both, uniform and parabolic velocity fields, yield almost identical results. The effective velocity increases with increasing Φ^2 and eventually saturates for high Φ^2 -values in the diffusion-limited regime. In the latter regime strong transversal concentration gradients exist and highest concentrations correlate with highest flow velocities. As a result the bulk of

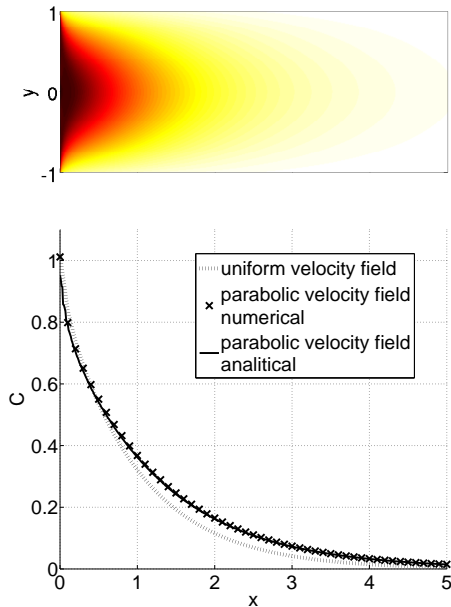


Figure 3.8.: Examples of first-order kinetics with a parabolic velocity field. The local parameters are $\Phi^2 = 10$ and $Pe = 2$. Top: simulated two-dimensional results. Bottom: comparison of one-dimensional analytical and numerical solution with results for a uniform velocity field.

the substrate mass is transported faster downstream. The effective dispersion coefficient D_{eff} remains small compared to the molecular diffusion coefficient (i.e., $D_{\text{eff}} < 1$) and shows a reverse dependency on Φ^2 than observed for v_{eff} (see Figure 3.9b). The steep gradient at the immediate vicinity of pore inlet (Figure 3.8) is caused by the uniform constant concentration distribution used as boundary condition along the entire inlet. This results in high substrate concentrations at the reactive pore wall, leading to reaction rates that are not limited by any transversal mass transfer at the vicinity of the inlet.

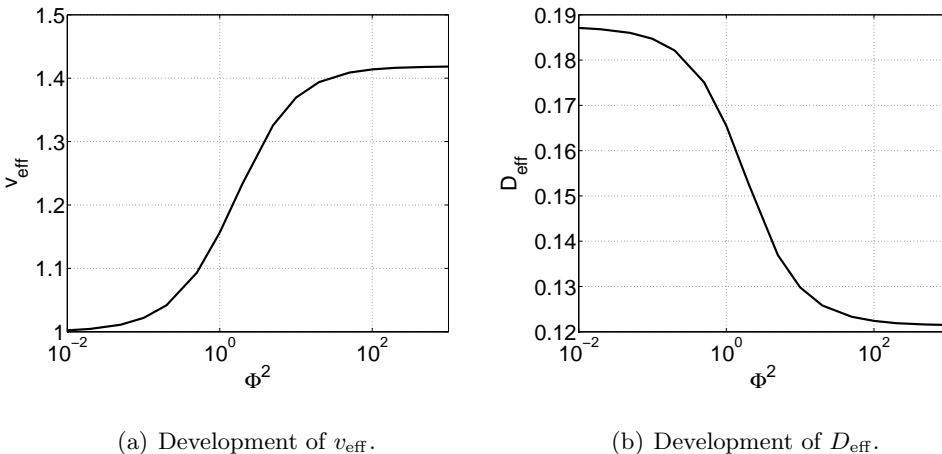


Figure 3.9.: Dependency on the effective parameters v_{eff} and D_{eff} from Φ^2 for the case of first-order kinetics with a uniform velocity field. The values were evaluated by solving the Equations (3.16a) and (3.16b)

3.4.3. Michaelis-Menten kinetics with uniform velocity field

For the combination of Michaelis-Menten kinetics and uniform velocity field analytical and numerical results agree well (Figure 3.10) which confirms the semi-analytical scheme used for the analysis. The two-dimensional concentration distribution obtained for Michaelis-Menten kinetics (Figure 3.10 top) is qualitatively similar to the one presented above for first-order kinetics (Figure 3.6 top). The one-dimensional concentration profile, however, shows a clear contrast between the two cases (Figure 3.10 bottom). At high y -averaged concentrations C , the concentration decrease is much weaker for Michaelis-Menten kinetics because at these concentrations the upscaled reaction rate approximately follows zeroth-order kinetics. The slope of the concentration profile is therefore nearly linear in contrast to the exponential decrease observed for first-

3.4.3 Michaelis-Menten kinetics with uniform velocity field

order kinetics. Only when C drops to small values (i.e., $C \leq K_m$), the upscaled reaction rate approaches first-order kinetics. This qualitative analysis shows, that in the upscaled equations the characteristics of Michaelis-Menten kinetics is preserved.

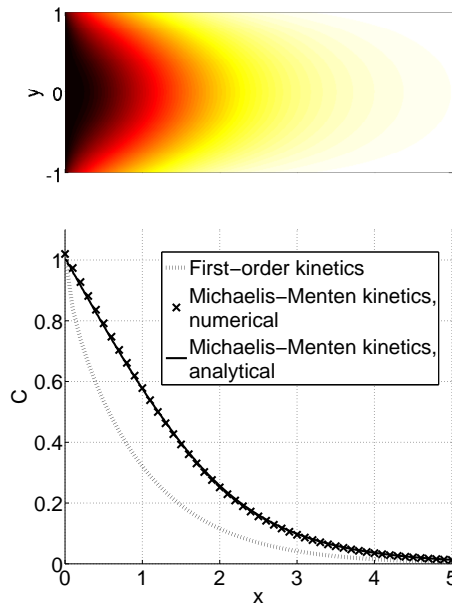
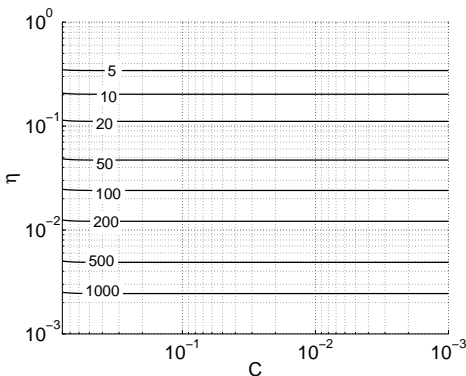


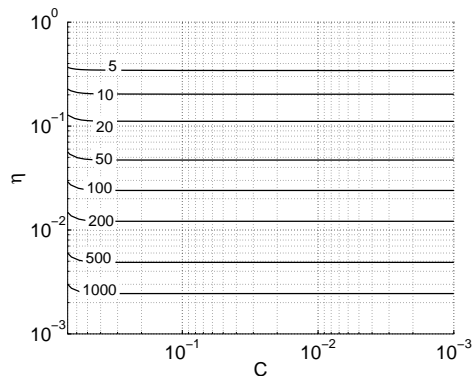
Figure 3.10.: Examples for Michaelis-Menten kinetics with uniform velocity field. The local parameters are $\Phi^2 = 10$, $Pe = 2$ and $K_m = 0.1$. Top: simulated two-dimensional solution. Bottom: comparison of analytical and numerical one-dimensional solutions with results from first-order kinetics.

As in case of first-order kinetics the scaling parameter η describes the coupling between local and global parameters (Equation (3.25)). Compared to the former case, where η does not depend on C (the slight variations for $C \approx 1$ are attributed to the inlet boundary conditions), the behavior of η is more complex for Michaelis-Menten kinetics. The parameter now depends on the y -averaged

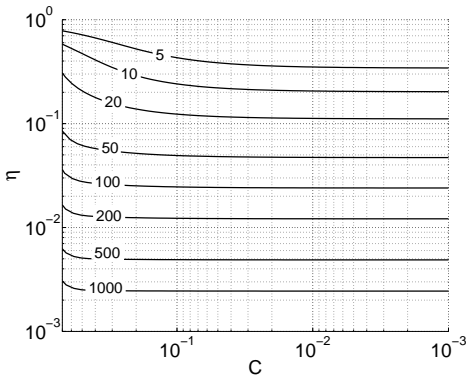
Section 3.4: Results and Discussion



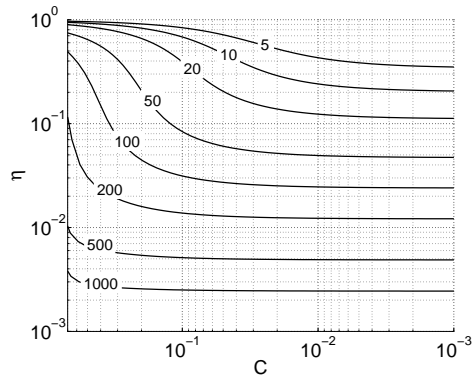
(a) Development of η for first-order kinetics.



(b) Development of η for $K_m = 1$.



(c) Development of η for $K_m = 0.1$.



(d) Development of η for $K_m = 0.01$.

Figure 3.11.: Development of η for different Φ^2 and K_m for the case of Michaelis-Menten kinetics with uniform velocity field. The respective value of Φ^2 are tagged along the curves. The results were evaluated by using Equation (3.24).

concentration C (Figure 3.11a) approaching a constant value only for sufficiently small concentrations ($C \ll K_m$; Figure 3.11b-d). Besides the sensitivity

3.4.4 Michaelis-Menten kinetics with parabolic velocity field

of η towards K_m , results also vary with Φ^2 . Lower values of Φ^2 extend the concentration range where η depends on C .

This characteristic allows to distinguish between three different regimes: an effective zeroth-order, an effective first-order and a transition regime. For an effective zeroth-order regime with $K_m \ll C$, η is nearly constant and close to 1. This regime is characterized by a combination of high concentration values and low values of Φ^2 (Figure 3.11d in the upper left part). For $K_m \approx C$ we have a transition regime where η , and therefore the correlation between the local and the global parameters, shows a strong dependency on C . In the third regime, characterized by low concentrations and/or high Φ^2 , η is well approximated by constant values representing an effective first-order regime, i.e. $K_m > C$. A comparison of Figures 3.11a, 3.11b, 3.11c and 3.11d shows that the behavior of η for high values of Φ^2 is very similar for all K_m . Therefore, the results for first-order kinetics can be applied to Michaelis-Menten kinetics with high values of Φ^2 .

3.4.4. Michaelis-Menten kinetics with parabolic velocity field

This case is the most complex of the scenarios investigated and the obtained results (Figure 3.12) represent a combination of the effects discussed in Sections 3.4.3 and 3.4.2.

As for first-order kinetics, a reaction-limited and a diffusion limited regime can be distinguished. The behavior of the upscaled equation in the reaction-limited case (see Figure 3.13a) can qualitatively be understood as a superposition of the cases described in Section 3.4.2 and 3.4.3. Compared to the uniform velocity field, the concentration decreases relatively sharp in the vicinity of the inlet but

Section 3.4: Results and Discussion

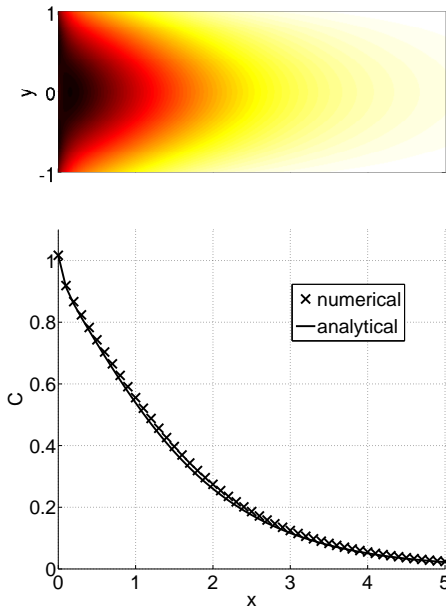


Figure 3.12.: Examples for Michaelis-Menten kinetics with a parabolic velocity field. The local parameters are $\Phi^2 = 10$, $K_m = 0.1$, and $Pe = 2$. Top: simulated two-dimensional solution. Bottom: comparison of analytical and numerical one-dimensional solutions.

exhibits weaker gradients further downstream of the pore. These effects have already been discussed in Section 3.4.2. Furthermore, for Michaelis-Menten kinetics, a zeroth-order behavior is observed for high concentrations and a first-order behavior for low concentrations (see Subsection 3.4.3). In contrast, for the diffusion-limited regime the upscaled concentration profiles show a similar dependency on the velocity field. The results for the first-order and Michaelis-Menten kinetics are almost identical (see Figure 3.13b). This again emphasizes that the relation between diffusion and reaction rate determines the upscaled behavior.

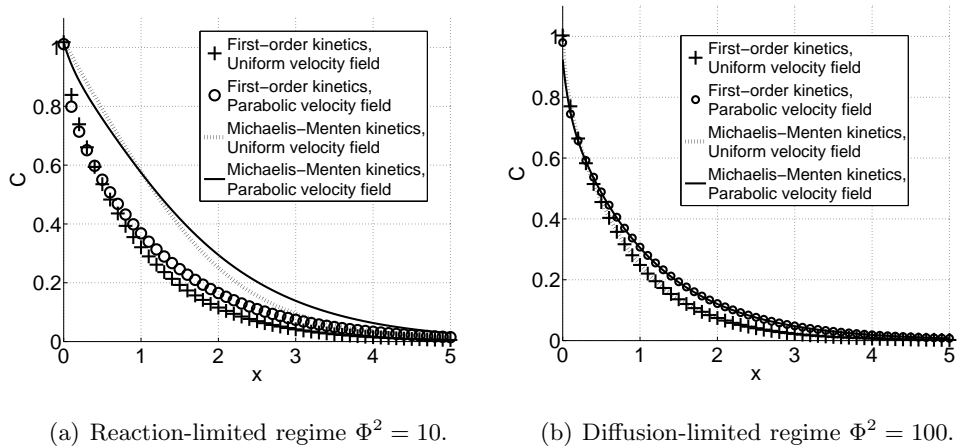


Figure 3.13.: Examples for Michaelis-Menten kinetics with a parabolic velocity field. The local parameters are $K_m = 0.1$ and $Pe = 2$.

3.4.5. Equivalent Michaelis-Menten parameters

Results presented in Section 3.4.3 show that the coupling between the local and global coefficients is concentration dependent in the case of Michaelis-Menten kinetics (Figure 3.11). However, a qualitative analysis of the results in Sections 3.4.3 and 3.4.4 demonstrates behavior similar to Michaelis-Menten kinetics in the upscaled equations, too. This suggests that approximations for concentration independent parameters for the upscaled rate expression can be found. In the following we investigate these equivalent parameters for the case of (i) a uniform and (ii) a parabolic velocity field.

Uniform velocity field In case of Michaelis-Menten kinetics and a uniform velocity field Equation (3.25) shows the importance of the ratio η for the behavior of the upscaled reaction rate. Although a rigorous analysis revealed that η is

Section 3.4: Results and Discussion

not constant but a function of concentration (Figure 3.11a-d)), we attempt to find a simple constant approximation of η which we call η_{eqv} . To estimate η_{eqv} we fitted Equation (3.25) to the exact one-dimensional concentration profiles derived from the two-dimensional solutions.

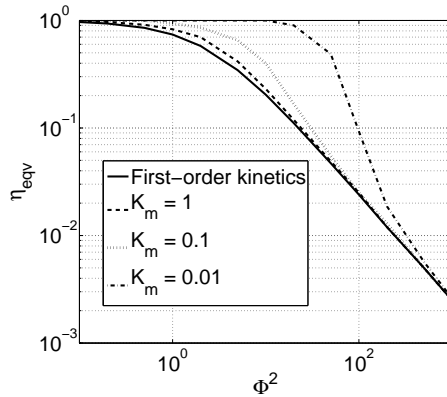


Figure 3.14.: Dependency of the approximated equivalent scaling parameter η_{eqv} on Φ^2 in case of Michaelis-Menten kinetics with uniform velocity field.

The results of the fitting procedure reveal that η_{eqv} depends on Φ^2 and K_m (Figure 3.14). For higher K_m results for Michaelis-Menten kinetics are comparable to those obtained for first-order kinetics. Both reaction kinetics show a similar decrease of η_{eqv} with increasing Φ^2 . This indicates a transient shift in the regime from reaction-limited ($\eta_{\text{eqv}} \approx 1$) to diffusion-limited ($\eta_{\text{eqv}} \ll 1$). In turn, for lower K_m results for Michaelis-Menten kinetics differ, with the reaction-limited regime apparently prevailing longer with increasing Φ^2 . This leads to higher values for η_{eqv} compared to those obtained for first-order kinetics. At sufficiently high Φ^2 results for Michaelis-Menten and first-order kinetics again converge asymptotically to values of $\eta_{\text{eqv}} \approx \pi^2/(4\Phi^2)$ supporting the

statements made in Section 3.4.2. The accuracy of the estimated concentration profiles obtained using η_{eqv} is given by the differences between fitted and exact solutions (Figure 3.15). In general, a good accuracy (errors $\leq 1\%$) is only found in the extreme cases of either low or high values of Φ^2 . The much higher errors found in the transition regime (errors $> 10\%$) correspond to the values of Φ^2 where η exhibits the strongest dependency on C (Figure 3.11). Furthermore, it was noticed that errors increase with decreasing K_m (results not shown).

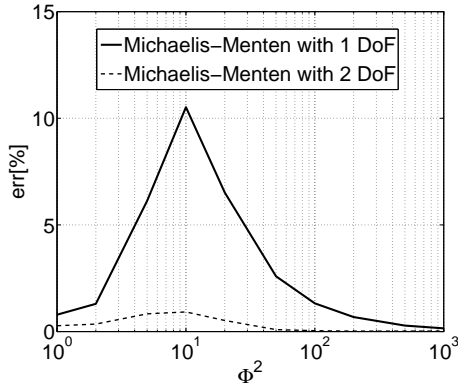


Figure 3.15.: Residual error made by using η_{eqv} (solid line) compared to two (dashed line) degrees of freedom (DoF) for Michaelis-Menten kinetics. Results were obtained assuming a value of $K_m = 0.1$.

To improve the quality of the estimates obtained by fitting effective Michaelis-Menten kinetics to the exact solutions we introduced an additional degree of freedom and fitted Equation (3.26). Considering now both parameters, Φ^2 and K_m , to be independent of each other the improvement resulted in two new equivalent parameters, Φ_{eqv}^2 and $K_{m,\text{eqv}}$. This procedure gives us significantly smaller errors in the transition zone between reaction- and diffusion-limited regimes (Figure 3.15), e.g. for $K_m = 0.1$ errors remain below 1 – 2%. In all

Section 3.4: Results and Discussion

investigated cases, i.e. $0.01 \leq K_m \leq 100$, the error of the improved fitting procedure was always less than 3%, which is in the lower range of the experimental accuracy for concentration measurements indicating the applicability of the approach.

Parabolic velocity field As explained in Section 3.4.4 the scaling behavior in this case can qualitatively be seen as a superposition of the cases described in Sections 3.4.3 and 3.4.2. The calculation of the coefficient functions in Equation (3.28) shows the appearance of complex mixing terms prohibiting the derivation of the parameter for the effective equation. Thus, numerical solutions were used as a reference to obtain constant rate parameters applying again a fitting procedure using Equation (3.28) but with constant coefficients. The effective transport and reaction expressions result in four unknown parameters in this case. However, to avoid overparametrization we consider the transport parameters determined for first-order kinetics to be applicable for Michaelis-Menten kinetics, and fit only Φ_{eqv}^2 and $K_{m,\text{eqv}}$, the two parameters of the reaction term.

For $K_m \geq 1$ the behavior of Φ_{eqv}^2 with respect to Φ^2 is similar to the results of first-order kinetics (Figure 3.16, see also Figure 3.7). In contrast, for $K_m < 1$ significant differences can be observed. In the latter case, the linear dependency between Φ_{eqv}^2 and Φ^2 proceeds till larger values. This shows that the reaction-limited regime is extended towards higher values of Φ^2 , which corresponds to the behavior of η_{eqv} (Figure 3.14). Nevertheless for high values of Φ^2 , Φ_{eqv}^2 converges towards $\pi^2/4$ regardless of the value of K_m . The dependency of $K_{m,\text{eqv}}$ on Φ^2 supports these statements (Figure 3.16b). In the reaction-limited regime, i.e. for low values of Φ^2 , the local and the global Michaelis constants are approximately identical, i.e. $K_m \approx K_{m,\text{eqv}}$. Again, with increasing Φ^2 the local

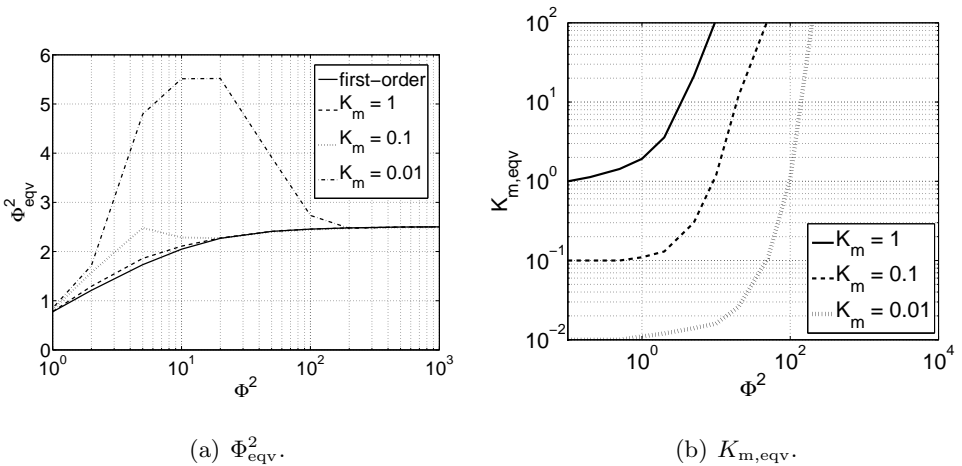


Figure 3.16.: Dependency of the approximated equivalent parameters Φ_{eqv}^2 and $K_{m,\text{eqv}}$ on Φ^2 for several K_m in case of Michaelis-Menten kinetics with a parabolic velocity field.

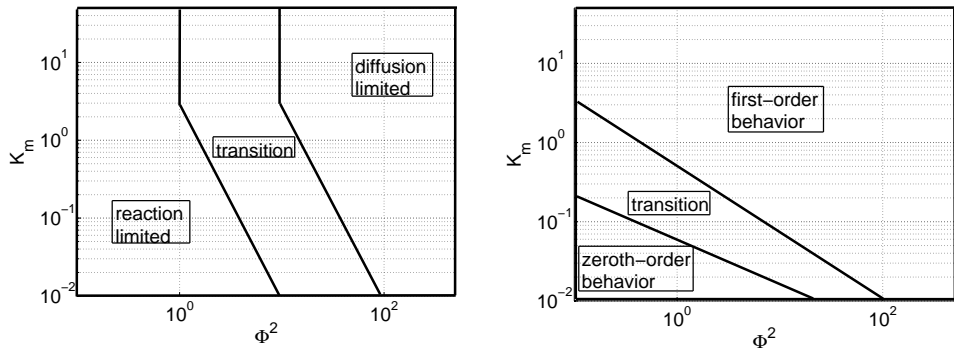
and global behavior diverge with higher values of K_m showing earlier divergence. Eventually, for high values of Φ^2 all global Michaelis constants $K_{m,\text{eqv}}$ increase to high values (100 or above). For such values the global behavior is always well approximated by first-order kinetics regardless of the value of K_m at the local level.

The concentration independent parameters and their dependency on local reaction rate parameters determined by this procedure could be used for macro-scale simulations, e.g. in the form of look-up tables, in pore network models of porous media [Thullner et al., 2007], [Bijeljic et al., 2004], [Li et al., 2006]. Such simulations would allow investigations of further effects, caused for example by variations of the pore width, the tortuosity or pore connectivity of the medium.

3.4.6. Synopsis

In case of Michaelis-Menten kinetics and a uniform velocity field the assumption of a single constant scaling parameter, linking local and global reaction parameters, leads to significant errors for the transition between reaction-limited and diffusion-limited regimes. Specifically, the upscaled rate expression does not follow Michaelis-Menten kinetics. This can explain the problems reported in studies, assuming a single scaling parameter for the reaction rate expression [Wood et al., 2007]. However, the errors obtained by assuming Michaelis-Menten kinetics can be clearly reduced by using two independent scaling relations for Φ^2 and K_m . This results in two new, equivalent parameters Φ_{eqv}^2 and $K_{m,\text{eqv}}$. Though we lack a rigorous analytical derivation of an effective rate expression for a parabolic velocity field, the analysis of the numerical results support the extension of the above statements to parabolic flow fields as well. Consequently, our results can be applied to Michaelis-Menten kinetics with a parabolic velocity field, that enable us to formulate general upscaling rules.

In the case of first-order kinetics the global behavior of the y -averaged solution can be separated into a reaction-limited and a diffusion-limited regime (Figure 3.7) whereby the transition between them is controlled by Φ^2 . In addition, for Michaelis-Menten kinetics we also have to distinguish between a first-order and a zeroth-order regime, the transition of which is now controlled by Φ^2 and K_m . Furthermore, K_m also has an impact on the transition between reaction-limited and diffusion-limited regimes (Figures 3.16). As a result the ratio between K_m and the concentration C has a strong influence on the scaling behavior of Michaelis-Menten kinetics making it far more complex as for first-order kinetics. Such concentration dependent transitions between reaction- and diffusion-limited systems have been reported before [Thullner et al., 2008],



- (a) Dominating local process (diffusion- or reaction-limited). (b) Behavior of the upscaled equations (zeroth- or first-order).

Figure 3.17.: General survey of the upscaling behavior in case of Michaelis-Menten kinetics. Borders of the zones with different regimes are drawn for demonstration purposes using arbitrary threshold values.

[Kampara et al., 2008]. This further supports that scaling rules obtained for first-order kinetics can not easily be expanded to Michaelis-Menten kinetics. Only for $C \ll K_m$, or in the marginal cases of either high or low Φ^2 , the different reaction rates scale similarly.

3.5. Summary and Conclusion

We have presented a new upscaling approach from a two-dimensional system with transport and surface catalyzed degradation of a single reactive species in a simple pore geometry to an effective one-dimensional reactive transport equation. For the analysis we neglected the longitudinal diffusion and motivated the decision in mathematical and physical terms. The validity of the developed model was tested with results from analytical and numerical solutions to verify the soundness of the upscaling process and to evaluate the effective parameters of the upscaled equation.

The main focus was the scaling behavior of Michaelis-Menten kinetics. Two cases have been considered regarding the velocity profile within the pore: a simple uniform and a more realistic parabolic velocity distribution. For both distributions, the results for Michaelis-Menten kinetics have been compared with results obtained for first-order kinetics.

The first two investigated scenarios of the analysis were simple cases of reactive transport with first-order kinetics at the reactive boundary of the medium (scenario I and II in Figure 3.4). Solutions for the upscaled system are already known [Balakotaiah and Chang, 1995], [Kechagia et al., 2002] and served as a verification of the conceptual approach applied in this study and the resulting effective reaction rates. Results show that the macroscopic reaction rate can be strongly reduced when diffusion is the limiting factor and that effective transport parameters must be considered for a parabolic velocity field.

For Michaelis-Menten kinetics (scenarios III and IV in Figure 3.4) the upscaling results showed a concentration dependent coupling between local and global scales with highest sensitivities for local concentrations in the same order of

magnitude as the Michaelis constant (i.e. $K_m \approx c_{\text{bio}}$). For scenario III where K_m was either much higher or much smaller than the bioavailable concentration c_{bio} , the upscaled reaction rate could be well approximated by first-order or zeroth-order kinetics, respectively. Coupling of local and global behaviors using a single parameter demonstrated that scaling parameters either required concentration dependend scaling or resulted in significant errors when remaining constant. The use of this parameter is therefore either cumbersome or inaccurate. However, by using two independent, constant scaling parameters the global behavior could be reproduced reasonably well. Such independent scaling parameters could be derived for both types of velocity fields by fitting the effective one-dimensional profiles to explicit solutions of the two-dimensional problem. For scenario IV our study revealed that the upscaling in case of a parabolic velocity field is analytically as well as numerically cumbersome, thus limiting the applicability of the analytical upscaling approach. However, by using the effective transport parameters obtained for first-order kinetics and re-determining the upscaled reaction rate parameters through fitting the numerical results, we could achieve acceptable results. These upscaled parameters, determined by fitting, now represent a good tradeoff between accuracy and applicability.

Results of this work provide an effective upscaled reaction rate considering mass-transfer limitations taking place at the scale of a single pore. The use of a simplified representation of a pore allowed an analytical treatment and understanding of the physical processes involved. By considering Michaelis-Menten kinetics at the pore scale, the obtained effective equations comprise the restrictions of substrate bioavailability caused by pore-scale diffusion. For such processes the obtained scaling behavior depends on the substrate concentra-

Section 3.5: Summary and Conclusion

tion. This result is caused by the concentration dependent transition between reaction-limited and diffusion-limited regimes and is not observed for first-order kinetics. The approach presented in this study allows the determination of concentration independent scaling parameters, which provide global concentration estimates of an acceptable accuracy. The obtained relations between local and global reaction rate parameters can be transferred to larger scale models, e.g. by using them in pore network simulations. Future steps should include the experimental validation of these theoretical results.

4. A Linear Exchange Model for the description of bioavailability at the pore scale.

Abstract Reactive-transport simulations are a common approach for the quantitative assessment of contaminant biodegradation in the subsurface. To use knowledge on microbial kinetics for the simulation of *in situ* biodegradation the mass-transfer processes controlling the bioavailability of the contaminants need to be described appropriately. A common approach to account for this problem is using a linear exchange model controlling the link between bulk and bioavailable concentration. Assuming that the subsequent degradation is controlled by the bioavailable concentration, only, these two steps can be combined to an analytical expression for the overall reaction rate known as Best-Equation or Best kinetics. In this chapter we evaluate this approach for its ability to describe biodegradation kinetics limited by pore-scale mass transfer. Results from explicit numerical and analytical simulations of both processes at the pore scale are used to test the accuracy of results obtained using Best kinetics. Our analysis shows that strictly spoken the Best-Equation is not valid. However, a good approximation can be achieved with errors of less than 6% in cases of moderate bioavailability and much lower errors in cases of either low or high

bioavailability. These results support the description of mass-transfer processes used in many reactive-transport models. Furthermore, we present a method to obtain an accurate estimate of the unknown rate parameter controlling the diffusive mass transfer processes at the pore scale.

4.1. Introduction

In the last years, *in situ* bioremediation has become a common remediation strategy for sites contaminated by organic carbon species [Alvarez and Illman, 2005]. It is obvious that the effectiveness of such an approach is mainly dependent on the ability of groundwater microorganisms to metabolize the respective contaminant. Measured degradation rates in the field however, have been shown to be often much lower than under idealized laboratory conditions [Simoni et al., 2001], [Alexander, 2000]. This observed discrepancy has lead to the concept of bioavailability, i.e. the contaminant may not be fully available to be degraded by the microorganisms. No single definition of bioavailability exists [Ehlers and Luthy, 2003], [Semple et al., 2004]. Due to the complex structure of the subsurface and the variety of processes controlling the fate of reactive species, factors influencing the bioavailability range from the physical and chemical state of the species to mass-transfer limitations taking place at different scales or across the cell membrane [Barry et al., 2002], [Button, 1991], [Johnsen et al., 2005], [Thullner et al., 2007].

In this study we focus on pore-scale mass fluxes. The relevance of these processes for biodegradation is still under discussion, while some have argued in favor [Gramling et al., 2002], [Raje and Kapoor, 2000], [Meile and Tuncay, 2006] and some against it [Li et al., 2007]. Nonetheless, different concepts have been proposed to account for these pore-scale mass fluxes. Many of these studies assume that macroscopic degradation kinetics follow the same type of rate law as at the pore scale. Commonly these models use a first-order reaction rate [Balakotaiah and Chang, 1995], [Dykaar and Kitanidis, 1996], [Kechagia et al., 2002] but recently more advanced studies with Monod resp. Michaelis-Menten kinetics have been presented [Meile and Tuncay, 2006], [Wood et al., 2007],

[Heße et al., 2009]. However, these models showed problems, when trying to give a rigorous mathematical justification for the effective parameters. As an alternative, approaches relying on a two-step scheme for the pore-scale mass transfer have been shown to describe bioavailability at the pore scale with good accuracy [Bosma et al., 1997], [Kampara et al., 2008]. In these models a distinct separation between the macroscopically measured or bulk concentration and the microscopically bioavailable concentration is assumed. Since only the latter is subject to biodegradation, microbial degradation activity is linked to the bioavailable concentration by Monod resp. Michaelis-Menten kinetics. The mass flux between these two concentrations is described by a linear exchange term. Under steady state conditions it can be combined with the reaction kinetics into a single analytical expression for the macroscopic reactive flux. This expression is known as Best kinetics [Best, 1955]. An intrinsic problem when using a linear exchange term is the assumption of the mass exchange taking place between two distinct compartments or reservoirs of the subsurface (e.g., pore water with bulk concentration and a biophase with bioavailable concentration). A clear separation of both however, is not possible for porous media with laminar flow fields.

In this work we use a simple representation of a single pore to simulate transport and biodegradation of a chemical species at the pore scale. The degradation reaction at the surface of the pore is assumed to follow Michaelis-Menten kinetics. A subsequent averaging over the pore will yield an effective description of the degradation process. These averaged results will serve as references for descriptions of the macroscopic degradation rate using Best kinetics. With this approach we aim to verify (i) whether the effective reaction kinetics can be described by Best kinetics and thus whether the linear exchange model pro-

Section 4.1: Introduction

vides an adequate description of pore-scale mass transfer processes, (ii) how the mass-transfer coefficient to be used in the linear exchange model can be estimated for a given scenario, (iii) how the accuracy and applicability of this method is compared to macroscopic Michaelis-Menten kinetics and (iv) under which circumstances pore-scale mass fluxes must be considered.

The results from this study will therefore assess the applicability of the linear exchange model for the quantitative description of pore-scale mass transfer limitations on bioavailability.

4.2. Theory

4.2.1. Biodegradation at the pore scale

In this study it is assumed that in porous media microorganisms are bound to the surface of the solid matrix and thus biodegradation of dissolved chemical species can only take place at the interface between the fluid phase carrying the dissolved species and the solid matrix phase of the medium. In contrast to the continuum approach used to describe processes at the macro scale, pore-scale descriptions allow for a clear separation between the fluid and the solid phase. Assuming that microorganisms are homogeneously covering the fluid-solid interface at no growth conditions the fate of biodegradable species is given by the pore-scale solution of the advection-diffusion-reaction equation:

$$\frac{\partial c}{\partial t} = -\nabla \cdot (\mathbf{v}c) + D\Delta c + R. \quad (4.1)$$

Here \mathbf{v} describes the water flow velocity and c the species concentration, both subject to pore-scale variations. D is the molecular diffusion coefficient. The reaction rate R describes the biodegradation taking place at the fluid-solid interface, only:

$$R = \begin{cases} 0 & \text{in the fluid phase} \\ -a_v q_{\max} \frac{c}{K_m + c} & \text{at the fluid solid interface.} \end{cases} \quad (4.2)$$

Here q_{\max} is the maximum surface reaction capacity (given in mass per surface area and time, determined by the density and degradation capability of the microorganisms covering the surface), a_v is the specific reactive surface and

Section 4.2: Theory

K_m is the Michaelis constant. This allows to express the maximum reaction rate as

$$k_{\max} = a_v q_{\max}. \quad (4.3)$$

Note that under the constraint of a homogeneous steady-state biomass coverage of the surface the Michaelis-Menten kinetics given by Equation (4.2) is structurally identical to the Monod expression.

4.2.2. Pore-scale geometry

The domain used for the calculations is a semi-infinite two-dimensional channel with diameter $2L_y$ and the fluid-solid interface presented by the (reactive) wall of the channel (see Figure 4.1 top and Figure B.1 for more details). For a realistic porous medium this domain could be applied in a network model consisting of capillary tubes [Kim and Fogler, 2000], [Thullner et al., 2002b]. Although the features of interest for this study are comprised in the used domain, effects like tortuosity, pore connectivity and a modulated pore diameter are not considered here. However, simplified pore geometries like the one used herein have been shown to yield insight into the dependency of geometry, transport and reaction in general [Kitanidis, 1992] as well as reactive transport at the pore scale [Kechagia et al., 2002], [Mikelić et al., 2006], [van Duijn et al., 2008].

4.2.3. Mass transfer described by a linear exchange term

As an alternative to calculating biodegradation rates by solving Equations (4.1) and (4.2) explicitly at the pore scale, introducing a linear exchange term allows for a simplification of the problem. The general concept is to distinguish be-

tween two individual concentrations (representing two individual reservoirs):
 (i) the bulk concentration C (interpreted as the weighted average of the concentration along the width of the pore) which is affected by transport, and
 (ii) the bioavailable concentration c_{bio} (interpreted as the concentration at the pore wall) which determines the rate of biodegradation. Both concentrations are coupled using a linear exchange term R_{tr} to describe the mass exchange rate

$$R_{\text{tr}} = a_v j_{\text{tr}} (C - c_{\text{bio}}). \quad (4.4)$$

Here j_{tr} is the mass-flux coefficient allowing to define the mass-transfer rate coefficient k_{tr} as

$$k_{\text{tr}} = a_v j_{\text{tr}}. \quad (4.5)$$

This approach is also known as the linear driving force model first proposed by Glueckauf and Coates [1947] for adsorption chromatography [Villermaux, 1987], which has been used from then on in the field of reactive transport, too [Roberts et al., 1987], [Harvey and Gorelick, 1995]. Since in a channel geometry this mass exchange takes place in a direction transversal to the water flow and is driven by diffusion one might anticipate that

$$k_{\text{tr}} \propto \frac{D}{L_y}. \quad (4.6)$$

Despite its simplicity the predictive capacity of the approach given by Equation (4.4) is limited due to the difficulties when trying to establish a connection between k_{tr} and real physical features of the porous medium (see e.g. Dykaar

Section 4.2: Theory

and Kitanidis [1996] for a detailed discussion). Therefore, we cannot infer further properties of this parameter at this point of the study.

Using Equation (4.4), Equations (4.1) and (4.2) can be rewritten as:

$$\frac{\partial C}{\partial t} = -V_{\text{eff}} \nabla C + D_{\text{eff}} \Delta C - R_{\text{tr}} \quad (4.7)$$

and

$$\frac{\partial c_{\text{bio}}}{\partial t} = R_{\text{tr}} - k_{\max} \frac{c_{\text{bio}}}{K_{\text{m}} + c_{\text{bio}}} \quad (4.8)$$

with D_{eff} as effective diffusion coefficient and V_{eff} as effective transport velocity along the length of the pore channel. For the calculation of these quantities we refer to Balakotaiah and Chang [1995] and Heße et al. [2009]. Note that V_{eff} is equal to the average pore velocity V for high bioavailability and increases by a maximum factor of approximately 1.4 for very low bioavailability [Heße et al., 2009]. Relaxation times at the pore scale can be considered short compared to macro-scale fluctuations of flow velocities and species concentrations, which justifies the assumption of steady state conditions. Using this assumption Equations (4.7) and (4.8) can be further simplified to a single equation describing the change of the bulk concentration along the pore channel:

$$\frac{\partial C}{\partial t} = -V_{\text{eff}} \nabla C + D_{\text{eff}} \Delta C - R_{\text{Best}} = 0 \quad (4.9)$$

with

$$R_{\text{Best}} = \frac{k_{\text{tr}}}{2} \left(K_{\text{m}} + C + \frac{k_{\max}}{k_{\text{tr}}} \right) \left(1 - \sqrt{1 - \frac{4 \frac{C}{K_{\text{m}}} \frac{k_{\max}}{K_{\text{m}} k_{\text{tr}}}}{\left(1 + \frac{C}{K_{\text{m}}} + \frac{k_{\max}}{K_{\text{m}} k_{\text{tr}}} \right)^2}} \right). \quad (4.10)$$

The latter is the so-called Best-Equation or Best kinetics [Best, 1955] derived by inserting Equation (4.4) into Equation (4.8) and rearraging under steady state conditions (i.e. $R_{\text{tr}} = R_{\text{Best}}$, $\partial c / \partial t = 0$; see e.g. Simoni et al. [2001] or Bosma et al. [1997] for a more detailed discussion). Note that in Equations (4.8) and (4.10) k_{\max} and k_{tr} are given by Equations (4.3) and (4.5), respectively. The Best-Equation provides a closed expression for the biodegradation rate with respect to the macroscopic or bulk concentration C . This macroscopic reaction rate is the result of two consecutive microscopic processes: the diffusive mass transfer and a local reactive consumption (the consumption at the microscopic location of the microorganisms, i.e. the solid water interface). Depending on the prevalence of these processes the macroscopic rate will be either diffusion- or reaction-limited, or a combination of both.

4.2.4. Dimensionless description

In order to obtain generalizable results and to make use of mathematical concepts derived previously by Heße et al. [2009] the above variables and equations are transferred into dimensionless descriptions. For this purpose reference lengths, $L_{x,\text{ref}}$ and $L_{y,\text{ref}}$ as well as a reference concentration c_{ref} are used. For $L_{y,\text{ref}}$ we choose half the width of the pore (see Figure B.1) and $L_{x,\text{ref}}$ is a characteristic length scale of the contaminant along flow paths, which is certainly much longer than $L_{y,\text{ref}}$. As c_{ref} the concentration at the pore inlet is chosen. Using these references allows for the definitions of the Péclet number, and the Thiele modulus, as dimensionless numbers or scaling units. The Péclet number

$$Pe = \frac{VL_{y,\text{ref}}^2}{DL_{x,\text{ref}}} \quad (4.11)$$

Section 4.2: Theory

is a measure for the relevance of advective versus diffusive mass fluxes. The Thiele modulus [Thiele, 1939] is defined as

$$\Phi^2 = \frac{k_{\max} L_{y,\text{ref}}}{a_v D K_m} \quad (4.12)$$

and is a measure to assess whether the macroscopic reaction rate is controlled by the local reaction rate or by diffusive fluxes.

Applying these above reference values allows to transfer all system variables into a dimensionless form

$$\hat{c}, \hat{K}_m = \frac{c, K_m}{c_{\text{ref}}}, \hat{q}_{\max} = q_{\max} \frac{L_{y,\text{ref}}}{D c_{\text{ref}}}, \hat{j}_{\text{tr}} = j_{\text{tr}} \frac{L_{y,\text{ref}}}{D}, \hat{x} = \frac{x}{L_{x,\text{ref}}}, \text{ and } \hat{y} = \frac{y}{L_{y,\text{ref}}}. \quad (4.13)$$

Description of the full problem By assuming the constraint $L_{y,\text{ref}}^2 \ll L_{x,\text{ref}}^2$, justified above, we can neglect the longitudinal diffusion [Heße et al., 2009], [Mikelić et al., 2006], [van Duijn et al., 2008]. Furthermore, we can state that the velocity field has only a component in the direction of the flow path (see Figure B.1). Using this assumption and the definitions above, Equations (4.1) and (4.2) can be converted into the following dimensionless steady-state expressions for the investigated pore channel

$$Pe \left(1 - \frac{y^2}{L_y}\right) \frac{\partial}{\partial \hat{x}} \hat{c} = \frac{\partial^2}{\partial \hat{y}^2} \hat{c} \quad (4.14)$$

in the fluid phase, and

$$\nabla \hat{c} \cdot \mathbf{n} = -\Phi^2 \frac{\hat{c}}{1 + \hat{c}/\hat{K}_m} \quad (4.15)$$

at the fluid solid interface. The velocity distribution in Equation (4.14) is defined as a parabolic function and \mathbf{n} is the outer unit normal.

Note that, unless stated otherwise we will use only dimensionless variables in the remainder of the manuscript. For the sake of simplicity we will thus drop the hat above the symbols.

Effective problem description Applying the above dimensionless variables to Equations (4.9) and (4.10) also allows expressing the effective solution for the pore-space geometry in dimensionless form:

$$\frac{V_{\text{eff}}}{V} \frac{\partial}{\partial x} C - \frac{D_{\text{eff}}}{D} \frac{\partial^2}{\partial x^2} C = a_v \frac{Q}{Pe}. \quad (4.16)$$

with Q as the dimensionless form of Best kinetics:

$$Q = \frac{j_{\text{tr}} K_m}{2} \left(1 + \frac{C}{K_m} + \frac{\Phi^2}{j_{\text{tr}}} \right) \left(1 - \sqrt{1 - \frac{4 \frac{C}{K_m} \frac{\Phi^2}{j_{\text{tr}}}}{\left(1 + \frac{C}{K_m} + \frac{\Phi^2}{j_{\text{tr}}} \right)^2}} \right). \quad (4.17)$$

For the derivation and the calculation of the effective transport parameters in Equation (4.16) we refer again to Balakotaiah and Chang [1995] or Heße et al. [2009] (valid for $Pe < 10$).

For comparison an alternative expression was considered for Q in Equation (4.16) using effective Michaelis-Menten kinetics in analogy to previous studies [Wood et al., 2007], [Heße et al., 2009] (denominated as Monod kinetics therein):

$$Q = \frac{\Phi_{\text{eff}}^2 C}{1 + C/K_{m,\text{eff}}} \quad (4.18)$$

with the effective reaction parameters Φ_{eff}^2 and $K_{m,\text{eff}}$ being linked to the local values for Φ^2 and K_m either using a single scaling parameter η_{eqv} with $\Phi_{\text{eff}}^2 = \eta_{\text{eqv}}\Phi^2$ and $K_{\text{eff}} = \eta_{\text{eqv}}K_m$ [Wood et al., 2007], [Heße et al., 2009], or using two independent scaling parameters $\eta_{1,\text{eqv}}$ and $\eta_{2,\text{eqv}}$ with $\Phi_{\text{eff}}^2 = \eta_{1,\text{eqv}}\Phi^2$ and $K_{\text{eff}} = \eta_{2,\text{eqv}}K_m$ [Heße et al., 2009].

4.2.5. General approach

To evaluate the applicability of the linear exchange model numerical solutions of the full problem description given by Equations (4.14) and (4.15) are compared to solutions of the effective problem description given by Equation (4.16).

Numerical solutions of the full problem were obtained using a finite element solver (for further details see Radu et al. [2008]). A parabolic profile was considered as velocity distribution along the width of the pore channel, and at the inflow of the pore channel a fixed concentration c_0 was used as boundary condition.

The resulting two-dimensional concentration distribution is subsequently averaged over the transversal axis to obtain a one-dimensional concentration profile along the longitudinal flow path. This concentration profile was used as reference for the results of the effective problem descriptions. Due to physically unrealistic boundary conditions at the inlet we avoided artefacts by excluding regions close to the inlet from the fitting procedure. In order to make all following analysis compareable we chose as criteria the point, where the cross section of the concentration distribution is well approximated by a single cosine function (see also Balakotaiah and Chang [1995], Kechagia et al. [2002] or Heße et al. [2009] for further details). Solutions of the effective problem were obtained

applying a Runge-Kutta solver. Values for the unknown mass-flux coefficient j_{tr} in Equation (4.17) and the scaling factor(s) $\eta_{*,\text{eqv}}$ in Equation (4.18) were determined by fitting, i.e. minimizing the square sum error between the analytically derived one-dimensional concentration profile (Best kinetics) and the one obtained by numerical simulation. Furthermore, values for j_{tr} were estimated analytically making use of results from Heße et al. [2009] (see Appendix B.1).

4.3. Results and Discussion

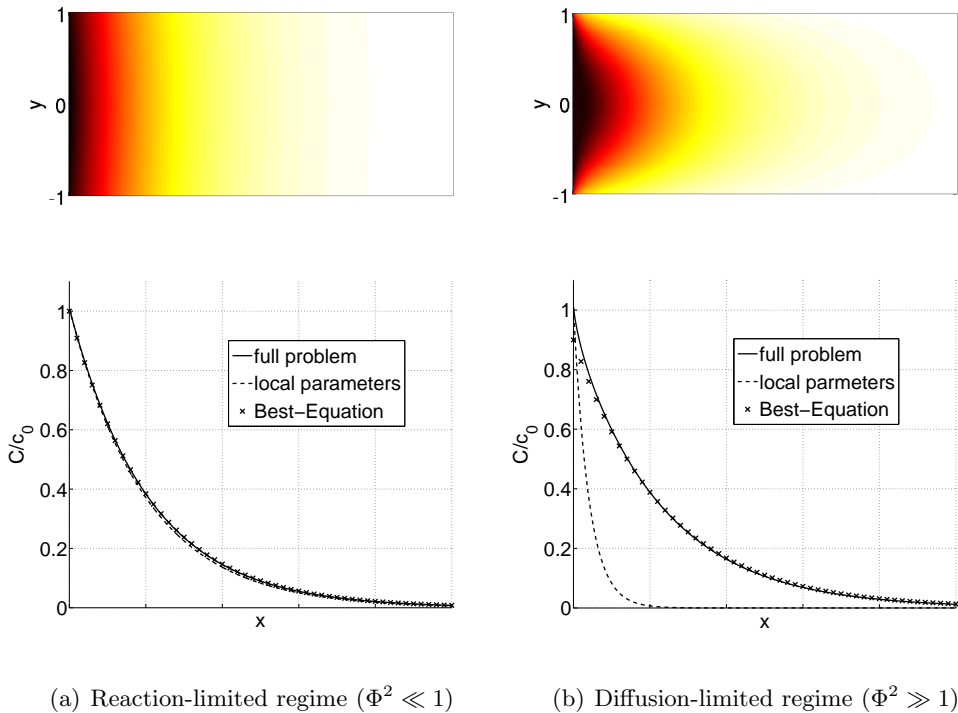


Figure 4.1.: Top: Selected examples showing simulated concentration distributions for the full problem for two different scenarios. Bottom: Comparison of averaged numerical simulations (—) of the full problem to solutions of Equation (4.16) using Best kinetics with a fitted j_{tr} (\times) and using Michaelis-Menten kinetics with local reaction rate parameters (- - -).

To demonstrate the general approach and to indicate the relevance of using an appropriate effective description results are first shown for two arbitrary examples; one representing a reaction-limited regime (Figure 4.1a), where the macroscopic degradation rate is mainly controlled by the local reaction rate,

and one representing a diffusion-limited regime (Figure 4.1b) where mainly transversal diffusive fluxes are controlling the macroscopic degradation rate. Numerical simulation results (steady state) of the full problem show that for the reaction-limited regime concentration gradients along the width of the pore channel are rather smooth (Figure 4.1a top). This results in the average bulk concentration C being representative for the concentration at the pore wall c_{bio} . As a consequence, the bulk concentration profile along the length of the pore obtained by averaging the numerical results along the width of the pore channel can be reasonably well predicted using an effective description with Michaelis-Menten kinetics and the local parameters (i.e. using Equation (4.16) with Q as in Equation (4.18) and $\eta_{1,\text{eqv}} = \eta_{2,\text{eqv}} = 1$) (Figure 4.1a bottom). In contrast, for the diffusion-limited regime strong concentration gradients can be observed along the width of the pore, and the bulk concentration C differs from the concentration at the pore wall c_{bio} (Figure 4.1b top). In this case predicting the longitudinal bulk concentration profile using Michaelis-Menten kinetics with local parameters leads to an overestimation of the macroscopic reaction rate and thus to an underestimation of the bulk concentration (Figure 4.1b bottom). For both regimes, using an effective description based on the linear exchange model, i.e. using Best kinetics as effective reaction rate Q in Equation (4.16), allows for a very good reproduction of the longitudinal bulk concentration profile (Figure 4.1 bottom) indicating the general applicability of the approach.

4.3.1. General behavior of the mass-flux coefficient j_{tr}

In order to assess the general behavior and the accuracy of the linear exchange model the above comparison of results from numerical simulations of

Section 4.3: Results and Discussion

the full problem and from the effective solution using Best kinetics was performed for a broad range of possible scenarios characterized by different values of the Thiele modulus Φ^2 and the ratio between the maximum concentration and the Michaelis constant c_0/K_m . While Φ^2 is a good inverse measure for the relative importance of reactive vs. diffusive processes the ratio c_0/K_m indicates if the reaction rate is (initially) following (i) an effective zeroth-order regime ($c_0/K_m \gg 1$), (ii) an effective first-order regime ($c_0/K_m \ll 1$), or (iii) a transition between both ($c_0/K_m \approx 1$).

Optimum fit results obtained for j_{tr} show a dependency of this parameter on the local reaction rate parameters (i.e., Φ^2 and c_0/K_m) (Figure 4.2a). With respect to Φ^2 different regimes can be identified: for low values of Φ^2 j_{tr} shows a strong dependency on c_0/K_m with higher values of c_0/K_m associated with higher values of j_{tr} resulting in a variation of j_{tr} over several orders of magnitude (Figure 4.2a, left part), which have been reported before by Young and Ball [1995] for similar setups. In contrast, for sufficiently high values of Φ^2 optimum fit values approach a constant value of $j_{tr} \approx 2.4 - 2.5$ independent of c_0/K_m (Figure 4.2a right part). The transition between these two extremes is characterized by j_{tr} increasing with Φ^2 towards a maximum value before decreasing towards the constant value for large Φ^2 . The larger c_0/K_m the larger the value of Φ^2 at which maximum values of j_{tr} are reached and at which subsequently the constant value is approached.

The residual errors obtained when comparing one-dimensional concentration profiles determined by fitting j_{tr} to solutions of the full problem show that for both, very high or very low values of Φ^2 , Best kinetics provides a very good estimate of the concentration along a pore-scale flow path with neglectable errors (Figure 4.2b). For values of $\Phi^2 \approx 10^0 - 10^2$ larger errors can be observed,

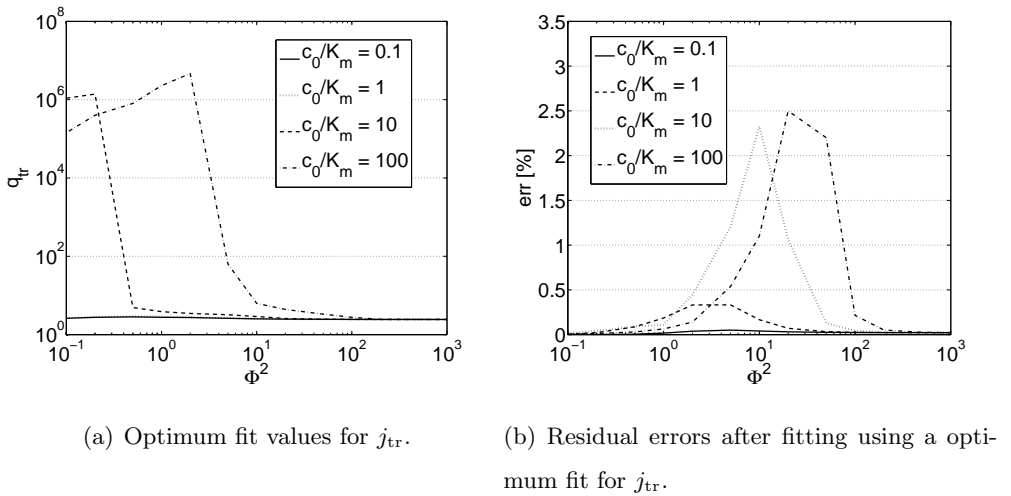


Figure 4.2.: Behavior and accuracy of the mass-flux coefficient j_{tr} from Equation (4.17) with respect to Φ^2 . The value of j_{tr} was determined by fitting an effective solution using Equation (4.16) to averaged numerical solutions of the full problem for several Φ^2 and c_0/K_m (a,b).

the value of which depend on c_0/K_m . For high values of c_0/K_m errors of up to 2.5% can be found, with decreasing maximum values with decreasing c_0/K_m . Also values of Φ^2 at which highest errors were found depend on c_0/K_m with higher c_0/K_m shifting the peak of the residual error towards higher values of Φ^2 .

Given that a value of $c_0/K_m = 0.1$ represents the first-order range of Michaelis-Menten kinetics, Best kinetics appears to be most accurate for this type of reaction regime. However, as maximum errors remain below 3% for all combinations of c_0/K_m and Φ^2 Best kinetics provides a good effective description also for the zeroth-order range of Michaelis-Menten kinetics and the transition be-

Section 4.3: Results and Discussion

tween these extremes. This indicates that in general the linear exchange model is an adequate effective description of bioavailability limited biodegradation at the pore scale. However, for low Φ^2 values of j_{tr} obtained by fitting varied over several orders of magnitude depending on both, Φ^2 and c_0/K_m . This would certainly challenge the prediction of j_{tr} and the applicability of the linear exchange model for practical use.

4.3.2. Using a constant estimate for j_{tr}

As discussed in the above section, j_{tr} showed strong variations with respect to the parameters of the local reaction rate, i.e. Φ^2 and c_0/K_m (Figure 4.2a). For high values of Φ^2 and/or low values of c_0/K_m however, the mass-flux coefficient j_{tr} appeared to be relatively constant. In addition, sensitivity analysis showed that for high c_0/K_m , results are rather insensitive even to large variations of j_{tr} (data not shown). These observations are consistent with the fact that for high c_0/K_m a zeroth-order reaction regime is prevailing with the reaction rate hardly depending on concentration. Thus, j_{tr} controlling the link between bulk and bioavailable concentration is not supposed to have a major impact on the overall reaction rate, which explains the low sensitivity. In contrast, for low c_0/K_m representing a first-order reaction regime the concentration is considered to be a crucial factor for the overall degradation rate and consequently the sensitivity towards j_{tr} is higher. As a consequence, any value for j_{tr} which might be used to represent the entire range of Φ^2 and c_0/K_m values should be at first a good estimate for the first-order regime.

A re-analysis of the results from Heße et al. [2009] allows for low values of c_0/K_m to derive an analytical estimate of

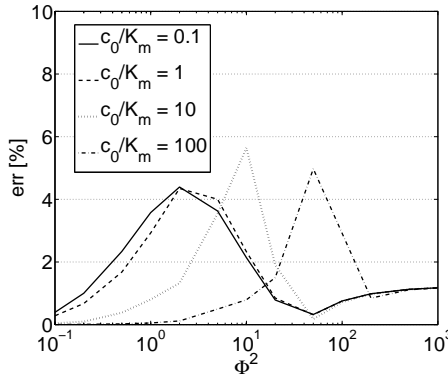


Figure 4.3.: Residual errors made when using Best kinetics with a constant mass-flux coefficient $j_{\text{tr}} = \pi^2/4$ as effective reaction rate expression for several Φ^2 and c_0/K_m .

$$j_{\text{tr}} = \pi^2/4 \approx 2.47 \quad (4.19)$$

(see Appendix B.1). This value is identical to results of Haggerty and Gorelick [1995] reported for the case of layered diffusion, and is also nearly identical to the optimum fit values found for large Φ^2 . In order to assess the applicability of this constant estimate for the entire range of Φ^2 and c_0/K_m an error analysis was done in analogy to the above section (Figure 4.2b).

Results of this error analysis for a constant value of $j_{\text{tr}} = \pi^2/4$ show again a good accuracy with small errors in the cases of either low or high values of Φ^2 (Figure 4.3). Higher errors are again observed in the transition regime with values showing a dependency on Φ^2 and c_0/K_m comparable to above results. The maximum of this error however, does not exceed 6% regardless of the value of c_0/K_m , which is still in an acceptable range compared to experimental accuracies [European Commission, 2000]. These findings support the extrapolation

Section 4.3: Results and Discussion

of the analytically determined first-order regime value of j_{tr} to the entire range of reaction regimes. Thus, the simplicity of obtaining an estimate while keeping the estimation errors in an acceptable range suggests the analytically derived value of j_{tr} to be the more efficient approach compared to the more accurate fitting procedure.

4.3.3. Comparison with macroscopic Michaelis-Menten kinetics

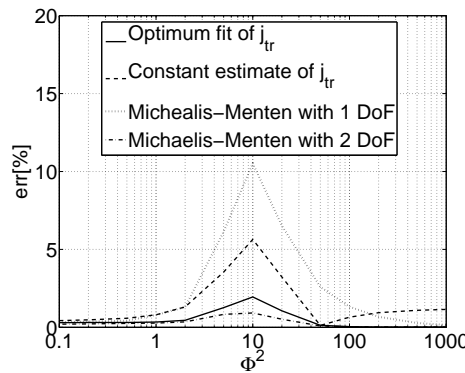


Figure 4.4.: Residual errors made by using different effective rate expression:

Best kinetics with a constant $j_{tr} = \pi^2/4$ (dashed line), and with fitted values for j_{tr} (solid line), and Michaelis-Menten kinetics with one (dotted line) and two (dashed dotted line) degrees of freedom (DoF), i.e. independently fitted scaling parameter(s). Results were obtained assuming a value of $c_0/K_m = 10$.

To compare the accuracy of the linear exchange model with effective Michaelis-Menten kinetics suggested in the literature as effective degradation rates [Wood et al., 2007], [Heße et al., 2009], residual errors of these different approaches were determined assuming $c_0/K_m = 10$ as for this value large errors were found

(see Figure 4.2b and Figure 4.3). Results of this comparison indicate that the highest accuracy is obtained by using effective Michaelis-Menten kinetics with two independent effective parameters (Figure 4.4). This observation can be attributed to the additional degree of freedom in this fitting approach compared to the expressions using a single fitting parameter. Of those approaches using one parameter only, Best kinetics with a fitted j_{tr} is the most accurate. The analytically derived value of $j_{\text{tr}} = \pi^2/4$ leads to slightly less accurate estimates as shown above. Compared to these two estimates using Best kinetics, effective Michaelis-Menten kinetics with only one scaling factor leads to the highest estimation errors.

4.3.4. Relevance of pore-scale bioavailability restrictions

In order to assess the necessity of the application of an effective description for pore-scale mass fluxes one has to evaluate the bioavailability with respect to the local reaction rate parameters Φ^2 and K_m . To quantify bioavailability Bosma et al. [1997] introduced the bioavailability number Bn as the ratio between the mass-transfer rate coefficient k_{tr} and the microbial specific affinity given by k_{max}/K_m . Combining this with Equations (4.5), (4.12) and (4.19) allows to express Bn as

$$Bn = \frac{k_{\text{tr}}}{k_{\text{max}}/K_m} = \frac{\pi^2}{4\Phi^2}. \quad (4.20)$$

This relation supports that the Thiele modulus can serve as a measure for species bioavailability [Chung et al., 1993]. However, as discussed above the relevance of such mass-transfer limitations also depends on the concentration of the reactive species, an effect already reported previously [Kampara et al., 2008],

Section 4.3: Results and Discussion

[Thullner et al., 2008]. For these reasons, Kampara et al. [2008] introduced the effective bioavailability B_{eff} as the ratio between the effective degradation rate given by Best kinetics (Equation 4.17 using the constant estimate for j_{tr}) and the potential degradation rate in the absence of any bioavailability restrictions given by Michaelis-Menten kinetics (Equation 4.18 using local values for Φ^2 and K_m ; see Appendix B.2 for more details). Expressing B_{eff} as function of Φ^2 and C/K_m (Figure 4.5) allows the determination of parameter combinations for which bioavailability effects need to be considered at the pore scale.

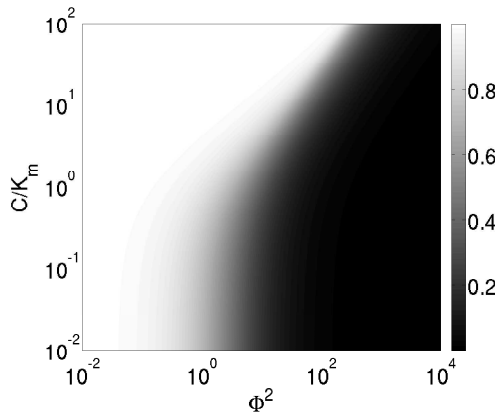


Figure 4.5.: Effective bioavailability B_{eff} with respect to the local reaction rate parameters Φ^2 and C/K_m . The values were calculated as the ratio of the reactive flux given by Best kinetics using Equation (4.17) compared to the reactive flux given by Michaelis-Menten kinetics using Equation (4.18) with local parameters.

Results of this analysis show that for low concentrations ($C/K_m \leq 1$) bioavailability restrictions become relevant at values of $\Phi^2 \approx 1$ with higher Φ^2 resulting in severe bioavailability limitations of the degradation rate (Figure 4.5). For higher concentrations, i.e. ($C/K_m \geq 1$), values of Φ^2 , for which bioavailability

effects have to be expected, increase. As a result a reduced bioavailability is confined to relatively fast reactions (high Φ^2), only. These findings are also in general agreement with the results for surface catalyzed abiotic reactions reported recently by Li et al. [2007] who observed only negligible limitations of mineral dissolution rates at for $\Phi^2 \leq 1$ (estimate based on data given therein).

4.3.5. Comparison to experimental data

In order to illustrate the application of the concept outlined above for the interpretation of experimental data we here use results from a column experiment on the biodegradation of 3-chlorodibenzofuran taken from Harms and Zehnder [1994] as an example. Detailed information on the setup and the experimentally determined parameters are provided in Appendix B.3, where we furthermore show how dimensionless and dimensional parameters are transferred into each other to exemplify the application of our results to real world problems.

For this experimental setup a Thiele modulus $\Phi^2 = 1.6$ and a mass-transfer rate coefficient of $k_{\text{tr}} = 0.23 \text{ s}^{-1}$ were calculated. Measured substrate concentrations decrease from $1.55 \mu M$ at the inlet to $0.37 \mu M$ at the outlet of the column which corresponds to values for C/K_m to vary between 6.7 and 1.6. Referring to the scheme given in Figure 4.5 this corresponds to a scenario with mildly limited bioavailability. According to Heße et al. [2009] these values furthermore yield an effective transport velocity v_{eff} of ≈ 1.2 larger than the average flow velocity V . Using the given parameter values (see Appendix B.3), the column experiment was simulated using the Biogeochemical Reaction Network Simulator (BRNS) [Regnier et al., 2002], [Thullner et al., 2005]. The simulation of biodegradation of the substrate using Michaelis-Menten kinetics with the given local parameters and no correction to the flow velocity resulted in an outflow concentration of

Section 4.3: Results and Discussion

$C_{\text{out}} = 0.048 \mu M$. This is a massive underestimation of the measured outlet concentration of $C_{\text{out}} = 0.37 \mu M$, which indicates a limited bioavailability of the substrate in the column. When using Best kinetics, i.e. Equation (4.10) with the above k_{tr} and given parameter values, the simulated outlet concentration clearly increased to $C_{\text{out}} = 0.185 \mu M$ but still underestimated the measured value. However, when deriving the hydraulic radius not from the specific surface of the glass bead packing ($r_{\text{hyd}} = 0.016 \text{ cm}$, see Appendix B.3), but arbitrarily assuming it to be equal to the (upper range) of the reported glass bead size ($r_{\text{hyd}} = 0.050 \text{ cm}$), the Thiele modulus increases to $\Phi^2 = 4.8$ and the mass-transfer coefficient deceases to $k_{\text{tr}} = 0.073 \text{ s}^{-1}$. With these values an outlet concentration of $c_{\text{out}} = 0.35 \mu M$ was simulated, which is in close agreement to the measured value while the results using the local parameter Michaelis-Menten rate expression were not affected by the change of hydraulic radius. Apparently some limitation of bioavailability can be attributed to the diffusive mass transfer at the pore scale but other factors (e.g., heterogeneities of the flow field, distribution of the bacteria, etc.) may have limited the bioavailability in this experiment as well.

Future research (e.g., comparing porous media packings with different bead sizes) must show if these effects can be confirmed by experimental data.

4.3.6. Implications for practical applications

The pore-scale mass transfer limitations investigated in the present study represent an intrinsic upper limit of mass transfer influenced bioavailabilty to be found in porous media. Any additional mass-transfer limitation at a larger scale would lead to a reduction of the mass-transfer rate coefficient. The need to consider pore-scale mass transfer limitations in practical applications is linked to

the Thiele modulus Φ^2 and the ratio of C/K_m as shown above. The determination of the mass-flux coefficient using a fitting routine requires however, a suitable reference especially with regard to its strong dependency on the parameters of the local reaction kinetics. To avoid this limitation a constant estimate of $j_{tr} = \pi^2/4$ can be used as an alternative with only slightly less accuracy.

Alternative approaches using Michaelis-Menten kinetics as effective degradation rate are also challenged by the effective parameters showing (i) a distinct dependency on the local rate parameters and (ii) a fitting or complex upscaling procedure for their derivation [Wood et al., 2007] [Heße et al., 2009]. Furthermore, an improvement of the accuracy achieved by Best kinetics can only be obtained when using two independently scaling effective parameters. Considering that an experimental determination of organic biodegradable chemicals in the environment is typically done with an error of 10% or more [European Commission, 2000], Best kinetics with a constant value of $j_{tr} = \pi^2/4$ is the most suitable compromise between providing an accurate prediction and the effort needed to determine the relevant effective parameter. Although Best kinetics considers one reactant only more reactive species could be modelled by means of explicit two-step schemes, i.e. an individual transport step for each species according to the linear exchange model with a subsequent combined degradation step. To predict values for the ultimately needed mass-transfer rate coefficient k_{tr} from the constant mass-flux coefficient j_{tr} only knowledge of the porous matrix geometry (hydraulic radius, specific surface) and the diffusion coefficient of the degraded substrate need to be known (see Appendix B.3 for an application example).

5. Influence of biofilm growth and pore-width variations on effective degradation rates.

Abstract In this chapter we investigate the influence of a growing biofilm as well as pore-width variations on effective degradation rates. The relevant processes, i.e. transport and reactive consumption of a reactive species as well as the growth of the microorganisms are modelled spatially resolved at the pore scale. For the representation of the pore space two geometries are considered. A simple channel domain as well as a sinusoid domain. Microorganisms are modelled in form of a thin biofilm at the wall of the pore not affecting fluid flow. Steady state of the system is achieved through balance between growth of the biofilm due incoming diffusional fluxes and the decay rate of the biofilm itself. The results presented herein are produced with the help of numerical simulations using a mixed finite element code as well as additional analytical tools where possible. The results show a reduction of the reactive-transport model to a pure transport model due to the adaption of the biofilm to the incoming diffusional fluxes. A variable pore width furthermore yields higher degradation rates compared to a simple channel geometry the dependency of which is further discussed.

5.1. Introduction

The use of *in situ* bioremediation for the clean up of a contaminated site has attracted increasing attention in the last years due to its low costs and easy processing compared to other methods [Rittmann, 2004]. Bioremediation relies on the ability of microorganisms to degrade hydrocarbon contaminants by using these compounds as a source of carbon as well as energy for growth.

This growth can occur in the porous media in different modes [van Loosdrecht et al., 2000]. The form most commonly assumed is that of a biofilm covering the solid matrix [Rittmann, 1993], [Chen, 1999]. Other forms reported in the literature comprise compact aggregates or web like structures [Dupin et al., 2001b]. The impact of biofilm development on the overall consumption is still a matter of debate, with many authors investigating the effects of biofilm clogging on the permeability of the soil [Suchomel et al., 1998], [Kim and Fogler, 2000], [Thullner et al., 2002a], [Kapellos et al., 2007]. While commonly the biofilm is considered to be formed uniformly some have argued that the biofilm growth leaves only channel like flow paths in the porous medium [Wanner et al., 1995]. While several previous authors have investigated biofilm explicitly at the pore scale [Dykaar and Kitanidis, 1996], [Knutson et al., 2005], to our best knowledge, no investigation exist on the interplay of biofilm growth and effective degradation rates.

In this study we use a modification of the pore-scale reactive transport model developed by Heße et al. [2009]. Instead of a biofilm being constant in space and time, growth according to the incoming flux of the reactive species is explicitly modelled. The biofilm is assumed as a thin layer at the interface of the fluid and solid medium not affecting fluid flow. As representations of the pore space

Section 5.1: Introduction

we use two different two-dimensional geometries. A simple channel geometry as well as a sinusoid geometry comprising more traits of a porous medium. The relevant processes, i.e. transport and consumption of the reactive species as well as growth and decay of the biofilm, are simulated numerically until steady state is achieved. In the case of a channel geometry as well as in the case of a simplified flow field within the sinusoid geometry the numerical results are compared to analytical results. These results comprises expressions for the distribution of the biofilm and for the reactive species.

In the following we will first describe the governing equations and the representation of the pore space as used in this study. After that, we will derive the analytical method applied to the simpler cases described above. Finally, we will present and discuss the numerical results.

5.2. Theory

In this section we present the equations, which describe the transport and consumption of a reactive species as well as the growth of a biofilm. We furthermore introduce the geometrical representation of the pore space. Additionally a scaling analysis is performed in order to introduce the relevant scaling units.

5.2.1. Scale of Interest

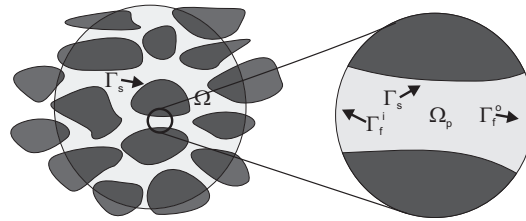


Figure 5.1.: Schematic of the scale of interest.

Unlike to the continuum or Darcy scale (Bear [1972]) the reactive species and the biofilm have to be modelled spatially resolved at the pore scale. The transport of the reactive species takes place in the liquid phase Ω_p (see Figure 5.1). It enters the pore through the inlet Γ_f^i and leaves, if not consumed, at the outlet Γ_f^o . The microorganisms on the other hand are localized at the surface of the solid phase Γ_s , where the degradation of the reactive species takes place.

5.2.2. Governing Equations

The first quantity investigated in this study is the concentration of the reactive species labeled with c , which is subjected to transport and reaction. The system of equations describing these processes will be

$$\frac{\partial}{\partial t}c + V\nabla \cdot \tilde{\mathbf{v}}c = D\Delta c \quad \text{in } \Omega_p, \quad (5.1a)$$

$$D\nabla c_{\text{bio}} \cdot \mathbf{n} = -k_{\text{mo}} c_{\text{mo}} \frac{c_{\text{bio}}}{K_{\text{m}} + c_{\text{bio}}} \quad \text{on } \Gamma_s, \quad (5.1b)$$

$$c = c^0 \quad \text{on } \Gamma_f^i. \quad (5.1c)$$

In Equation (5.1a) the water flux \mathbf{v} is given as $\mathbf{v} = V\tilde{\mathbf{v}}$. Here V is the pore-scale average velocity and $\tilde{\mathbf{v}}$ comprises the deviations from this value. The coefficient D is the molecular diffusion. The reaction rate in Equation (5.1b) has two coefficients: (i) the specific microbial reaction rate k_{mo} and (ii) the Michaelis constant K_{m} . The variable c_{bio} denotes the concentration of the reactive species available to the microorganisms. These microorganisms are the second species investigated in this study, the concentration of which is labeled with c_{mo} . The growth and decay is described by

$$\frac{\partial}{\partial t}c_{\text{mo}} = Yk_{\text{mo}}c_{\text{mo}} \frac{c_{\text{bio}}}{K_{\text{m}} + c_{\text{bio}}} - \mu_{\text{dec}}c_{\text{mo}}. \quad (5.2)$$

Here Y is the yield factor, i.e. the portion of degraded reactive species being transformed into biomass. The second term in Equation (5.2) is a decay term. In this work a first-order relationship with the decay rate μ_{dec} is assumed. Whereas transport of the reactive species takes place in the entire pore space the microorganisms are assumed to form a thin biofilm at the fluid-solid interface not affecting fluid flow.

5.2.3. Channel Domain

The first geometry being used to represent the pore space in this study is a semi-infinite channel domain (Figure 5.2). Despite its simplicity it has been suc-

cessfully applied by different authors to investigate reactive transport [Kechagia et al., 2002], [Mikelić et al., 2006], [Heße et al., 2009] as well as biomass growth and development [Chen et al., 1993], [Dupin et al., 2001a] [Dupin et al., 2001b]. The simplicity of the domain will facilitate the use of analytical tools in the investigation of the reactive-transport processes, which will be outlined in Section 5.3 in more detail.

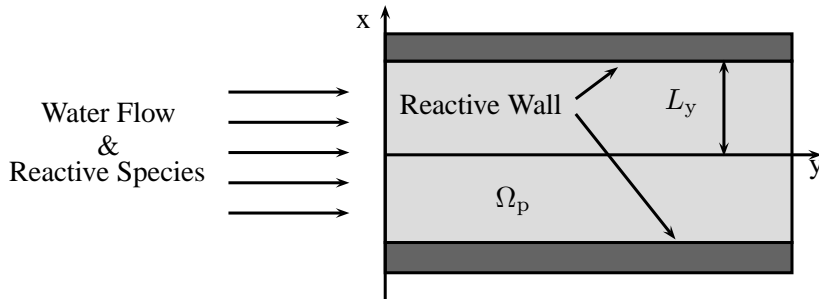


Figure 5.2.: Geometry of a channel geometry.

5.2.4. Sinusoid domain

In addition to the channel domain, a more realistic domain is used for the representation of the pore space (Figure 5.3). This geometry facilitates the investigation of the relevance of realistic features like a varying pore diameter, which leads to different growth conditions in the narrow as well as in the wide part of the pore or a more complex flow field.

The sinusoid domain depicted in Figure 5.3 can be described mathematically by the envelope of the geometry

$$h(x) = (1 + a \sin(2\pi x))L_y. \quad (5.3)$$

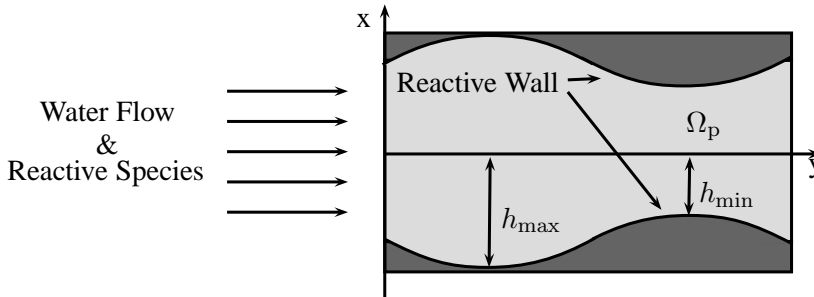


Figure 5.3.: Geometry of a sinusoidal geometry.

Here L_y refers to the length scale defined in Figure 5.2. Using this definition the same average pore volume is obtained as for the channel geometry. The reactive surface per unit volume a_v however, is increased compared to the channel geometry ($a_v = 1$). For a geometry described by Equation (5.3) this quantity is given as

$$a_v = \int_0^{2\pi} \sqrt{1 + a^2 4\pi^2 \cos^2(4\pi x)} dx. \quad (5.4)$$

This value must be taken into account when performing a dimensional analysis of the system.

5.2.5. Scaling analysis

In order to transform the system given by Equations (5.1a) – (5.1c) into a nondimensional or scaled form we introduce the following reference or scaling units: the reference lengths $L_{x,\text{ref}}$ and $L_{y,\text{ref}}$ as well as the reference concentrations c_{ref} and $c_{\text{mo,ref}}$. This procedure allows a generalization of our results and is suited for the numerical treatment of the problem. Applying these reference values yields the following transformations of the system variables

$$\hat{x} = \frac{x}{L_{x,\text{ref}}}, \quad \hat{y} = \frac{y}{L_{y,\text{ref}}}, \quad \hat{c}, \hat{K}_m = \frac{c, K_m}{c_{\text{ref}}}, \quad \hat{\mu}_{\text{dec}} = \frac{\mu_{\text{dec}} L_y^2 c_{\text{mo}}}{D K_m}, \quad \text{and} \quad \hat{c}_{\text{mo}} = \frac{c_{\text{mo}}}{c_{\text{mo,ref}}}. \quad (5.5)$$

In addition we introduce the following two scaling units: First, the Péclet number

$$Pe = \frac{VL_{y,\text{ref}}^2}{DL_{x,\text{ref}}}, \quad (5.6)$$

which is comparing the advective vs. the diffusive flux. Second, the Thiele modulus

$$\Phi^2 = \frac{k_{\text{mo}} c_{\text{mo}} L_{y,\text{ref}}}{a_v D K_m}, \quad (5.7)$$

which is comparing the diffusive vs. the reactive flux. Before rewriting Equations (5.1a) – (5.1c) into the scaled form we introduce two further simplifications. First, since we are only interested in the steady state of the system the time derivative is set to zero. Second, since we can assume the variations in the concentration c to be much smaller in direction of the flow field than in the transversal direction we can assume that $L_{y,\text{ref}}^2 \gg L_{x,\text{ref}}^2$. With this condition we can neglect the longitudinal diffusion. As a result we can rewrite Equations (5.1a) – (5.1c) as:

$$Pe \nabla \cdot \tilde{\mathbf{v}} \hat{c} = \frac{\partial^2}{\partial \hat{y}^2} \hat{c} \quad \text{in } \Omega_p, \quad (5.8a)$$

$$\nabla \hat{c}_{\text{bio}} \cdot \mathbf{n} = - \frac{\Phi^2}{1 + \hat{c}_{\text{bio}} / \hat{K}_m} \hat{c}_{\text{bio}} \quad \text{on } \Gamma_s, \quad (5.8b)$$

$$\hat{c} = \hat{c}^0 \quad \text{on } \Gamma_f^i. \quad (5.8c)$$

Section 5.2: Theory

By making use of the steady state condition Equation (5.2) can be rearranged to

$$\hat{c}_{\text{bio}} = \frac{\hat{K}_m \hat{\mu}_{\text{dec}}}{(Y \hat{k}_{\text{mo}} - \hat{\mu}_{\text{dec}})}. \quad (5.9)$$

Equation (5.9) shows that the bioavailable concentration of the reactive species \hat{c}_{bio} is constant along the reactive wall. The reactive-transport system under consideration here is accordingly reduced into a pure transport system and fully decoupled from the biomass concentration \hat{c}_{mo} . Equation (5.8b) can therefore be replaced with

$$\hat{c} = \hat{c}_{\text{bio}} \text{ on } \Gamma_s, \quad (5.10)$$

where \hat{c}_{bio} is the constant concentration of the reactive species calculated with Equation (5.9). This behavior can be explained by the fact that the distribution of the biomass is evolving until a balance is achieved between growth caused by the incoming diffusive flux of the reactive species and the decay of the microorganisms. The concentration \hat{c}_{bio} is consequently the value, where the existence of these microorganisms can be sustained.

Note that from now on we will, for the sake of convenience, drop the hat for the labeling of the nondimensional units.

5.2.6. Scenarios considered for the calculation

As mentioned above two different geometries are used in this work. For each geometry we will in addition consider two different velocity fields: a simple uniform as well as a realistic velocity field. For the channel geometry the flow

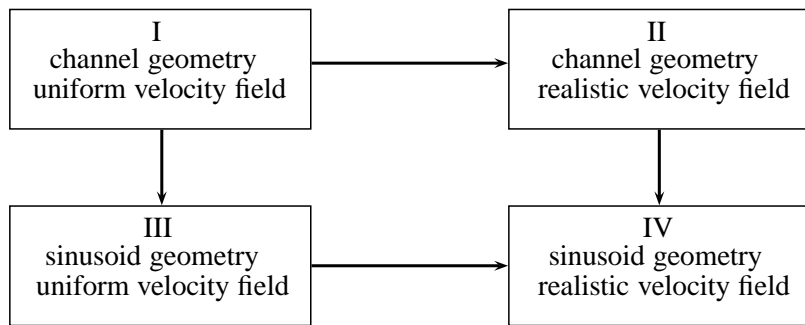


Figure 5.4.: Overview of the different scenarios considered in this study.

of a fluid is known as Hagen-Poiseuille flow and is described by a parabolic velocity field. For the sinusoid domain we here use a derivation of the flow field described by Kitanidis and Dykaar [1997] for this type of geometry. As a result four different scenarios of increasing complexity are investigated (Figure 5.4). This procedure allows an step-by-step understanding of the dynamics in the most complex, and by extension the most realistic, Scenario IV, where no analytical solutions are available.

5.3. Analytical Methods

In this section we will derive the steady state analytical solutions for the system of coupled reactive transport and biofilm growth in a two-dimensional geometry. For the most complex case, i.e. a sinusoid geometry combined with a realistic flow field, no analytical solution can be provided. This case will however, be discussed in detail in Section 5.4 with the help of numerical results.

Assuming the flow field has only a component in the y -direction we can simplify the coefficient function \tilde{v} in Equation (5.8a) to $f(y)$. By furthermore including the condition given by Equation (5.10) we can state

$$Pef(y) \frac{\partial}{\partial x} c = \frac{\partial^2}{\partial y^2} c \quad \text{in } \Omega_p, \quad (5.11a)$$

$$c = c_{\text{bio}} \quad \text{on } \Gamma_s, \quad (5.11b)$$

$$c = c^0 \quad \text{on } \Gamma_f^i. \quad (5.11c)$$

Owing to its symmetry Equation (5.11a) is a separable partial differential equation, i.e. we can write the solution in the following form

$$c(x, y) = \sum_i^\infty c_i^x(x) c_i^y(y). \quad (5.12)$$

Since the pore-scale model used herein is a modified version of the model described by Heße et al. [2009] we will use this study as reference for the solution of Equations (5.11a-c). Compared to this reference some alterations may be noted: First, according to Equation (5.2) the biofilm will sustain growth until limited by the ability of the diffusion to provide enough supplies. This will lead in steady state to a scenario comparable to the diffusion-limited regime

described by Heße et al. [2009]. Second, the constant bioavailable concentration defined in Equation (5.9) acts as a form of offset, i.e. the solution c does not converge to zero for big values of x but to c_{bio} . As a result we will derive the following analysis for $c_{\text{bio}} = 0$ only, since the case $c_{\text{bio}} \neq 0$ is covered by considering the following transformation

$$c(x, y) = c(x, y)(1 - c_{\text{bio}}) + c_{\text{bio}}. \quad (5.13)$$

The last difference concerns the boundary condition c^0 left unspecified above. In their study Heße et al. [2009] used a uniform distribution to describe c^0 . With respect to Equation (5.12) c^0 was expressed as a sum of cosine functions. We here consider only the first mode since higher terms will lead to unrealistic biofilm distributions for small values of x . Assuming $c_{\text{bio}} = 0$, justified above we can write

$$c^0 = \frac{4}{\pi} \cos\left(\frac{\pi}{2}y\right). \quad (5.14)$$

With these considerations we can develop the solution of Equations (5.11a-c) for the Scenarios I to III.

5.3.1. Scenario I

For the case of a channel geometry and a uniform velocity field, i.e. $f(y) = 1$, the solution for the system given by Equations (5.11a) – (5.11c) is

$$c(x, y) = c^0 e^{-\frac{\Phi_{\text{eff}}^2}{P_e} x}, \quad (5.15)$$

with

$$\Phi_{\text{eff}}^2 = \frac{\pi^2}{4} \quad (5.16)$$

defined in analogy to Heße et al. [2009]. For the effective description, i.e. the effective one-dimensional differential equation for the y -averaged concentration $C(x)$, we can write

$$\frac{\partial}{\partial x} C(x) = -\frac{\Phi_{\text{eff}}^2}{Pe} C(x). \quad (5.17)$$

The distribution of the biomass along the x -direction can be calculated by the amount of reactive species being consumed. To that end we average Equation (5.15) over the y -axis and find the first derivative

$$\frac{\partial}{\partial x} C(x) = \frac{2}{Pe} e^{-\frac{\Phi_{\text{eff}}^2}{Pe} x}. \quad (5.18)$$

This relationship must be multiplied with the yield factor Y to get the amount of produced biomass, which is in turn equal to the decaying biomass per timestep, i.e. $c_{\text{mo}}\mu_{\text{dec}}$. As a result we get for the concentration of the microorganisms

$$c_{\text{mo}} = \frac{Y}{\mu_{\text{dec}}} \frac{2}{Pe} e^{-\frac{\Phi_{\text{eff}}^2}{Pe} x}. \quad (5.19)$$

For the case of a parabolic velocity field however, we need to alter this procedure.

5.3.2. Scenario II

In case of parabolic velocity field, i.e. $f(y) = 1.5(1 - y^2)$, we must take the contribution of the different modes into account. As a result the effective description exhibit higher order derivatives as well as a new coefficient of the first

derivative. However, as shown by Balakotaiah and Chang [1995] or Heße et al. [2009] the coefficients of the higher derivatives become small in the diffusion-limited regime prevailing in our model. Consequently, we will only use the new coefficient of the first derivative labeled as v_{eff} .

For the solutions for the concentration of the reactive species we can state in analogy to the Equation (5.15)

$$c(x, y) = c^0 e^{-\frac{\Phi_{\text{eff}}^2}{v_{\text{eff}} Pe} x}, \quad (5.20)$$

with $v_{\text{eff}} \approx 1.4$ according to Heße et al. [2009]. The effective one-dimensional differential equation now reads in analogy to Equation (5.17)

$$v_{\text{eff}} \frac{\partial}{\partial x} C(x) = -\frac{\Phi_{\text{eff}}^2}{Pe} C(x) \quad (5.21)$$

as well as for the concentration of the microorganisms

$$c_{\text{mo}} = \frac{Y}{\mu_{\text{dec}}} \frac{2}{v_{\text{eff}} Pe} e^{-\frac{\Phi_{\text{eff}}^2}{v_{\text{eff}} Pe} x} \quad (5.22)$$

in analogy to Eqution (5.19).

5.3.3. Scenario III

Due to the x - and y -dependency of the flow field in the sinusoid domain Equation (5.11a) is no longer seperable. The approach used above for the derivation of an analytical solution of coupled reactive transport and biofilm growth is therefore not applicable for a sinusoid geometry. We can however, investigate a scenario of intermediate complexity to assess the influence of a varying pore

Section 5.3: Analytical Methods

diameter isolated from the flow field. Assuming a uniform velocity field is certainly an unphysical assumption. Nonetheless, the simplification facilitates the derivation of an analytical solution for this case, which justifies the decision.

For the further analysis the sinusoid will be transformed into a channel geometry with the same volume by introducing

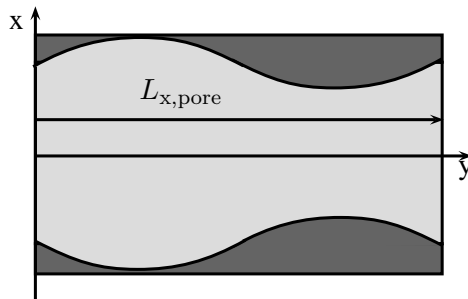
$$\eta = \frac{y}{(1.0 - a \cos(2\pi x/L_{x,pore}))}, \quad (5.23)$$

with a being the amplitude and $L_{x,pore}$ the length of the pore width variation as described in Equation (5.3). As a result we have to adapt the diffusion coefficient, which results in a x -dependent Péclet number

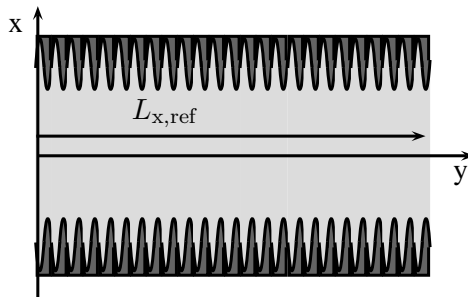
$$\tilde{Pe}(x) = Pe \ g(x) = Pe(1.0 - a \cos(2\pi x/L_{x,pore}))^2. \quad (5.24)$$

As mentionned above the velocity field is assumed to follow a uniform distribution, we can therefore state that $f(\eta) = 1$.

In case of the channel domain the reference length scale in the x -direction $L_{x,ref}$ remained arbitrary since the geometry did not exhibit a characteristic length along that direction (see Figure 5.2). This is in contrast to the case of a sinusoid geometry (see Figure 5.3), with $L_{x,pore}$ denoting the length of the pore width variations (see Figure 5.5a). As stated in Section 5.2.5 however, the reference length $L_{x,ref}$ should correspond to the variations of the pore-scale concentration c along this direction. Since a significant drop of the concentration c in the x -direction within a single pore is an unrealistic assumption we can state $L_{x,ref} \gg L_{x,pore}$ (see Figure 5.5). As a consequence of this clear separation between the different length scales we can apply homogenization theory to find a constant substitute Φ_{eqv}^2 comprising the variations $g(x)$ in Equation (5.24)



(a) Single pore.



(b) Assembly of many pores.

Figure 5.5.: Demonstration of the different scales in case of a sinusoidal geometry.

$$\Phi_{\text{eqv}}^2 = \Phi_{\text{eff}}^2 \int_0^{L_{x,\text{pore}}} \frac{1}{g(x)} dx. \quad (5.25)$$

The derivation of Equation (5.25) requires the application of basic concepts of homogenization theory only and is therefore omitted here. The curious reader is instead referred to the literature on that topic (see e.g.: [Hornung, 1996]).

With the coefficient functions being constant now we can apply the same proceedings as outlined above. For the solution of the concentration of the reactive species we can write

$$c(x, \eta) = \frac{4}{\pi} e^{-\frac{\Phi_{\text{eqv}}^2}{Pe} x} \cos\left(\frac{\pi}{2}\eta\right), \quad (5.26)$$

for the one-dimensional differential equation

$$\frac{\partial}{\partial x} C(x) = -\frac{\Phi_{\text{eqv}}^2}{Pe} C(x) \quad (5.27)$$

as well as for the concentration of the microorganisms

$$c_{\text{mo}} = \frac{Y}{\mu_{\text{dec}}} \frac{\Phi_{\text{eqv}}^2}{\Phi_{\text{eff}}^2} \frac{2}{Pe} e^{-\frac{\Phi_{\text{eqv}}^2}{Pe} x} \quad (5.28)$$

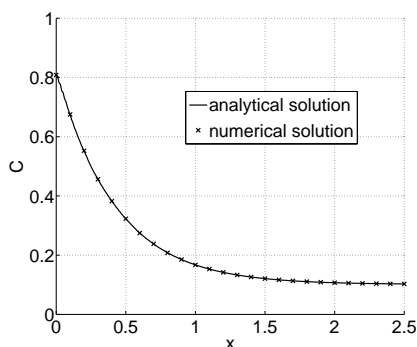
in analogy to Equations (5.15), (5.17) and (5.19) respectively. Due to the reactive surface being bigger in the sinusoid geometry compared to the channel geometry the relationship given by Equation (5.4) must be taken into account when comparing the distribution of the microorganism according to Equations (5.19) and (5.28) in dimensional units. For the nondimensional analysis however, performend herein this difference is not relevant.

5.4. Results and Discussion

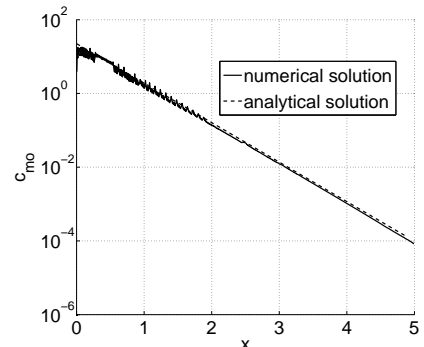
The results presented in this section will cover the four different scenarios as described in Figure 5.4 separately. In addition, we will compare and discuss the results of our model to the findings described by Heße et al. [2009].

5.4.1. Scenario I

In the first part, we investigate the most simple case of a channel domain with a uniform velocity field. This scenario will serve to introduce basic properties of the model to which further attributes will be added in the following sections.



(a) Analytically and numerically calculated averaged concentration C with respect to x for Scenario I.



(b) Analytically and numerically calculated biofilm concentration c_{mo} with respect to x for Scenario I.

Figure 5.6.: Distribution of the averaged concentration of the reactive species C and of the biomass c_{mo} along the channel as described in Figure 5.2 calculated for Scenario I. The coefficients for the numerical calculations were: $Pe = 1$, $Y = 0.1$ and $\mu_{dec} = 0.01$.

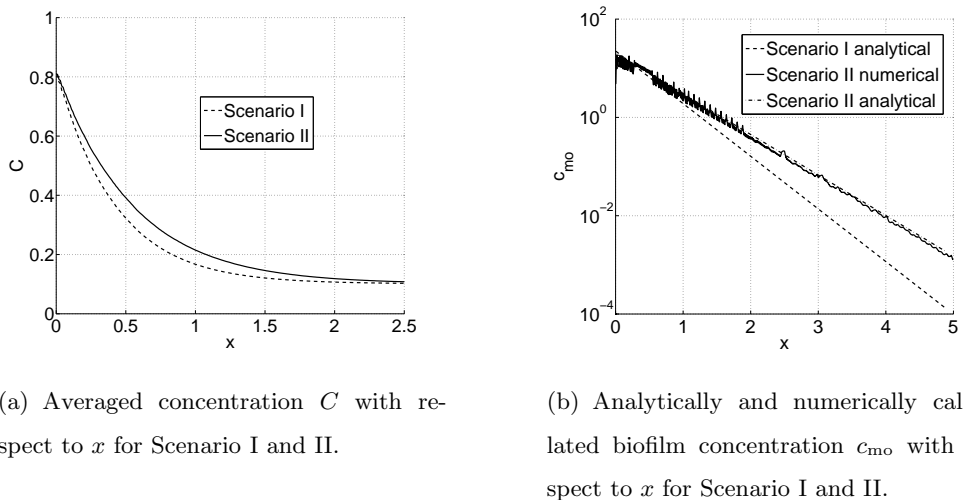
Section 5.4: Results and Discussion

Numerical results obtained for the scenario of a channel geometry with a uniform velocity field show almost perfect agreement with the analytical solutions derived in Section 5.3.1 (Figure 5.6). The bulk concentration C decreases with x in an exponential behavior until saturating at c_{bio} (Figure 5.6a). The concentration of the biomass c_{mo} also behaves according to the analytical solution given by Equation (5.19) (Figure 5.6b). Minor differences between the analytical and numerical results can be found only for small values of x . These deviations remained however, comparably small in all investigated cases.

5.4.2. Scenario II

Assuming all other conditions to remain the same we furthermore discuss the case of a channel geometry with a realistic parabolic velocity field.

The mathematical analysis in Section 5.3.2 revealed the effective velocity term v_{eff} to be the main difference compared to the uniform velocity field. Comparing the solutions of the averaged concentration C (Figure 5.7a) as well as the solutions of the concentration of the microorganisms c_{mo} (Figure 5.7b) from uniform and parabolic velocity fields we see the same qualitative behavior in both cases. In quantitative terms however, a shift between the respective curves can be observed. This shift can be explained by the effective velocity v_{eff} , introduced above, leading to higher values for C in case of a parabolic velocity field compared to a uniform velocity field. This effect can be motivated in physical terms by the higher velocity of the parabolic field in the middle of the channel, where most of the reactive species can be found. The concentration of the microorganisms c_{mo} however, is initially smaller in Scenario II compared to Scenario I due to lower degradation rates and consequently lower biomass production.



(a) Averaged concentration C with respect to x for Scenario I and II.

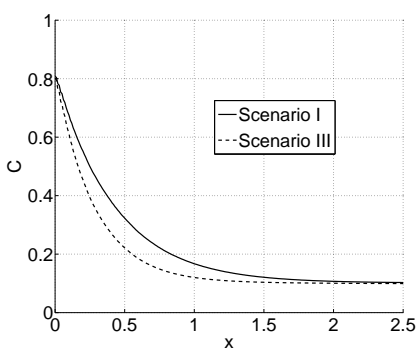
(b) Analytically and numerically calculated biofilm concentration c_{mo} with respect to x for Scenario I and II.

Figure 5.7.: Distribution of the averaged concentration of the reactive species C and of the biomass c_{mo} along the channel calculated for Scenario I and II. The coefficients for the numerical calculations were: $Pe = 1$, $Y = 0.1$ and $\mu_{dec} = 0.01$.

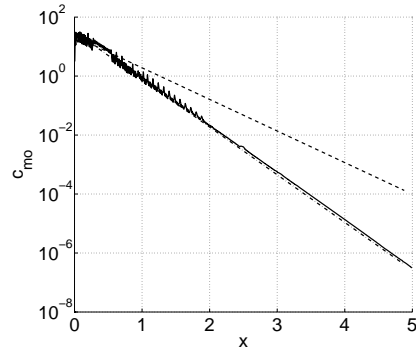
5.4.3. Scenario III

Despite being physically unrealistic the scenario of a uniform flow field is considered here for the assessment of the contribution of the diffusional flux in a sinusoid geometry separately from the velocity field. Furthermore, we can provide an analytical solution for this case, the derivation of which is covered in detail in Section 5.3.3.

Comparing the results from this scenario to findings from Scenario I we see a stronger decrease of the averaged concentration C with respect to x (Figure 5.8a). This can be explained with Φ_{eqv}^2 in Equation (5.25) being higher than Φ_{eff}^2 prevailing in Scenario I. In physical terms we can explain this behavior with



(a) Averaged concentration C with respect to x for Scenario I and II.



(b) Analytically and numerically calculated biofilm concentration c_{mo} with respect to x for Scenario I and III.

Figure 5.8.: Distribution of the averaged concentration of the reactive species C and of the biomass c_{mo} along the channel calculated for Scenario I and Scenario III. The coefficients for the numerical calculations were: $Pe = 1$, $Y = 0.1$ and $\mu_{dec} = 0.01$. The amplitude of the pore width variations for the simulation in Scenario III was $a = 0.5$.

a higher bioavailability in the smaller parts of the pore space surmounting the concurrent declined access in the wider parts (see Figure 5.3). As a result we see an increase in the overall consumption. Similar behavior can be observed for the concentration of the biomass (Figure 5.8b), i.e. we see a stronger decrease of the concentration of the microorganisms in this scenario compared to Scenario I. Since the total amount of injected reactive species and by extension the amount of biomass is identical in both scenarios, values for c_{mo} are initially bigger in Scenario III compared to Scenario I.

5.4.4. Scenario IV

Unlike to the former scenarios we can not derive an analytical solution for the model given by the Equations (5.1a) – (5.1c) when assuming a sinusoid geometry and a realistic velocity field. Therefore, we have to rely on numerical means only to investigate this case. For the calculation of the velocity field in a sinusoid geometry we used the findings of Kechagia et al. [2002].

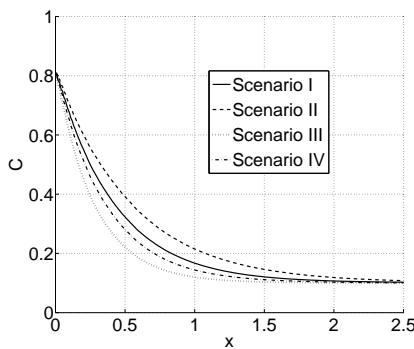


Figure 5.9.: Averaged concentration C with respect to x for all four scenarios.

The parameters for the simulations were: $Pe = 1$, $Y = 0.1$ and $\mu_{dec} = 0.01$.

Comparing the results from this case to those presented above we see a superposition of the described effects in qualitative terms. This comprises an effective velocity caused by the realistic velocity field as well as a higher effective degradation due to the varying diameter of the pore. A quantitative analysis however, reveals differences, i.e. applying v_{eff} and Φ_{eqv}^2 will yield a mismatch between the averaged numerical solutions of the full system and the solutions of the effective description. This mismatch becomes more apparent, as the amplitude a of the sinusoid increases (data not shown). The explanations for this mismatch are twofold: First, we can find increasing transversal velocity

Section 5.4: Results and Discussion

components arising with increasing a . Second, fluid flow and therefore the total amount of injected reactive species is decreasing with increasing a due to the higher inertial forces of the geometry acting on the fluid.

5.4.5. Contributions of the new reactive-transport model

As mentionned above the reactive-transport model used in this study is a modified version of the model reported by Heße et al. [2009]. In this section we will compare these two models with respect to the alterations made herein. These cover the growth of a biofilm as well as the use of a sinusoid geometry.

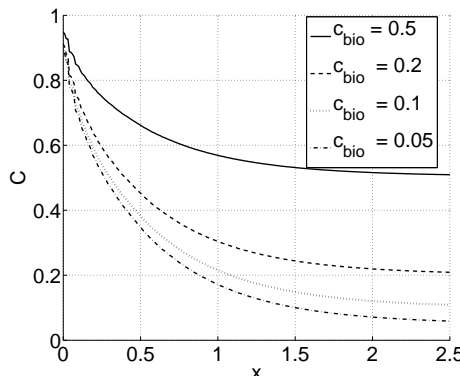


Figure 5.10.: Averaged concentration C for different values of c_{bio} with respect to x for scenario I.

An important difference is the role of the bioavailable concentration c_{bio} . Apart from being constant it furthermore acts as some form of offset to which C is converging for high values of x . Altering one of the coefficients in Equation (5.9) changes the value of c_{bio} and by extension the value to which C converges for high x (Figure 5.10). These results show that the reaction coefficients K_m

and k_{mo} as well as the biomass parameters Y and μ_{dec} influence the distribution of c indirectly.

As revealed by the mathematical analysis in Section 5.3 the steady state of the biofilm growth will lead to a regime comparable to the diffusion-limited regime described by Heße et al. [2009]. Given that c_{bio} approaches zero and assuming all other conditions to be the same both models should yield almost identical solutions, which could be verified by numerical simulations (results not shown).

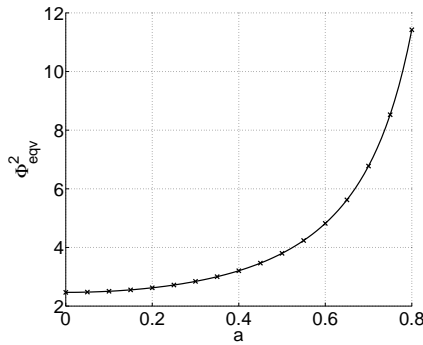


Figure 5.11.: Development of Φ_{eqv}^2 in Scenario III for different amplitudes a .

The discussion of the results from Scenario III demonstrated the increase in the overall consumption due to the increase of Φ_{eqv}^2 . Investigating the behavior of Φ_{eqv}^2 with respect to the amplitude a we see a strong increase of Φ_{eqv}^2 , especially as a approaches 1 (see Figure 5.11). At this value the effective parameter Φ_{eqv}^2 will converge towards infinity. Since this case would correspond in reality to a closed pore this trivial case is not covered in Figure 5.11.

5.5. Summary and Conclusion

In this work we used a two-dimensional geometric representation of the pore space with transport and surface catalyzed degradation of a reactive species. Growth and decay of the microorganisms was explicitly modelled according to the reactive consumption. For the computational domain we applied a simple channel as well as a more elaborated sinusoid geometry. For the analysis four different scenarios of increasing complexity were considered. In the first three scenarios we could provide analytical solutions to support the numerical simulations. In the most realistic fourth scenario however, we had to rely on numerical means only.

It could be shown that in the model used herein the distribution of the biofilm will attune to the incoming diffusional fluxes of the reactive species until balance is achieved between decay and growth. As a result the bioavailable concentration will become spatially constant in the steady state of the biofilm development, which reduces in turn the reactive-transport model to a pure transport model.

For the case of a channel geometry, i.e. Scenarios I and II, the resulting effective system was comparable to the diffusion-limited regime of reactive transport reported by Heße et al. [2009]. This could be explained with the limiting influence of the incoming diffusional fluxes of the reactive species on biofilm growth. We furthermore discussed the occurrence of the coefficient v_{eff} in the effective description of Scenario II compared to Scenario I comprising the effects of the realistic pore-scale velocity field.

In Scenarios III and IV we investigated a more realistic representation of the pore space in form of a sinusoid geometry. For Scenario III we used a physi-

cally unrealistic uniform velocity in analogy to Scenario I. The simplification facilitated the use of analytical tools. We could derive a constant parameter Φ_{eqv}^2 comprising the effect of the pore-width variations of the sinusoid geometry. It was shown that Φ_{eqv}^2 was monotonously increasing with the amplitude a of these variations. This behavior could be explained with the increased access of the microorganisms to the reactive species in the smaller parts of the pore space surmounting the concurrent decrease in the wider parts. In Scenario IV we investigated the most complex case by considering a realistic velocity field in the pore. Lacking an analytical solution in analogy to Scenarios I to III only numerical simulations were presented and discussed. It could be shown that in qualitative terms the behavior can be described with the help of the results presented above. A quantitative analysis however, revealed increasing discrepancies with increasing amplitude a .

6. Synthesis

6.1. Summary and conclusions

Bioavailability is a crucial factor for assessing the effectiveness of biodegradation. Amongst many other factors bioavailability can be significantly reduced by pore-scale mass fluxes. In this thesis the ramifications of these pore-scale mass fluxes on effective degradation rates were investigated. As representation of the pore space we used a two-dimensional channel or sinusoid geometry. The transport of the reactive species was realized by simulating advection and diffusion in the pore volume whereas reactive consumption was realized as boundary conditions at the reactive wall of the medium. Steady state solutions of the system were achieved numerically and/or analytically and averaged transversally to the flow direction resulting in effective one-dimensional solutions. These solutions were used as references for the assessment of effective reaction rates investigated in this study. For these effective reaction rates optimum fit values were used for the derivation of numerical estimates of the unknown parameter of the one-dimensional descriptions. Alternatively analytical estimates could be provided and were tested with respect to accuracy as compared to fitted parameters as well as to exact solutions of the full system. It could be shown that in case of pore-scale Michaelis-Menten kinetics as reaction rate two different

scaling units are to be considered. The first one is the Thiele modulus, which is comparing advective and reactive mass fluxes. This number is therefore a good measure for bioavailability at the pore scale. The second important quantity turned out to be the ratio of the Michaelis constant and the concentration of the reactive species.

In Chapter 3 Michaelis-Menten kinetics was used for the reaction rate of the effective one-dimensional description. As representation of the pore space a channel geometry was used. The analysis of the numerical results showed a complex scaling behavior compared to the marginal case of a first-order reaction rate discussed therein as a reference. Compared to this reference the scaling behavior in the transition regime between the regimes with either high and low bioavailability became additionally concentration dependent in case of Michaelis-Menten kinetics. First a single constant scaling parameter, in analogy to above marginal case, was determined by fitting averaged numerical solutions of the full problem to solutions of the effective description. This lead however, to distinct errors in the transition regime. These errors could be reduced significantly when considering two independent scaling parameters, one for each reaction rate parameter.

In Chapter 4 the same pore-scale model for reactive transport was considered but a linear exchange term was assumed to describe pore-scale mass transport. In steady state this term can be combined with Michaelis-Menten kinetics resulting in the Best-Equation; an alternative reaction rate of the effective one-dimensional description. The mass flux coefficient, being the unknown parameter of the linear exchange term, was determined first in analogy to above procedure by fitting using Best kinetics as effective reaction rate. An error analysis showed a very good conformance in cases of either high or low bioavailability

Section 6.1: Summary and conclusions

with small but negligible errors in the transition regime. In addition a constant estimate was investigated with respect to accuracy, which has been derived analytically from the marginal case of first-order kinetics. A further error analysis with the analytical parameter showed a good conformance, too, with only slightly higher errors compared to the fitted parameter. These properties, i.e. the good accuracy combined with its simplicity, makes the Best-Equation with the analytical estimate for the mass-flux coefficient the best choice for the effective reaction rate compared with the other alternatives considered herein; exhibiting either lower accuracy and/or the need for a usually unknown reference for the fitting process. Finally, the effective description with the Best-Equation as reaction rate using the analytical estimate for the mass-flux coefficient has been applied for the assessment of experimental data exhibiting biodegradation with a limited bioavailability. The analysis could only partially explain the reduced bioavailability in the experiment so further limiting factors were prevailing in the experiment.

In Chapter 5 a modified pore-scale model for reactive transport was investigated, in which explicit biofilm growth was modelled as well as in addition to above channel geometry a more elaborated sinusoid geometry was considered. The mathematical analysis revealed that in steady state the biofilm has evolved such that the bioavailable concentration is spatially constant. As a result the reactive-transport model of the reactive species will be reduced to a pure transport model. The effective reaction rate in case of a channel geometry is then identical to above results for the case of low bioavailability. If a sinusoid geometry is considered the effective reaction rate is increased in proportion to the variations of the pore width.

For practical applications the thesis provided a guideline, when bioavailability restrictions due to pore-scale mass fluxes affect the effective reaction rate, with respect to the relevant quantities; the Thiele modulus as well as the ratio of the species concentration and the Michaelis constant. The Best-Equation with the analytical estimate for the mass-flux coefficient was presented as the best tradeoff between accuracy and applicability. The calculation of these relevant quantities as well as the application of above reaction rate to real world problems was demonstrated by means of experimental data.

6.2. Outlook

With respect to the topic of bioavailability limited by pore-scale mass fluxes this thesis provided several important contributions for the scale of a single pore. The natural step for further research would be the implementation of the derived effective descriptions in a network model of a porous medium consisting of capillary or undulated tubes. Such an approach would facilitate the investigation of further traits of porous media like tortuosity or pore connectivity not comprised in the geometry used herein.

A useful improvement of the pore-scale model itself would be the introduction of a second limiting species. With respect to the reaction kinetics used in this study this would lead to double Monod resp. double Michaelis-Menten kinetics. An expansion from two to three dimensions would likewise allow the investigation of additional relevant effects.

A limitation in the mathematical analysis of the current model used here, which can be improved in the future, is the confinement to low Péclet numbers only. Although being justified for most groundwater systems, high Péclet numbers

Section 6.2: Outlook

can be found in laboratory experiments or chemical reactor systems. Since mass-transfer limitations due to convection dominated flow has been reported in the literature the issue deserves further study and would contribute to the applicability of the model.

Bibliography

UG homepage. URL <http://atlas.gcsc.uni-frankfurt.de/people.html>.

Martin Alexander. Aging, bioavailability, and overestimation of risk from environmental pollutants. *Environmental Science & Technology*, 34(20):4259–4265, 2000.

Pedro J. Alvarez and Walter A. Illman. *Bioremediation and Natural Attenuation*. Wiley & Sons, 2005.

R. Aris. On the dispersion of a solute in a fluid flowing through a tube. *Proceedings of the Royal Society of London. Series A*, 235:67–77, 1956.

Scott Bair and Maura A. Metheny. Remediation of the Wells G & H Superfund Site, Woburn, Massachusetts. *Ground Water*, 40(6):657–668, 2005. doi: 10.1111/j.1745-6584.2002.tb02553.x.

Nikolai S. Bakhvalov and Gregory Panasenko. *Homogenization: Averaging Processes in Periodic Media: Mathematical Problems in the Mechanics of Composite Materials*. Kluwer Academic Pub, 1989. ISBN 0792300491.

Vemuri Balakotaiah and Hsueh-Chia Chang. Dispersion of chemical solutes in chromatographs and reactors. *Philosophical Transactions: Physical Science and Engineering*, 351:39–75, 1995.

Dawid A. Barry, Henning Prommer, Cass T. Miller, Peter Engesgaard, Adam Brun, and Chunmiao Zhen. Modelling the fate of oxidisable organic contaminants in groundwater. *Advances in Water Resources*, 25:945–983, 2002.

Peter Bastian. *Parallele adaptive Mehrgitterverfahren*. Teubner Skripten zur Numerik. Teubner-Verlag, 1996.

Peter Bastian, Klaus Birken, Klaus Johannsen, Stefan Lang, Nikolas Neuß, Hendrik Rentz-Reichert, and Christian Wieners. UG—a flexible toolbox for solving partial differential equations. *Computing & Visualization in Science*, 1:27–40, 1997.

Jacob Bear. *Dynamics of Fluids in Porous Media*. American Elsevier, 1972.

Barbara A. Bekins, Ean Warren, and Michael E. Godsy. A Comparison of Zero-Order, First-Order, and Monod Biotransformation Models. *Ground Water*, 36(2):261 – 268, 1997.

Jay B. Best. The inference of intracellular enzymatic properties from kinetic data obtained on living cells: Some kinetic considerations regarding an enzyme enclosed by a diffusion barrier. *J. Cell. Comp. Physiol.*, 46:1–27, 1955.

Branko Bijeljic, Ann H. Muggeridge, and Martin J. Blunt. Pore-scale modelling of longitudinal dispersion. *Water Resources Research*, 40:149–158, 2004.

Jan Blumschein. Wärme- und Stoffübergang in der flüssigkeitsbedüsten Wirbelschicht. Master's thesis, Otto-von-Guericke-Universität Magdeburg, 2002.

Steve Bonneville, Philippe Van Cappellen, and Thilo Behrends. Microbial reduction microbial reduction of iron(iii) oxyhydroxides: effects of mineral solubility and availability. *Chemical Geology*, 212:255–268, 2004.

Bibliography

- Tom N. P. Bosma, Peter J. M. Middeldorp, Gosse Schraa, and Alexander J. B. Zehnder. Mass transfer limitation of biotransformation: Quantifying bioavailability. *Environmental Science & Technology*, 31(1):248–252, 1997.
- Joseph Boussinesq. *Théorie de l’écoulement tourbillonnant et tumultueux des liquides dans les lits rectilignes à grande section*. Gauthier-Villars et fils, 1897.
- Adam Brun and Peter Engesgaard. Modelling of transport and biogeochemical processes in pollution plumes: literature review and model development. *Journal of Hydrology*, 256:211–227, 2002.
- D. K. Button. Biochemical basis for whole-cell uptake kinetics: Specific affinity, oligotrophic capacity, and the meaning of the michaelis constant. *Applied and Environmental Microbiology*, 57(7):2033–2038, 1991.
- Benito M. Chen. Numerical simulation of biofilm growth in porous media. *Journal of Computational and Applied Mathematics*, 103:55–66, 1999.
- Benito M. Chen, Alfred B. Cunningham, Richard Ewing, R. Peralta, and E. Visser. Two-dimensional modeling of microscale transport and biotransformation in porous media. *Numerical Methods for Partial Differential Equations*, 10(1):65 – 83, 1993.
- N. G. Chikurov. Stability and accuracy of implicit methods for stiff systems of linear differential equations. *Differential Equations*, 42(7):1057–1067, 2006.
- Gui-Yung Chung, Ben J. McCoy, and Kate M. Scow. Criteria to assess when biodegradation is kinetically limited by intraparticle diffusion and sorption. *Biotechnology and Bioengineering*, 41(6):625 – 632, 1993.

-
- Olaf A. Cirpka, E. O. Frind, and Rainer Helmig. Numerical simulation of biodegradation controlled by transverse mixing. *Journal of Contaminant Hydrology*, 40:159–182, 1999.
- Robert M. Corless, Gaston H. Gonnet, David E. G. Hare, David J. Jeffrey, and Donald E. Knuth. On the Lambert W Function. *Advances in Computational Mathematics*, 5:329–359, 1997.
- Gedeon Dagan. *Flow and Transport in Porous Formations*. Springer, 1989.
- Gerhard Damköhler. *Einfluß von Diffusion, Strömung und Wärmetransport auf die Ausbeute bei chemisch-technischen Reaktionen.*, volume 3 of *Der Chemie Ingenieur*. Leipzig, 1937.
- Henry Darcy. *Les Fontaines Publiques de la Ville de Dijon: Exposition et Application des Principes à Suivre et des Formules à Employer dans les Questions de Distribution d'Eau*. Atlas, 1856.
- Hans-Jörg Diersch. Interactive, graphics-based finite element simulation of groundwater contamination processes. *Advances in engineering software*, 15(1), 1992.
- Hubert J. Dupin, Peter K. Kitanidis, and Perry L. McCarty. Pore-scale modeling of biological clogging due to aggregate expansion: A material mechanics approach. *Water Resources Research*, 37(12):2965–2979, 2001a.
- Hubert J. Dupin, Peter K. Kitanidis, and Perry L. McCarty. Simulations of two-dimensional modeling of biomass aggregate growth in network models. *Water Resources Research*, 37(12):2981–2994, 2001b.
- Bruce B. Dykaar and Peter K. Kitanidis. Macrotransport of biologically reacting solute through porous media. *Water Resources Research*, 32:307–320, 1996.

Bibliography

David A. Edwards, Michael Shapiro, and Howard Brenner. Dispersion and reaction in two-dimensional model porous media. *Physics of Fluids A*, 5, 1993.

Laura J. Ehlers and Richard G. Luthy. Contaminant bioavailability in soil and sediment. *Environmental Science & Technology*, 37(15):295–302, 2003.

European Commission. Guidance document on residue analytical methods. Technical report, Directorate General Health and Consumer Protection, 2000.

Adolf Fick. Ueber Diffusion. *Annalen der Physik*, 170:59–86, 1855.

H. Scott Fogler. *Elements of Chemical Reaction Engineering*. Prentice Hall PTR, 3rd edition, 1998. ISBN 0135317088.

Philipp Forchheimer. *Hydraulic*. B. G. Teubner, 1914.

Boris G. Galerkin. Stershin i plastinki. Rjadui w nekotoruich woprosach uprugogo pawnowesija stershnej i plastinok. *Westnik inshenerov*, 1:897–908, 1915.

Jürgen Geiser. *Diskretisierungsverfahren für Systeme von Konvektions-Diffusions-Dispersions-Reaktions-Gleichungen und Anwendungen*. PhD thesis, Ruprecht-Karls-Universität Heidelberg, 2004.

Lynn Gelhar. *Stochastic Subsurface Hydrology*. Prentice-Hall, Engelwood cliffs, 1993.

Lenore J. Gensburg, Cristian Pantea, Edward Fitzgerald, Alice Stark, Syni An Hwang, and Nancy Kim. Mortality among former love canal residents. *Environmental Health Perspectives*, 117(2), 2009. doi: 10.1289/ehp.11350.

-
- Paul-Louis George and Houman Borouchaki. *Delaunay Triangulation and Meshing*. Editions Hermès, 1998.
- Paul-Louis George and Pascal Jean Frey. *Mesh Generation*. Hermès Science Publishing, 2000.
- E. Glueckauf and J.I. Coates. The influence of incomplete equilibrium on the front boundary of chromatograms and the effectiveness of separation. *J. Chem. Soc.*, pages 1315–1321, 1947.
- Carolyn M. Gramling, Charles F. Harvey, and Lucy C. Meigs. Reactive transport in porous media: A comparison of model prediction with laboratory visualization. *Environmental Science & Technology*, 36:2509–2514, 2002.
- Wolfgang Hackbusch. *Multi-Grid Methods and Applications*. Springer, 1985.
- Roy Haggerty and Steven M. Gorelick. Multiple-rate mass-transfer for modelling diffusion and surface-reactions in media with pore-scale heterogeneity. *Water Resources Research*, 31:2383 – 2400, 1995.
- Hauke Harms. Bacterial growth on distant naphthalene diffusing through water, air, and water-saturated and nonsaturated porous media. *Applied Environmental Microbiology*, 62:2286–2293, 1996.
- Hauke Harms and Tom N. P. Bosma. Mass transfer limitation of microbial growth and pollutant degradation. *Journal of Industrial Microbiology and Biotechnology*, 18(2–3):97–105, 1997. doi: 10.1038/sj.jim.2900259.
- Hauke Harms and Alexander J. B. Zehnder. Influence of substrate diffusion on degradation of dibenzofuran and 3-chlorodibenzofuran by attached and suspended bacteria. *Applied and Environmental Microbiology*, 60(8):2736–2745, 1994.

Bibliography

- Charles F. Harvey and Steven M. Gorelick. Temporal moment-generating equations: Modeling transport and mass transfer in heterogeneous aquifers. *Water Resources Research*, 31:1895 – 1911, 1995.
- Nathan W. Haws, William P. Ball, and Edward J. Bouwer. Modeling and interpreting bioavailability of organic contaminant mixtures in subsurface environments. *Journal of Contaminant Hydrology*, 82:255–292, 2006.
- Michel Helfgott and Edith Seier. Some mathematical and statistical aspects of enzyme kinetics. *The Journal of Online Mathematics and Its Applications*, 7, 2007.
- Rainer Helmig, Holger Class, Ralf U. Huber, Hussam Sheta, Richard Ewing, Reinhard Hinkelmann, Hartmut Jakobs, and Peter Bastian. Architecture of the modular program system Mufte ug for simulating multiphase flow and transport processes in heterogeneous porous media. *Mathematische Geologie*, 2:123–131, 1998.
- Falk Heße, Martin Thullner, Florin A. Radu, and Sabine Attinger. Upscaling of the advection-diffusion-reaction equation with Monod reaction. *Advances in Water Resources*, 32(8):1336–1351, 2009. doi: 10.1016/j.advwatres.2009.05.009.
- Rudolf Hilfer. Review on scale dependent characterization of the microstructure of porous media. *Transport in Porous Media*, 46:373–390, 2002.
- Ulrich Hornung. *Homogenization and Porous Media*. Interdisciplinary Applied Mathematics. Springer, 1996.
- Willem Hundsdorfer and Jan G. Verwer. *Numerical Solutions of Time-Dependent Advection-Diffusion-Reaction Equations*. Springer, 2003.

Christelle Hyacinthe, Steve Bonneville, and Philippe Van Cappellen. Reactive iron(iii) in sediments: Chemical versus microbial extractions. *Geochimica et Cosmochimica Acta*, 70:4166–4180, 2006.

Anders R. Johnsen, Lukas Y. Wick, and Hauke Harms. Principles of microbial PAH-degradation in soil. *Environmental Pollution*, 133(1):71–84, 2005.

Maria Kaika. The Water Framework Directive: A New Directive for a Changing Social, Political and Economic European Framework. *European Planning Studies*, 11(3):299–316, 2003. doi: 10.1080/09654310303640.

Makeba Kampara, Martin Thullner, Hans H. Richnow, Hauke Harms, and Lukas Y. Wick. Impact of bioavailability restrictions on microbially induced stable isotope fractionation. 2. experimental evidence. *Environmental Science & Technology*, 42:6552–6558, 2008.

Makeba Kampara, Martin Thullner, Hauke Harms, and Lukas Y. Wick. Impact of cell density on microbially induced stable isotope fractionation. *Applied Microbiology & Biotechnology*, 81:977–985, 2009.

George E. Kapellos, Terpsichori S. Alexiou, and Alkiviades C. Payatakes. Hierarchical simulator of biofilm growth and dynamics in granular porous materials. *Advances in Water Resources*, 30:1648–1667, 2007.

Persefoni E. Kechagia, Ioannis N. Tsimpanogiannis, Yanis C. Yortsos, and Peter C. Lichtner. On the upscaling of reaction-transport processes in porous media with fast or finite kinetics. *Chemical Engineering Science*, 57:2565–2577, 2002.

Bibliography

- Dong-Shik Kim and H. Scott Fogler. Biomass evolution in porous media and its effects on permeability under starvation conditions. *Biotechnology and Bioengineering*, 69(1):47 – 56, 2000.
- Peter K. Kitanidis. Analysis of macrodispersion through volume-averaging: Moment equations. *Stochastic Hydrology and Hydraulics*, 6(1):5–25, 1992.
- Peter K. Kitanidis and Bruce B. Dykaar. Stokes flow in a slowly varying two-dimensional periodic pore. *Transport in Porous Media*, 26:89–98, 1997.
- Peter Knabner and Lutz Angermann. *Numerical Methods for Elliptic and Parabolic Partial Differential Equations*. Springer, 2003.
- Chad E. Knutson, Charles J. Werth, and Albert J. Valocchi. Pore-scale simulation of biomass growth along the transverse mixing zone of a model two-dimensional porous medium. *Water Resources Research*, 41, 2005. doi: 10.1029/2004WR003459.
- Chad E. Knutson, Albert J. Valocchi, and Charles J. Werth. Comparison of continuum and pore-scale models of nutrient biodegradation under transverse mixing conditions. *Advances in Water Resources*, 30:1421–1431, 2007.
- Olaf Kolditz. *Computational Methods in Environmental Fluid Mechanics*. Springer-Verlag, 2002.
- Stefan Lang. Parallel-adaptive simulation with the multigrid-based software framework UG. *Engineering with Computers*, 22(3-4):157–179, 2006.
- Li Li, Catherine A. Peters, and Michael A. Celia. Upscaling geochemical reaction rates using pore-scale network modeling. *Advances in Water Resources*, 29(9):1351–1370, 2006.

-
- Li Li, Carl I. Steefel, and Li Yang. Scale dependence of mineral dissolution rates within single pores and fractures. *Geochimica et Cosmochimica Acta*, 72(2):360–377, 2007.
- Peter C. Lichtner and Qinjun Kang. Upscaling pore-scale reactive transport equations using a multiscale continuum formulation. *Water Resources Research*, 43, 2007.
- Rudolf Liedl, Albert J. Valocchi, Peter Dietrich, and Peter Grathwohl. Finiteness of steady state plumes. *Water Resources Research*, 41(12), 2005. doi: doi:10.1029/2005WR004000.
- Jaroslav Mackerle. 2D and 3D finite element meshing and remeshing: A bibliography (1990-2001). *Engineering Computations: International Journal for Computer-Aided Engineering*, 18(8):1108–1197, 2001.
- Klaus U. Mayer. *A numerical model for multicomponent reactive transport in variably saturated porous media*. PhD thesis, University of Waterloo, 2000.
- Lawrence M. Mayer. Surface area control of organic carbon accumulation in continental shelf sediments. *Geochimica et Cosmochimica Acta*, 58:1271–1284, 1994.
- Michael G. McDonald and Arlen W. Harbaugh. The history of modflow. *Ground Water*, 41(2):280 – 283, 2005. doi: 10.1111/j.1745-6584.2003.tb02591.x.
- Christof Meile and Kagan Tuncay. Scale dependence of reaction rates in porous media. *Advances in Water Resources*, 29(1):62–71, 2006. doi: doi:10.1016/j.advwatres.2005.05.007.
- Leonor Michaelis and Maud L. Menten. Die Kinetic der Invertinwirkung. *Biochemische Zeitschrift*, 49:333–369, 1913.

Bibliography

- Andro Mikelić, Vincent Devigne, and Cornelius J. van Duijn. Rigorous upscaling of a reactive flow through a pore, under important Péclet's and Damköhler's numbers. *SIAM Journal for Mathematical Analysis*, 38(4):1262–1287, 2006.
- Jaques Monod. The growth of bacterial cultures. *Annual Reviews of Microbiology*, 3:371–394, 1949.
- Claus-Dieter Munz and Thomas Westermann. *Numerische Behandlung gewöhnlicher und partieller Differentialgleichungen*. Springer, 2006.
- Ellyn M. Murphy and Timothy R. Ginn. Modeling microbial processes in porous media. *Hydrogeology Journal*, 8:142–158, 2000.
- David D. Myrold and James M. Tiedje. Diffusional constraints on denitrification in soil. *Soil Science Society of America Journal*, 49:651–657, 1985.
- Sandra Nägele. *Mehrgitterverfahren für die inkompressiblen Navier-Stokes Gleichungen im laminaren und turbulenten Regime unter Berücksichtigung verschiedener Stabilisierungsmethoden*. Inaugural-dissertation, Ruprecht-Karls-Universität Heidelberg, November 2003.
- National Research Council (U.S.). *Bioavailability of Contaminants in Soils and Sediments: Processes, Tools, and Applications*. National Academies Press, 2003.
- Claude-Louis Navier. Memoire sur les lois du mouvement des fluides. *Memoire de l'Academie des Science*, 6:389–440, 1823.
- Thimo Neubauer and Peter Bastian. On a monotonicity preserving eulerian-lagrangian localized adjoint method for advection-diffusion equations. *Advances in Water Resources*, 28:1292–1309, 2005.

Gunnar Nützmann, Paolo Viotti, and Per Aagaard. *Reactive Transport in Soil and Groundwater*. Springer, 2005.

M. A. Paine, R. G. Carbonnell, and Stephen Whitaker. Dispersion in pulsed systems. I. Heterogeneous reaction and reversible adsorption in capillary tubes. *Chemical Engineering Science*, 38(11):1781–1793, 1993.

George C. Papanicolaou. Diffusion in random media. *Surveys in Applied Mathematics*, 1:205 – 255, 1995.

Grigorios A. Pavliotis. *Homogenization Theory for Advection-Diffusion Equations with Mean Flow*. PhD thesis, Rensselaer Polytechnic Institute, Troy, NY, 2002.

Alexander Prechtel, Sandro Bitterlich, Florin A. Radu, and Peter Knabner. Natural Attenuation: hohe Anforderungen an die Modellsimulation 'high demands for model simulations'. *Grundwasser*, 11(3):217–225, 2006. ISSN 1432-1165. doi: 10.1007/s00767-006-0147-6.

Florin A. Radu, Marcus Bause, Alexander Prechtel, and Sabine Attinger. *A mixed hybrid finite element discretization scheme for reactive transport in porous media*. Numerical Mathematics and Advanced Applications. Springer, 2008.

Florin A. Radu, Iuliu S. Pop, and Sabine Attinger. Analysis of an Euler implicit - mixed finite element scheme for reactive solute transport in porous media. *Numerical Methods for Partial Differential Equations*, 2009. doi: 10.1002/num.20436.

Bibliography

Deepashree S. Raje and Vivek Kapoor. Experimental study of biomolecular reaction kinetics in porous media. *Environmental Science & Technology*, 34: 1234–1239, 2000. doi: 10.1021/es9908669.

Randolf Rausch, Wolfgang Kinzelbach, René Therrien, and Christian Wagner. *Solute Transport Modelling: An Introduction to Models and Solution Strategies*. Borntraeger, 2005.

Pierre Regnier, J. P. O’Kane, Carl I. Steefel, and Jean-Pierre Vanderborght and. Modeling complex multi-component reactive-transport systems: Towards a simulation environment based on the concept of a knowledge base. *Applied Mathematical Modelling*, 26(9):913–927, 2002.

Phillip Renard and Guy de Marsily. Calculating equivalent permeability: A review. *Advances in Water Resources*, 20:253–278, 1997.

Bruce E. Rittmann. The significance of biofilm in porous media. *Water Resources Research*, 29(7):2195–2202, 1993.

Bruce E. Rittmann. Definition, objectives, and evaluation of natural attenuation. *Biodegradation*, 15(6):349–357, December 2004.

Walter Ritz. Über eine neue Methode zur Lösung gewisser Variationsprobleme der mathematischen Physik. *Journal für die Reine und Angewandte Mathematik*, 135:1–61, 1909.

Paul V. Roberts, Mark N. Goltz, R. Scott Summers, John C. Crittenden, and Peter Nkedi-Kizza. The influence of mass transfer on solute transport in column experiments with an aggregated soil. *Journal of Contaminant Hydrology*, 1:375–393, 1987.

-
- E. E. Roden. Analysis of long-term bacterial vs. chemical Fe(III) oxide reduction kinetics. *Geochimica et Cosmochimica Acta*, 68:3205–3216, 2004.
- Philip G. Saffman. A theory of dispersion in a porous medium. *Journal of Fluid Mechanics*, 6(3):321–349, 1959. doi: 10.1017/S0022112059000672.
- Dirk Schäfer, Wolfgang Schäfer, and Wolfgang Kinzelbach. Simulation of reactive processes related to biodegradation in aquifers, 1. Structure of the three-dimensional reactive transport model. *Journal of Contaminant Hydrology*, 31(1-2):167–186, 1998.
- Adrian E. Scheidegger. *The physics of flow through porous media*. University of Toronto Press, 1974.
- Santiago Schnell and Claudio Mendoza. Closed form solution for time-dependent enzyme kinetics. *Journal of Theoretical Biology*, 187:207–212, 1997.
- Kirk T. Semple, A.W.J. Morriss, and Graeme I. Paton. Bioavailability of hydrophobic organic contaminants in soil: fundamental concepts and techniques for analysis. *European Journal of Soil Science*, 54:809–818, 2003.
- Kirk T. Semple, Kieron J. Doick, Kevin C. Jones, Peter Burauel, Andrew Craven, and Hauke Harms. Defining bioavailability and bioaccessibility of contaminated soil and sediment is complicated. *Environmental Science & Technology*, 38(12):228A–231A, 2004.
- Stefano F. Simoni, Anke Schäfer, Hauke Harms, and Alexander J. B. Zehnder. Factors affecting mass transfer limited biodegradation in saturated porous media. *Journal of Contaminant Hydrology*, 50:99–120, 2001.

Bibliography

Carl I. Steefel and Kerry T. B. MacQuarrie. Approaches to modeling of reactive transport in porous media. *Reviews in Mineralogy and Geochemistry*, 34(1): 85–129, 1996.

George Gabriel Stokes. On the steady motion of incompressible fluids. *Transactions of the Cambridge Philosophical Society*, 7:439–453, 1842.

William G. Strang and George J. Fix. *An Analysis of the Finite Element Method*. Wellesley Cambridge Press, 1973.

Brian J. Suchomel, Benito M. Chen, and Myron B. Allen III. Network model of flow, transport and biofilm effects in porous media. *Transport in Porous Media*, 30(1):1–23, January 1998.

Geoffrey I. Taylor. Dispersion of soluble matter in solvent flowing slowly through a tube. *Proceedings of the Royal Society of London. Series A*, 219:186–203, 1953.

Ernest W. Thiele. Relation between catalytic activity and size of particle. *Industrial Engineering Chemistry*, 31:916–920, 1939.

Georg Thiem. *Hydrologische Methoden*. Gebhardt Leipzig, 1906.

Martin Thullner, Laurie Mauclaire, Martin H. Schroth, Josef Zeyer, and Wolfgang Kinzelbach. Interaction between water flow and spatial distribution of microbial growth in a two-dimensional flow field in saturated porous media. *Journal of Contaminant Hydrology*, 58:169–189, 2002a.

Martin Thullner, Josef Zeyer, and Wolfgang Kinzelbach. Influence of microbial growth on hydraulic properties of pore networks. *Transport in Porous Media*, 49(1):99–122, 2002b.

Martin Thullner, Philippe Van Cappellen, and Pierre Regnier. Modeling the impact of microbial activity on redox dynamics in porous media. *Geochimica et Cosmochimica Acta*, 69(21):5005–5019, 2005.

Martin Thullner, Pierre Regnier, and Philippe Van Cappellen. Modeling microbially induced carbon degradation in redox stratified subsurface environments: concepts and open questions. *Geomicrobiology Journal*, 24:139–155, 2007.

Martin Thullner, Makeba Kampara, Hans H. Richnow, Hauke Harms, and Lukas Y. Wick. Impact of bioavailability restrictions on microbially induced stable isotope fractionation. 1. theoretical calculation. *Environmental Science & Technology*, 42(17):6544–6551, 2008.

Olga V. Ushakova. *Advances in Grid Generation*. Nova Science Publishers, 2007.

Cornelius J. van Duijn, Andro Mikelić, Iuliu S. Pop, and Carole Rosier. Effective dispersion equations for reactive flows with dominant Péclet and Damköhler numbers. *Advances in Chemical Engineering*, 34:1–45, 2008.

Jos van Kan, Guus Segal, and Fred Vermolen. *Numerical Methods in Scientific Computing*. VSSD, first edition edition, 2005. ISBN 13 978-90-6562-179-5.

Mark C.M. van Loosdrecht, Joseph J. Heijnen, Hermann J. Eberl, Jan-Ulrich Kreft, and Christian Picóoreanu. Mathematical modelling of biofilm structures. *Antonie van Leeuwenhoek*, 81:245–256, 2000.

Jacques Villermaux. Chemical engineering approach to dynamic modelling of linear chromatography: a flexible method for representing complex phenomena from simple concepts. *Journal of Chromatography*, 406:11–26, 1987.

Bibliography

- Hans-Jörg Vogel. Topological characterization of porous media. *Morphology of Condensed Matter*, 600:75–92, 2002.
- Oskar Wanner, Alfred B. Cunningham, and Richard Lundmann. Modeling biofilm accumulation and mass transport in a porous medium under high substrate loading. *Biotechnology and Bioengineering*, 47(6):703–712, 1995.
- Ian A. Watson, Roger S. Crouch, Peter Bastian, and Sascha Oswald. Advantages of using adaptive remeshing and parallel processing for modelling biodegradation in groundwater. *Advances in Water Resources*, 28(11):1143–1158, November 2005.
- Stephen Whitaker. *The method of volume averaging. Theory and applications of transport in porous media*. Dordrecht: Kluwer, 1999.
- Todd H. Wiedemeier, Hanadi S. Rifai, John T. Wilson, and Charles Newell. *Natural Attenuation of fuels and chlorinated solvents in the subsurface*. John Wiley & Sons, 1999.
- Brian D. Wood. The role of scaling laws in upscaling. *Advances in Water Resources*, 2008.
- Brian D. Wood, Karen Radakovich, and Fabrice Golfier. Effective reaction at a fluid-solid interface: applications to biotransformation in porous media. *Advances in Water Resources*, 30:1630–1647, 2007.
- World Health Organization. *Guidelines for drinking-water quality*. World Health Organization, 1997.
- Dirk F. Young and William P. Ball. Effects of column conditions on the first-order rate modelling of nonequilibrium solute breakthrough. *Water Resources Research*, 31:2181 – 2192, 1995.

Tjalling J. Ypma. Historical development of the Newton-Raphson method.
SIAM Review, 37(4):531–551, 1995. doi: 10.1137/1037125.

Andrew R. Zimmermann, Keith W. Goyne, Jon Chorover, Sridhar Komarneni, and Susan L. Brantley. Mineral mesopore effects on nitrogenous organic matter adsorption. *Organic Geochemistry*, 35:355–375, 2004.

A. Appendix of Chapter 3

A.1. Development of the upscaled solution

In this appendix we will provide the details for the upscaling of the pore-scale processes. This comprises (i) the analytical solution as well as (ii) the effective differential equation. The Equations (3.6a) – (3.6c) describing these processes can be found in the body of the study and will not be listed again.

A.1.1. Separation of the variables

The scheme used to derive an analytical solution in case of first-order kinetics can be found in [Balakotaiah and Chang, 1995]. It has been modified to account for the mathematical and geometrical description used in this study.

Transversal direction Let $\{\lambda_i\}_{i \geq 1}$ be the set of eigenvalues and $\{\Psi_i\}_{i \geq 1}$ the respective set of orthonormal eigenfunctions of the following self-adjoint eigenvalue problem

$$\frac{\partial^2}{\partial y^2} \Psi_i(y) = -\lambda_i^2 \Psi_i(y), \quad (\text{A.1a})$$

$$\frac{\partial}{\partial y} \Psi_i|_{y=0} = 0, \quad (\text{A.1b})$$

$$\frac{\partial}{\partial y} \Psi_i|_{y=1} = -\Phi^2 \Psi_i|_{y=1}. \quad (\text{A.1c})$$

The boundary condition given by Equation (A.1b) reflects the symmetry of the medium and Equation (A.1c) is the reaction term in case of first-order kinetics. The solution of Equation (A.1a) is known to consist of the trigonometric functions sine and cosine. Therefore we can write

$$\Psi_i(y) = A_i \cos(\lambda_i y) + B_i \sin(\lambda_i y). \quad (\text{A.2})$$

Here λ_i is the frequency and A_i and B_i are the respective amplitudes. These coefficients have to match the boundary conditions. First we use the boundary condition given by Equation (A.1b)

$$\frac{\partial}{\partial y} \Psi_i|_{y=0} = 0 = B_i \cos(0) - A_i \sin(0) \quad (\text{A.3})$$

from which is clear that $B_i = 0$. The boundary condition given by Equation (A.1c) yields

$$\frac{\partial}{\partial y} \Psi_i|_{y=1} = -\Phi^2 A_i \cos(\lambda_i) = -A_i \lambda_i \sin(\lambda_i). \quad (\text{A.4})$$

Rearranging this expression we get

$$\lambda_i \tan(\lambda_i) = \Phi^2. \quad (\text{A.5})$$

Appendix A

The behavior of the left hand side of Equation (A.5) is that of a strictly monotonously increasing curve from $-\infty$ to $+\infty$ within each interval $(\frac{i}{2}\pi, (\frac{i}{2} + 1)\pi)$ with $(i = 1, 3, 5, \dots)$. The solutions λ_i are therefore determined by evaluate this expression within each of this intervals. (Figure A.1).

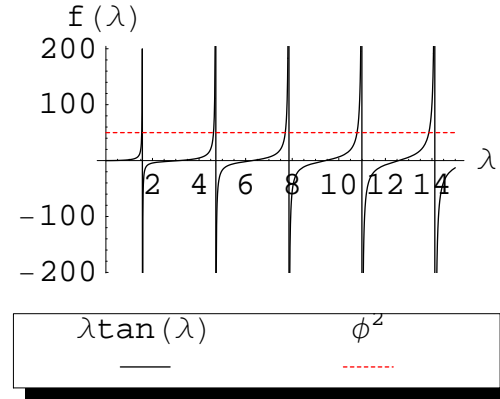


Figure A.1.: Solution of the eigenvalue problem described by Equation (A.5) displayed as the interfaces of the $\lambda \tan(\lambda)$ function (continuous line) and a constant reaction rate (dashed line, arbitrarily set to $\Phi^2 = 50$ in this example).

For the calculation of the amplitudes A_i we refer to the ortho-normality of the eigenfunctions, i.e.

$$\int_0^1 \Psi_i \Psi_j \ dy = \delta_{i,j} \quad (\text{A.6})$$

When we use this condition and insert Equation (A.2), we get

$$A_i = \left(\int_0^1 \cos^2(\lambda_i y) \ dy \right)^{-\frac{1}{2}} = 2 \sqrt{\frac{\lambda_i}{\sin(2\lambda_i) + 2\lambda_i}}. \quad (\text{A.7})$$

Now we can formulate the explicit solution for every transversal mode of Equation (3.8) by introducing the values for A_i and B_i into Equation (A.2)

$$\Psi_i(y) = 2 \sqrt{\frac{\lambda_i}{\sin(2\lambda_i) + 2\lambda_i}} \cos(\lambda_i y). \quad (\text{A.8})$$

Longitudinal direction In order to solve for the longitudinal part of every mode we insert Equation (3.8) into Equation (3.6a)

$$Pe f(y) \sum_{i=1}^{\infty} \Psi_i(y) \frac{\partial}{\partial x} C_i(x) = \sum_{i=1}^{\infty} C_i(x) \frac{\partial^2}{\partial y^2} \Psi_i(y). \quad (\text{A.9})$$

Multiplying this equation by Ψ_j and integrating over y yields

$$Pe \sum_{i=1}^{\infty} \int_0^1 f(y) \Psi_i(y) \Psi_j(y) dy \frac{\partial}{\partial x} C_i(x) = \sum_{i=1}^{\infty} C_i(x) \int_0^1 \frac{\partial^2}{\partial y^2} \Psi_i(y) \Psi_j(y) dy. \quad (\text{A.10})$$

By defining

$$\int_0^1 f(y) \Psi_i \Psi_j dy = \tau_{ij} \quad (\text{A.11})$$

and inserting Equation (A.1a), because of the ortho-normality of the Ψ_i 's (A.6) we get

$$\sum_{i=1}^{\infty} \tau_{ij} \frac{\partial}{\partial x} C_i(x) = -\frac{\lambda_j^2}{Pe} C_j(x). \quad (\text{A.12})$$

To get a good approximation of the complete solution a finite number of modes will certainly be sufficient. By considering only N modes of the series we can rewrite Equation (A.12) in a matrix notation

$$\mathbf{T} \frac{\partial}{\partial x} \mathbf{C} = \boldsymbol{\Lambda} \mathbf{C} \quad (\text{A.13})$$

with

$$\mathbf{T} = \begin{pmatrix} \tau_{11} & \cdots & \tau_{1N} \\ \vdots & \ddots & \vdots \\ \tau_{N1} & \cdots & \tau_{NN} \end{pmatrix}, \quad (\text{A.14})$$

$$\boldsymbol{\Lambda} = \begin{pmatrix} -\frac{\lambda_1^2}{Pe} & & 0 \\ & \ddots & \\ 0 & & -\frac{\lambda_N^2}{Pe} \end{pmatrix} \quad (\text{A.15})$$

and

$$\mathbf{C} = \begin{pmatrix} C_1 \\ \vdots \\ C_N \end{pmatrix} \quad (\text{A.16})$$

for the unknown vector \mathbf{C} , whose entries are the longitudinal modes of the solution c . Equation (A.13) can be rearranged into

$$\frac{\partial}{\partial x} \mathbf{C} = \mathbf{T}^{-1} \boldsymbol{\Lambda} \mathbf{C} = \boldsymbol{\Gamma} \mathbf{C} \quad (\text{A.17})$$

In this form we have a simple system of homogeneous linear differential equations of order one with constant coefficients.

A.1.2. Analysis of the case of first-order kinetics with a uniform velocity field

In this part of the appendix we will give the details for the case of first-order kinetics with a uniform velocity field. This comprises the analytical solution as well as the effective equation (see Figure 3.5).

Analytical solution In case of a uniform velocity field the matrix \mathbf{T} is the identity matrix according to Equation (A.11). Therefore $\boldsymbol{\Gamma}$ is diagonal and the Equations (3.10) are decoupled. The governing ordinary differential equation for every mode then reads

$$\frac{\partial}{\partial x} C_i(x) = -\frac{\lambda_i^2}{Pe} C_i(x) \quad (\text{A.18})$$

The solution of this equation is known to be

$$C_i(x) = C_i(0)e^{-\frac{\lambda_i^2}{Pe}x}. \quad (\text{A.19})$$

For the evaluation of the initial conditions $C_i(0)$ we have to refer to Equation (3.8) and insert the boundary condition given by Equation (3.6b)

$$1 = c(0, y) = \sum_{i=1}^N C_i(0) \Psi_i(y) \quad (\text{A.20})$$

multiplying both sides with Ψ_j and integrating over y yields

$$C_j(0) = \int_0^1 c(0, y) \Psi_j(y) dy \quad (\text{A.21})$$

Appendix A

because of the ortho-normality of the eigenfunctions $\Psi_i(y)$. Since $c(0, y) = 1$ we finally arrive at

$$C_j(0) = \int_0^1 \Psi_j(y) dy = A_j \frac{\sin(\lambda_j)}{\lambda_j}. \quad (\text{A.22})$$

With this equation we get the starting value for every transversal mode C_j of the solution.

Effective equation To find the upscaled effective description of Equation (3.6) we directly apply the upscaling operator $\int_0^1 dy$ to Equation (3.6a) and insert the boundary conditions given by the Equations (3.6b) and (3.6c). In case of the uniform velocity field we get

$$\begin{aligned} \int_0^1 Pe \frac{\partial}{\partial x} c dy &= \int_0^1 \frac{\partial^2}{\partial y^2} c dy \\ Pe \frac{\partial}{\partial x} C &= \frac{\partial}{\partial y} c_{\text{bio}} - \frac{\partial}{\partial y} c|_{y=0} \\ &= -\Phi^2 c_{\text{bio}}. \end{aligned}$$

Here we introduce an effective Thiele modulus Φ_{eff}^2 , as

$$\Phi_{\text{eff}}^2 = \frac{c_{\text{bio}}}{C} \Phi^2. \quad (\text{A.23})$$

Since C is only zero at $+\infty$ this equation is valid almost everywhere. It can be shown that Φ_{eff}^2 shows only variation for small values of x so it can be approximated as a constant.

A.1.3. Analysis of the case of first-order kinetics with a parabolic velocity field

Analytical solution the matrix \mathbf{T} is no longer a diagonal matrix in case of a parabolic velocity field. As a result the entries of \mathbf{C} in Equation (3.10) are now coupled and must be solved in a closed form. Nevertheless, the matrix \mathbf{T} is still symmetric, so $\tau_{ij} = \tau_{ji}$ (Figure A.2).

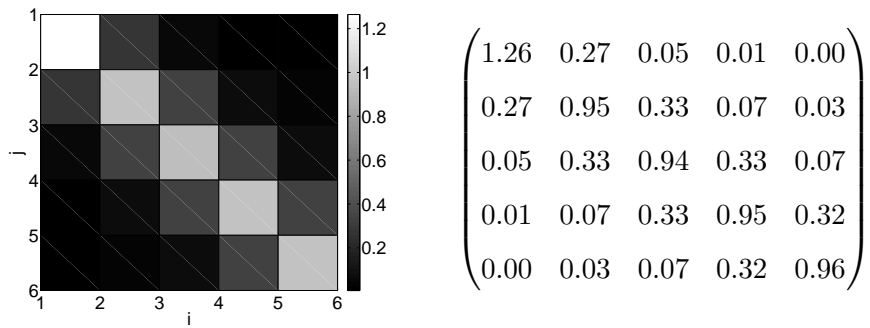


Figure A.2.: First five rows and columns of matrix \mathbf{T} in graphical and numerical display, evaluated for $\Phi^2 = 10$ in case of first-order kinetics and a parabolic velocity field.

To find the solution of Equation (3.10) we diagonalize the system matrix Γ . To that end we have to find a representation of the form $\Gamma = \mathbf{G}\mathbf{D}\mathbf{G}^{-1}$. Here \mathbf{D} is a diagonal matrix and \mathbf{G} is the orthogonal matrix of the eigenvectors of Γ . Applying this transformation we can rewrite Equation (3.10) into

$$\mathbf{c}' = \Gamma\mathbf{C} = \mathbf{G}\mathbf{D}\mathbf{G}^{-1}\mathbf{C}$$

$$\mathbf{G}^{-1}\mathbf{c}' = \mathbf{D}\mathbf{G}^{-1}\mathbf{C}$$

$$\mathbf{w}' = \mathbf{D}\mathbf{w}$$

with $\mathbf{w} = \mathbf{G}^{-1}\mathbf{C}$. In this form the modes are decoupled so we can follow the same proceedings as in case of a uniform velocity field.

Effective equation A direct analytical upscaling like in Section A.1.2 is not possible in case of a parabolic velocity field. Applying the upscaling operator $\int_0^1 dy$ on Equation (3.6a) we get

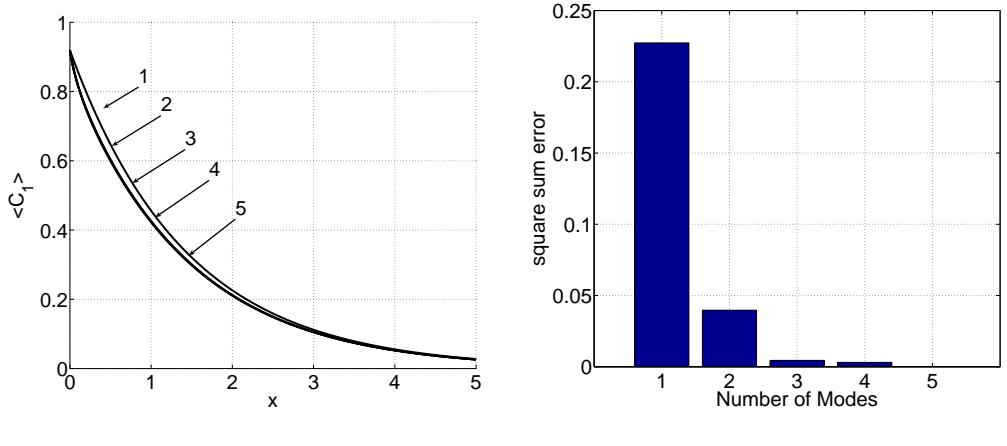
$$1.5 \frac{\partial}{\partial x} \left(C - \int_0^1 y^2 c \, dy \right) = -\frac{\Phi_{\text{eff}}^2}{P_e} C. \quad (\text{A.24})$$

Unfortunately no explicit solution is known for the remaining integral in Equation (A.24). Therefore we have to pursue an alternative proceeding to arrive at an effective equation. Using the linear system of ordinary differential Equations (A.17) we can get an expression for the leading first mode $C_1(x)$. In order to obtain the effective description we have to rewrite the system of N differential equations of order 1 to an ordinary differential equation of order N . The general solution of this procedure is

$$\sum_{n=0}^N a_n \frac{\partial^n}{\partial x^n} C_1 = 0. \quad (\text{A.25})$$

In Equation (A.25) the numbers a_n are the respective coefficients of the characteristic polynomial of Γ in Equation (A.17). To link the solution for this mode with the upscaled solution C we have to multiply it with the corresponding y -averaged transversal mode: $\langle C_1 \rangle = C_1 \int \Psi_1 \, dy$. Since $C = \sum_i \langle C_i \rangle$ holds, we make an error by neglecting the higher modes of C . Nevertheless, these modes decrease very fast so the error is confined to small values of x and even there it is comparably small. An important simplification can be made, regarding the

number of modes N , which has to be taken into account, to arrive at a good estimate for C_1 .



(a) The y -averaged first mode $\langle C_1 \rangle$ calculated using different number of modes.
(b) Square sum error for several modes.

Figure A.3.: Error made by using only a limited number of longitudinal modes for the calculation of $\langle C_1 \rangle$ in case of first-order kinetics and a parabolic velocity field.

A numerical analysis shows that a good approximation is already reached by using few modes (see Figure A.3). Only in the case when one mode is considered, i.e. the first mode itself, we get a significant error. This error however decreases dramatically when using more modes, which justifies the use of only two. By restricting therefore our analysis to $N = 2$ we get a differential equation of second order for C_1 .

A.1.4. Analysis of the case of Michaelis-Menten kinetics

For Michaelis-Menten kinetics given by

$$\nabla c \cdot \mathbf{n} = -\frac{\Phi^2 c_{\text{bio}}}{1 + c_{\text{bio}}/K_m} \quad (\text{A.26})$$

the procedure presented in Appendix A.1.1 must to be modified.

Transversal direction The coefficients of the transversal component in Equation (3.8) now depend on the concentration

$$\frac{\partial}{\partial y} \Psi|_{y=1} = -\frac{\Phi^2}{1 + c_{\text{bio}}/K_m} \Psi|_{y=1}. \quad (\text{A.27})$$

Applying the same procedure as for first-order kinetics, the equation for the evaluation of the eigenvalues in Equation (A.5) now reads

$$\lambda_i \tan(\lambda_i) = \frac{\Phi^2}{1 + c_{\text{bio}}/K_m}. \quad (\text{A.28})$$

Furthermore, the calculation of the the transversal modes is modified to

$$\Psi_i(x, y) = A_i(x) \cos(\lambda_i(x)y). \quad (\text{A.29})$$

Because of the nonlinearity of this problem the coefficients $\lambda_i(x)$ has to be found in an iterative scheme, where the solution of each step serves as a guess for their evaluation.

Longitudinal direction The procedure to arrive at Equation (A.17) has to be modified as well when considering the case of Michaelis-Menten kinetics. Now it reads

$$\mathbf{T}(x) \frac{\partial}{\partial x} \mathbf{c}(x) + \mathbf{B}(x) \mathbf{c}(x) = \boldsymbol{\Lambda}(x) \mathbf{c}(x). \quad (\text{A.30})$$

Here the entries of the matrix $\mathbf{B}(x)$ are given by

$$\beta_{ij}(x) = \int_0^1 f(y) \left(\frac{\partial}{\partial x} \Psi_j(x, y) \right) \Psi_i(x, y) dy. \quad (\text{A.31})$$

Rearranging yields

$$\frac{\partial}{\partial x} \mathbf{c}(x) = \mathbf{T}(x)^{-1} (\mathbf{\Lambda}(x) - \mathbf{B}(x)) \mathbf{c}(x) = \mathbf{\Gamma}(x) \mathbf{c}(x), \quad (\text{A.32})$$

so we get again a system of homogeneous linear differential equations. In contrast to Equation (A.17) the entries of the coefficient matrix $\mathbf{\Gamma}(x)$ are not constants but x -dependent functions.

B. Appendix of Chapter 4

B.1. Analytical estimate for j_{tr}

In addition to solving the full problem given by Equations (4.14) and (4.15) numerically the simplicity of the chosen geometry of the pore channel (see Figure B.1) allows for obtaining analytical solutions of this equation for the case of very low concentrations compared to the Michaelis constant K_m . In this case the obtained analytical results allow deriving an constant expression for the mass-flux coefficient j_{tr} .

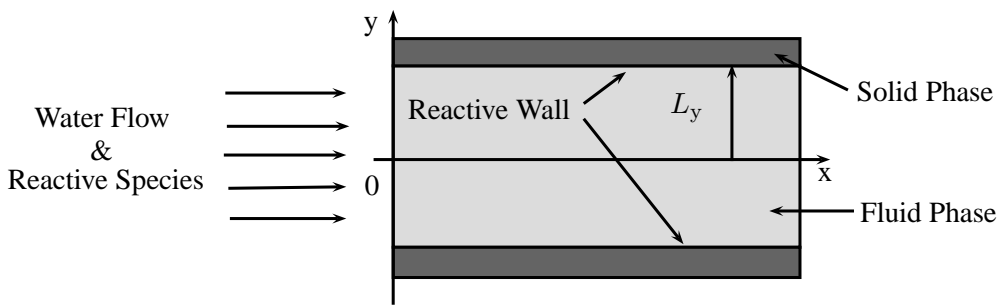


Figure B.1.: Schematic representation of the geometry used to describe processes in a single pore.

For concentrations sufficiently small compared to the Michaelis constant K_m , Michaelis-Menten kinetics is effectively identical to first-order kinetics. In that case, we can write for the reactive flux given by Equation (4.15)

$$q_{\text{reac}} = -\Phi^2 c_{\text{bio}}. \quad (\text{B.1})$$

Assuming $C \ll K_m$ or $C/K_m \ll 1$ and rearranging Equation (4.17) for the mass-flux coefficient yields

$$\begin{aligned} j_{\text{tr}} &= \frac{Q^2 - \Phi^2 K_m Q}{K_m Q - \Phi^2 K_m C} \\ &= \frac{Q^2 / K_m - \Phi^2 Q}{Q - \Phi^2 C} \\ &\approx \frac{-\Phi^2 Q}{Q - \Phi^2 C}. \end{aligned}$$

Reconverting this expression for the macroscopic reactive flux Q , leads to a significantly simpler expression for Best kinetics (Equation (4.17)), which is valid for small concentrations

$$Q = -\frac{j_{\text{tr}} \Phi^2}{j_{\text{tr}} + \Phi^2} C. \quad (\text{B.2})$$

This equation constitutes again a first-order reaction rate but now with respect to the macroscopic concentration C . Our approach apparently does not alter the structure of the reaction kinetics. Comparing this expression to Equation (B.1) allows the introduction of a new effective first-order rate constant using the relationship

$$Q = -\Phi_{\text{eff}}^2 C \quad (\text{B.3})$$

with the effective rate constant given by

$$\Phi_{\text{eff}}^2 = \frac{j_{\text{tr}} \Phi^2}{j_{\text{tr}} + \Phi^2}. \quad (\text{B.4})$$

Equation (B.4) describes an effective Thiele modulus Φ_{eff}^2 , which is linked to the local Thiele modulus Φ^2 , via the mass-flux coefficient j_{tr} . The value of which is given by Φ_{eff}^2 in the limit of $\Phi^2 \rightarrow \infty$. As shown by Balakotaiah and Chang [1995] or Heße et al. [2009], an analysis of the behavior of this effective Thiele modulus Φ_{eff}^2 is mathematically coupled to the square of the first solution of the transcendent equation

$$\lambda \tan(\lambda) = \Phi^2. \quad (\text{B.5})$$

Details on how to derive Equation (B.5) from the problem described in the main manuscript are given in these references. For $\Phi^2 \rightarrow \infty$ the first solution of Equation (B.5) is simply the first pole of the tangent function ($\pi/2$), so

$$j_{\text{tr}} = \frac{\pi^2}{4}. \quad (\text{B.6})$$

It is necessary to note that this solution for j_{tr} has been derived for the used geometry (Figure B.1) and different pore geometries may lead to significantly different results and thus different values for j_{tr} . The results are however, consistent with the findings of Haggerty and Gorelick [1995] for example for the case of layered diffusion. In case of a first-order reaction rate the mass-flux coefficient j_{tr} can therefore be regarded as a geometry parameter describing the effect of pore-scale diffusion on macroscopic reaction rates in the chosen setup.

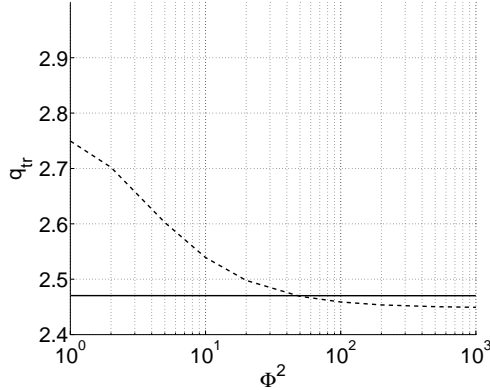


Figure B.2.: Numerical estimate of the mass-flux coefficient j_{tr} with respect to Φ^2 in case of an effective first-order reaction rate (dashed line). The analytically derived value $j_{\text{tr}} = \pi^2/4$ is plotted as solid line.

To test the analytically determined value for j_{tr} we use direct numerical simulations of the full problem described by Equations (4.14) and (4.15) again assuming $C/K_m \ll 1$. For lower values of Φ^2 , i.e. in the reaction-limited regime, the results show an increasing error (see Figure B.2). The error also shows the limits of the assumption of a perfect first-order reaction rate as represented by Equation (B.4). For high values of Φ^2 (see Figure B.2), i.e. in the diffusion-limited regime, the results show a good approximation with only a small bias. This error apparently stems from the numerical discretization of the implemented scheme.

B.2. Effective bioavailability

Following Kampara et al. [2008] the effective bioavailability B_{eff} is given as the ratio between the effective degradation rate given by Best kinetics and the

potential degradation rate in the absence of any bioavailability restrictions given by Michaelis-Menten kinetics:

$$B_{\text{eff}} = \frac{R_{\text{Best}}}{R_{\text{MM}}} = \frac{Q_{\text{Best}}}{Q_{\text{MM}}} \quad (\text{B.7})$$

with R and Q describing dimensional and dimensionless rate expressions, respectively. The subscripts *Best* and *MM* refer to Best kinetics and Michaelis-Menten kinetics. Using Equation (4.17) (with a constant estimate for j_{tr}) for Q_{Best} and Equation (4.18) (with local values for Φ^2 and K_m) for Q_{MM} leads to

$$B_{\text{eff}} = \frac{\pi^2}{8\Phi^2} \left(1 + \frac{K_m}{C} \right) \left(1 + \frac{C}{K_m} + \frac{4\Phi^2}{\pi^2} \right) \left(1 - \sqrt{1 - \frac{16 \frac{C}{K_m} \frac{\Phi^2}{\pi^2}}{\left(1 + \frac{C}{K_m} + \frac{4\Phi^2}{\pi^2} \right)^2}} \right). \quad (\text{B.8})$$

As a result Equation (B.8) contains only local variables.

B.3. Experimental setup

The experimental setup represents one of the column experiments described in Harms and Zehnder [1994]. Glass columns of 8.9 cm bed length above a glass frit at the bottom and 1 cm inner diameter were filled with glass spheres of 0.45 mm diameter. This glass bead packing was fully saturated with phosphate-buffered saline (PBS) and operated in down-flow mode by peristaltic pumping. A bacterial suspension was percolated through the columns to allow for irreversible attachment of biomass equivalent to 0.248 mg protein per column. The attached biomass was calculated from the difference between inflowing and outflowing biomass. The inflow was then switched first to cell-free PBS to remove

planktonic and loosely attached cells and then to a $1.55 \mu M$ solution of 3-chlorodibenzofuran in PBS. The disappearance of the substrate 3-chlorodibenzofuran during passage of the columns was used to calculate the specific degradation activity in the columns. Control experiments with inactive biomass confirmed that losses due to bioaccumulation, volatilization or sorption to tubing or column materials were negligible. A detailed description of the experimental procedures and measurement techniques is given in Harms and Zehnder [1994] and an overview of parameter values measured for this experiment is provided in Table B.1.

length l	8.9 cm
diameter of the column d_c	1 cm
bead diameter d	$0.0450 (+ - 0,005) \text{ cm}$
pore volume V_{por}	2.45 cm^3
porosity n	0.35
diffusion constant of the substrate D	$6 \cdot 10^{-6} \text{ cm}^2 \text{s}^{-1}$
flow velocity V	1.25 mm s^{-1}
maximum microbial degradation rate V_{max}	$0.326 \text{ nmol (mg protein)}^{-1} \text{ s}^{-1}$
half-saturation constant K_m	231 nM
biomass in the column m	0.248 mg protein
concentration at the inlet c_{in}	$1.55 \mu M$

Table B.1.: Measured parameters of the column experiment.

In order to apply our results to experimental data values for the Thiele modulus Φ^2 and the mass-transfer coefficient k_{tr} have to be derived, which requires reasonable estimates of typical length scale and specific surface, both needed as scaling units [Vogel, 2002], [Hilfer, 2002].

Appendix B

The maximum reaction rate is given by

$$k_{\max} = \frac{V_{\max} m}{V_{\text{por}}}, \quad (\text{B.9})$$

the specific surface, i.e. the ratio of the reactive surface and the pore volume for a packing of spherical beads is given as

$$a_v = \left(\frac{1}{n} - 1 \right) \frac{6}{d} \quad (\text{B.10})$$

and the hydraulic radius as the typical length scale is

$$r_{\text{hyd}} = \frac{4}{a_v}. \quad (\text{B.11})$$

This expression is equivalent to expressions in the literature [Wood et al., 2007] based on different definitions of the specific surface.

Furthermore the maximum conversion rate is determined as

$$k_{\text{tr}} = \frac{\pi^2}{4} \frac{D a_v}{r_{\text{hyd}}} = \frac{\pi^2}{16} D a_v^2, \quad (\text{B.12})$$

which allows for the calculation of the Thiele modulus and the mass-transfer coefficient using Equations (4.3), (4.12), and (4.5), respectively:

$$\Phi^2 = \frac{k_{\max} r_{\text{hyd}}}{D K_m a_v} = \frac{4 k_{\max}}{D K_m a_v^2} = 1.6 \quad (\text{B.13})$$

$$k_{\text{tr}} = \frac{\pi^2}{4} \frac{D a_v}{r_{\text{hyd}}} = \frac{\pi^2}{16} D a_v^2 = 0.227. \quad (\text{B.14})$$

Danksagung

Für die Vergabe des Themas sowie die fachliche Betreuung und Unterstützung verdiensten in erster Linie meine Betreuer Sabine Attinger und Martin Thullner meinen Dank. Darüber hinaus ist vor allem Florin Adrian Radu zu nennen dessen Code ich für den Großteil meiner Simulationen verwenden durfte und den ich nicht hätte nutzen können ohne viele Tage und Wochen seiner Unterstützung und Mithilfe.

Kaum möglich in ihrer jetzigen Form wäre diese Arbeit aber auch ohne meine Zimmerkollegen. Ihre, oft mehrstündigen, Diskussionen waren mir mehr als einmal Inspiration, Anregung, Prüfstein und Kritik zugleich. Vielen Dank daher an dieser Stelle vor allem an Christoph Schneider sowie an Juliane Mai und Claudia Prüstel.

Durch Korrekturlesen haben sich, neben den oben genannten, vor allem Anke Hildebrandt, Rohini Kumar und Jude Lubega Muusuza meinen Dank verdient. Vollständig wäre diese Liste jedoch nicht ohne die Hilfe von Arne Nägel entsprechend zu würdigen. Seine unermüdliche Energie mir bei meinen ersten Gehversuchen mit UG zur Seite zu stehen, ist mehr als man verlangen kann.

Nicht unerwähnt bleiben soll hier auch die vielfältige Hilfe die mir von den Mitarbeiter des Departments Hydrosystemmodellierung sowie zahlreicher weiterer Angestellter und Wissenschaftler des UFZ wie Sven Lautenbach, Sindy

Rosenkranz, Luis Samaniego, Thomas Schnicke, Daniel Kahlenberg, uva. zuteil wurde. Die freundliche und freundschaftliche Atmosphäre die durch sie am Institut herrschte, haben dazu beigetragen meine Arbeit in den letzten Jahren nicht nur in wissenschaftlicher Hinsicht interessant und anregend zu machen.

Zuletzt möchte ich noch die Unterstützung von Ruth Weinhold heraustreichen. Ihr Vertrauen und ihre Hilfe die mir mehr als einmal die Weiterarbeit ermöglicht haben, können kaum zu hoch geschätzt werden.

Selbstständigkeitserklärung

Ich erkläre, dass ich die vorliegende Arbeit selbstständig und unter Verwendung der angegebenen Hilfsmittel, persönlichen Mitteilungen und Quellen angefertigt habe.

Leipzig, den 15. Februar 2011

Falk Heße

